

Integrated Measurement Techniques for RF-Power Amplifiers



Maikel Huiskamp

INTEGRATED MEASUREMENT TECHNIQUES FOR RF-POWER AMPLIFIERS

Maikel Huiskamp

Samenstelling promotiecommissie:

Voorzitter / secretaris:

prof. dr. J.N. Kok Universiteit Twente

Promotor:

prof. dr. ir. B. Nauta Universiteit Twente

Co-promotor:

dr. ir. A.J. Annema Universiteit Twente

Leden:

prof. dr. L.C.N. de Vreede	Technische Universiteit Delft
prof. dr. ir. P.G.M. Baltus	Technische Universiteit Eindhoven
prof. dr. ir. F.E. van Vliet	Universiteit Twente
dr. ir. A.B.J. Kokkeler	Universiteit Twente



This work is part of the SHERPAS (Self-HEaling Rf Power Amplifier Systems) project (no. 12903) and is supported financially by the Applied and Engineering Science division (TTW) of the Netherlands Organization for Scientific Research (NWO)

**UNIVERSITY
OF TWENTE.**

University of Twente
P.O. Box 217, 7500 AE
Enschede, The Netherlands

INTEGRATED MEASUREMENT TECHNIQUES FOR RF-POWER AMPLIFIERS

PROEFSCHRIFT

ter verkrijging van
de graad van doctor aan de Universiteit Twente,
op gezag van de rector magnificus,
prof. dr. ir. A. Veldkamp,
volgens besluit van het College voor Promoties
in het openbaar te verdedigen
op woensdag 2 februari 2022 om 14:45 uur

door

Maikel Huiskamp
geboren op 22 december 1990
in Deventer

Dit proefschrift is goedgekeurd door:

Promotor

prof. dr. ir. B. Nauta

Co-promotor

dr. ir A.J. Annema

Printed by: Ipskamp printing, Enschede, The Netherlands

ISBN: 978-90-365-5330-8

DOI: 10.3990/1.9789036553308

Copyright © 2022 by Maikel Huiskamp, Enschede, The Netherlands. All rights reserved.
No parts of this thesis may be reproduced, stored in a retrieval system or transmitted in
any form or by any means without permission of the author. Alle rechten voorbehouden.
Niets uit deze uitgave mag worden vermenigvuldigd, in enige vorm of op enige wijze,
zonder voorafgaande schriftelijke toestemming van de auteur.

Abstract

The introduction of the internet of things (IoT) resulted in a significant increase in the demand of low-cost wireless transceivers. To decrease the cost of wireless transceivers, a full implementation on a single die or package, in a modern CMOS technology is preferred. However, with newer CMOS technologies both the maximum supply voltage and the breakdown voltage decrease, reducing the maximum achievable output power that the RF-PA can achieve from the nominal power-supply for a fixed load impedance. Additionally there is an increasing demand for higher data-rates and fully wireless devices, resulting in high requirements on linearity and efficiency of the RF-PA.

To enable higher data-rates within a bandwidth limited frequency spectrum, complex modulation schemes are required. However, complex modulation increases the demands on linearity (e.g. AM-AM and AM-PM conversions), phase accuracy and amplitude accuracy to limit the effects of spectral regrowth, intermodulation and error vector magnitude (EVM) degradation. These forenamed three inaccuracies increase the occupied bandwidth and reduce the SNR of the transmitted signal, resulting in a reduction of spectral efficiency and channel capacity.

Most wireless devices are battery powered, hence power efficiency is an important metric. Complex modulation schemes enable an increase in spectral efficiency, but this comes at the cost of a high peak-to-average power ratio (PAPR). Conventionally an RF-PA has to operate in power-backoff to be able to amplify signals with a high PAPR at a sufficient accuracy, which reduces the overall power efficiency of the RF-PA. Switched mode class-E PAs are promising candidates for battery powered wireless devices, since they can ideally achieve 100% power efficiency and can be integrated in modern CMOS technologies. Additionally process-voltage-temperature variations, such as supply

voltage and antenna impedance variations, impact the performance and reliability of the RF-PA significantly. The performance and reliability of class-E PAs strongly depends on the load impedance, where load variations can reduce the performance and even permanently damage the RF-PA.

The focus of this work is on integrated measurement techniques, reliability improvements and linearisation for RF-PAs to enable efficient, robust and high performance RF-PAs for use in modern wireless transceivers. To enable tuning and improving the performance and reliability of RF-PAs accurate information about its current operating conditions are required, which can be acquired from the internal nodes of the RF-PA. However, the internal RF-PA nodes can contain high frequency components. Directly sampling these nodes with an analog-to-digital converter (ADC) results in a significant power consumption, thus lowering the overall system efficiency.

A 65 nm CMOS RF-waveform characterizer based on an N-path circuit is presented that measures the DC component and the first 3 harmonics of the RF signal by applying a DFT to 8 (ideally) equally spaced in phase quasi-DC output voltages. The accuracy of the waveform estimation is limited by the accuracy of the sampling moments, which in our case is limited by delay cell mismatch. A technique to cancel delay cell mismatch is introduced, that can increase the measurement accuracy by up to 20 dB resulting in a 6.8-bit measurement linearity at the cost of only a small power and area increase.

However, the internal nodes in a switched mode RF-PAs contain RF signals with frequency components above the third harmonic and sampling these signals with 8 samples per period results in aliasing. When using the RF-waveform characterizer aliasing limits the accuracy at which the RF-PA can be characterized, thereby reducing the performance and reliability improvements that can be achieved. Higher sampling rates will reduce the effect of aliasing, but this significantly increases the power consumption assuming that a higher sampling rate can be achieved at all.

To reduce the effect of aliasing without increasing the sample rate an algorithm is introduced that uses two samplers that sample at distinct (non-integer multiple) sampling rates. The algorithm can resolve aliasing and reconstruct the sampled signal as long as it has an orthogonal frequency basis (which is the case for a signal consisting of only harmonics) and the aggregated information-bearing bandwidth of the sampled signal is less than half the cumulative sam-

ple rate of the two samplers.

Load variations result in reflections at the output of the RF-PA, causing a standing wave at the output of the RF-PA. This standing wave increases the voltage at the output of the RF-PA, which can possibly damage or even destroy the RF-PA. The effect of load mismatch is even more apparent in class-E PAs, where due to load mismatch the maximum voltage over the switch can increase up to 13 times the power supply voltage compared to 3.65 times when the load is matched. As a result load mismatch can significantly reduce the reliability of RF-PAs, especially for class-E PAs.

To improve the reliability of class-E PAs, a technique to self-protect the class-E PA by decreasing the PAs sensitivity to load variations is introduced. An on-chip switched-capacitor bank is used to tune the relative-resonance frequency of the switch-LC tank, minimizing the stress on the switch transistor over load variations. To validate the self-protection technique, load-pull measurements are performed on a 65 nm CMOS class-E PA. The proposed self-protection technique increases the safe-operating area from a voltage standing wave ratio (VSWR) of 2:1 up to a VSWR of 19:1, with a worst case impact on output power and efficiency of -1.6 dB and 6% respectively.

RF-PA linearisation techniques such as digital pre-distortion (DPD) are used to reduce the effect of non-linearity. These non-linearities can result in spectral regrowth and intermodulation distortion, which lower the spectral efficiency and possibly cause interference for neighboring channels. Conventionally the DPD coefficients are derived for a 50Ω load, but the load impedance can vary due to external influences and reduces the ability of static DPD to linearise the RF-PA.

This thesis presents a polar class-E PA with adaptive DPD (ADPD), reducing the effect of load variations on the polar modulated class-E PA. The on-chip waveform characterizer is used to measure the internal drain voltage of the class-E amplifier, after which the measured waveform is used to adaptively tune the DPD coefficients. To demonstrate the proposed system, measurements are performed on a 2 GHz 1024 QAM signal with a 1 MSym/s symbol rate. The ADPD system can correct both AM-AM and AM-PM conversion, while maintaining both the target EVM and adjacent channel power ratio over a significantly larger area on the Smith chart compared to a 50Ω optimized static DPD. Furthermore, the ADPD system can simultaneously

correct for slow memory effects (e.g. temperature and antenna load variations) without the need for complex memory DPD algorithms.

Contents

Abstract	i
1 Introduction	1
1.1 CMOS RF-Power Amplifiers	3
1.1.1 RF-Power	3
1.2 Complex modulation techniques	13
1.2.1 Quadrature amplitude modulation (QAM)	13
1.2.2 Orthogonal frequency-division multiplexing	14
1.2.3 Pulse shaping	17
1.2.4 Peak to Average power ratio	20
1.3 Summary and outlook	21
2 RF-Power Amplifiers	23
2.1 Efficiency	23
2.2 Linear vs Switching RF-Power amplifiers	24
2.2.1 Linear RF-PAs	25
2.2.2 Switched mode amplifiers	27
2.3 RF-PA distortion and complex modulation	29
2.3.1 AM-AM and AM-PM	29
2.3.2 EVM	30
2.3.3 Intermodulation distortion	31
2.3.4 Spectral regrowth	32
2.3.5 Adjacent channel power leakage	33
2.4 Power back-off efficiency enhancement techniques	35
2.4.1 Envelope elimination and restoration	35
2.4.2 Outphasing	37

2.5	Linearisation Techniques	41
2.5.1	Feedforward	41
2.5.2	Envelope Feedback	42
2.5.3	Cartesian Feedback	42
2.5.4	Pre-distortion	43
2.6	PA-breakdown	46
2.6.1	Gate-oxide breakdown	46
2.6.2	Hot carrier degradation	46
2.6.3	Punch-through	47
2.6.4	Drain-bulk breakdown	47
2.6.5	Electromigration	48
2.7	Thesis outline	48
3	N-path circuits	51
3.1	Operation	52
3.2	Receiver vs Waveform characterizer	55
3.2.1	Harmonics	55
3.2.2	Signal strength	58
3.2.3	Noise	60
3.3	Sample bandwidth	62
3.4	Timing accuracy	64
4	A Delay Spread Cancelling Waveform Characterizer for RF Power Amplifiers	67
4.1	Sampling Circuit	68
4.2	Delay Spread Cancellation	71
4.3	Measurement Results	76
4.3.1	System measurements	76
4.3.2	Measurements on a misbiased RF-PA	79
4.4	Conclusion	79
5	Reconstructing Aliased Frequency Spectra by Using Multiple Sample Rates	81
5.1	Introduction And Prior Art	81
5.2	Frequency ambiguity due to aliasing	83
5.3	Multi-rate Unaliasing	87

5.3.1	MRU Algorithm	87
5.4	Qualitative Comparison of MRU with other techniques	91
5.4.1	Time-interleaving versus MRU	91
5.4.2	Anti-aliasing versus MRU	92
5.4.3	Potential advantages of MRU	92
5.5	Impact of non-idealities	93
5.5.1	Inaccuracy propagation: the matrix condition number	94
5.5.2	ADC Non-idealities and Calibration	95
5.6	Measurement results	99
5.6.1	Reconstruction of an aliased signal centred around $f_s/2$	101
5.6.2	Reconstruction of aliased signal outside first Nyquist Zone	106
5.6.3	Reconstruction of two aliased signals from distinct Nyquist zones	107
5.7	Conclusion	110
6	Theory and Implementation of a Load-Mismatch Protective Class-E PA System	111
6.1	Introduction	111
6.2	Reliability concerns in class-E PAs	114
6.2.1	Gate-oxide breakdown	114
6.2.2	Hot carrier degradation	114
6.3	Class-E PAs under (non-)nominal conditions	115
6.3.1	Class-E PA basics	115
6.3.2	Effects of load mismatch on class-E PA behavior	116
6.4	Second-order Effects	119
6.5	Simulation Results	119
6.6	Effects of the q and d parameters on PA behavior	123
6.6.1	Effects of the q parameter on PA load-pull contours	124
6.6.2	Effects of the d parameter on PA load-pull contours	124
6.7	Measurements	126
6.8	Self-healing system	130
6.9	Conclusion	133
7	Preserving Polar Modulated Class-E Power Amplifier Linearity under Load Mismatch	135
7.1	Introduction	135

7.2	Linearity of a polar class-E PA under load mismatch	137
7.3	Demonstration of ADPD with polar class-E PA	138
7.3.1	Waveform Characterizer	138
7.3.2	Adaptively Preserving PA Linearity	139
7.3.3	Implementation	140
7.4	Measurements	141
7.5	Conclusion	145
8	Summary and original contributions	147
8.1	Summary	147
8.2	Original contributions	150
A	Numerical example of the MRU algorithm	151
B	IQ extension of the MRU algorithm	155
C	Characterization of harmonics in an RF-PA	159
	Acknowledgement	161
	List of publications	165
	Bibliography	167

Introduction

Wireless communication systems are widespread in our daily lives and can be found in our phones, laptops, tablets, radios and in many more devices. Most of these devices use electromagnetic waves with frequencies within the radio spectrum to communicate with one another and all these devices have to share this available spectrum. The spectrum that can be used for wireless communication is confined by both physics (e.g. absorption of electromagnetic waves by water [1] and oxygen [2]) and technology limits. To enable the increase in wireless devices and higher data-rates more of the usable spectrum is utilized. For example, in current LTE systems frequencies below 6 GHz are used [3] and with the introduction of 5G-NR the frequency bands between 26 GHz and 40 GHz are added to further increase the available spectrum [4]. Figure 1.1 shows an overview of the US spectrum allocation in 2016 for frequencies between 960 MHz and 3 GHz, illustrating how cramped the radio spectrum is.

The introduction of the internet-of-things (IoT) resulted in an enormous increase in the number of devices connected to the internet [5]. IoT finds appli-

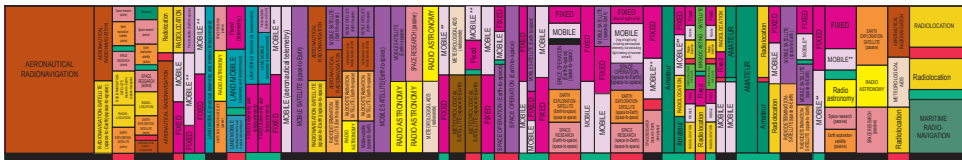


Figure 1.1: US spectrum allocation in 2016 from 960MHz to 3GHz (Source:NTIA).

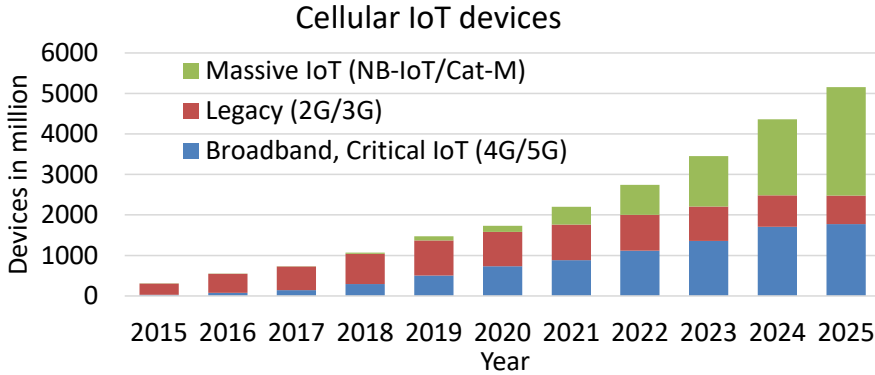


Figure 1.2: Number of (expected) cellular IoT devices from the year 2015 to 2025 [5].

cations in diverse areas such as urban infrastructure, industry, agriculture and healthcare [6]. In an IoT system many devices, e.g. sensors and actuators, are connected to a global network allowing them to communicate with each other and form complex systems. Over the last few years the number of cellular IoT devices exponentially increased as shown in Fig. 1.2. To enable the increase in wireless data transmission within the limited radio spectrum requires modulation schemes with a high spectral efficiency, such as quadrature amplitude modulation (QAM) and/or orthogonal frequency division multiplexing (OFDM) [7]. Both these techniques improve spectral efficiency, however they require highly linear amplifiers and simultaneously reduce the overall system efficiency.

Wireless IoT networks require low-cost, low-power and highly integrated wireless devices. In order to meet these demands, standard CMOS is pursued as a cost-effective solution for integration of wireless systems on chip [8]. Transceivers handle transmission and reception of wireless signals and were already successfully implemented in CMOS technologies decades ago [9, 10]. In CMOS transceivers, the radio frequency power amplifier (RF-PA) remains one of the most power-hungry blocks in modern communication standards that utilize complex modulation. As a consequence the RF-PA significantly limits the duration that transceivers can operate on a single battery charge, hence limiting the autonomous operation of a wireless IoT device.

This chapter provides a high level overview of CMOS RF-power amplifiers and reviews the spectral efficiency and signal properties of the two most com-

mon complex modulation schemes (QAM and OFDM). Chapter 2 discusses the impact of these complex modulations on power efficiency, spectral efficiency and design overhead in practical RF-PAs. Also current solutions to improve RF-PA efficiency when using complex modulation and techniques to improve RF-PA reliability are reviewed. Chapter 2 concludes with an outline of this thesis, introducing the other chapters briefly.

1.1 CMOS RF-Power Amplifiers

Complementary metal-oxide-semiconductor (CMOS) is the most used technology for integrated circuits, since it allows for low-power high performance digital circuits. In 1965, Gordon Moore observed that the transistor density doubled every two years and this observation is now commonly known as Moore's law. The smaller transistor sizes resulted in higher transistor density, allowing for small, efficient and complex digital circuits. Another advantage of scaling CMOS is the reduction in cost per function, allowing for cheaper electronics [11]. Not only digital circuits benefited from Moore's law, but the advances in CMOS technology also made it an attractive candidate for RF circuits [8].

1.1.1 RF-Power

Although most of the transceiver blocks benefit from CMOS scaling, the design of RF-Power Amplifier (RF-PA) becomes more complicated in newer technology nodes, where especially the output power is affected. The power that can be delivered to a load impedance Z_{Load} is equal to

$$P = \frac{V_{rms}^2}{|Z_{Load}|^2} \text{Re}(Z_{Load}), \quad (1.1)$$

where V_{rms} is the rms voltage over the load impedance Z_{Load} . From (1.1) we can conclude that increasing the output power can be achieved by increasing the voltage for a constant load impedance, or by lowering the load impedance for a constant voltage or by both. However, the maximum tolerable voltage in CMOS decreases for smaller technology nodes whereas the nominal antenna load impedance Z_{Ant} remains constant thereby reducing the maximum output power, assuming that $Z_{Load} = Z_{Ant}$.

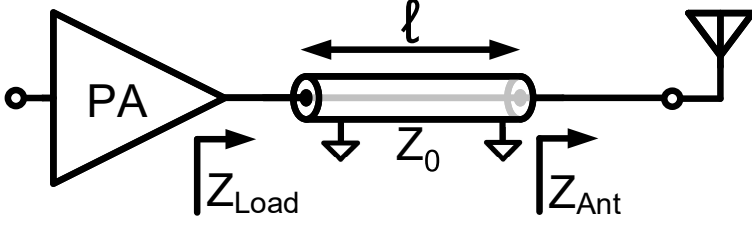


Figure 1.3: Antenna connected to the RF-PA via a transmission line.

Impact of Z_{Load} on the output power

Figure 1.3 shows an RF-PA that is connected to an antenna via a transmission line with a characteristic impedance Z_0 and length ℓ . In case that $Z_{Ant} \neq Z_0$ the impedance Z_{Load} seen by the RF-PA looking into the transmission line depends on Z_{Ant} , Z_0 and the length of the transmission line ℓ [12]:

$$Z_{Load} = Z_0 \frac{1 + \Gamma e^{-j2\beta\ell}}{1 - \Gamma e^{-j2\beta\ell}} = Z_0 \frac{Z_{Ant} + jZ_0 \tan(\beta\ell)}{Z_0 + jZ_{Ant} \tan(\beta\ell)} \quad (1.2)$$

where $\beta = 2\pi/\lambda$ and the reflection coefficient Γ is the ratio between the reflected power P_r and the incident power P_i . In equation, Γ can be written as

$$\Gamma = \frac{P_r}{P_i} = \frac{Z_{Ant} - Z_0}{Z_{Ant} + Z_0}, \quad (1.3)$$

where $0 \leq |\Gamma| \leq 1$ for passive loads Z_{Ant} . As a consequence any variation of the antenna impedance Z_{Ant} changes the impedance Z_{Load} presented to the output of the RF-PA.

The antenna is commonly modelled for simplicity as a 50Ω resistor. However the antenna impedance is not only determined by the antennas shape and size [13], but is also influenced by its near field environment [14]. This results in changes of the antenna impedance, hence impacting Z_{Load} and thus the RF-PA output power. Figure 1.4 shows a smith-chart which contains equi-power contours for different Z_{Load} , assuming that

$$\frac{V_{max}}{I_{max}} = 50\Omega = R_{opt} \quad (1.4)$$

where V_{max} and I_{max} are respectively the maximum output voltage and output current of the RF-PA. A smith chart is a tool to represent impedances (all

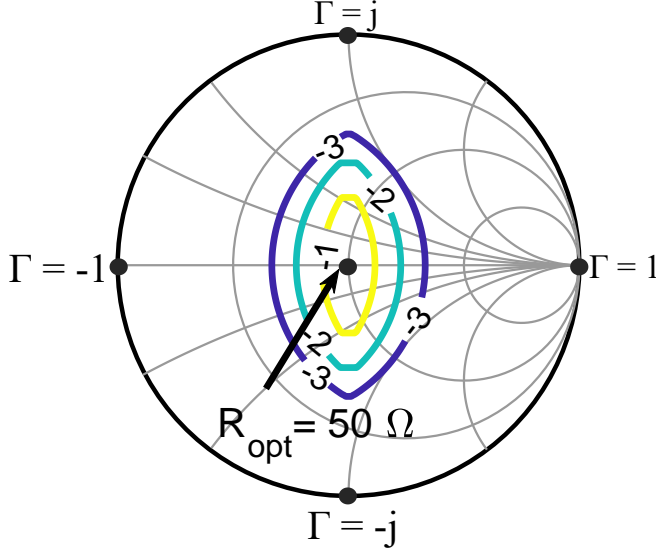


Figure 1.4: Equal power contours (dB) for variations in Z_{Load} , assuming (1.1), $|V_{out}| \leq V_{max}$, $|I_{out}| \leq I_{max}$ and $R_{opt} = 50\Omega$. Note that the outer circle of the smith chart corresponds to $|\Gamma| = 1$.

passive impedances fit within the unit circle), allowing the representation of various properties, such as constant power contours, constant efficiency contours and safe operating area for different impedances.

The smith-chart can be viewed as a polar plot of the reflection coefficient Γ , where the magnitude $|\Gamma|$ is plotted as the radius from the center of the smith-chart and the angle θ ($-180^\circ \leq \theta \leq 180^\circ$) is defined counter clockwise from the right hand side of the horizontal line [12]. The center of the smith chart is conventionally chosen to be the characteristic impedance, but the smith chart can be normalized to any (passive) impedance.

Figure 1.4 shows that the output power reduces for any impedance mismatch between the antenna and the transmission line ($|\Gamma| > 0$); the reduction is visualized by the equi-power contours which are normalized with respect to the output power when the RF-PA is loaded with R_{opt} . In Fig. 1.4 it is assumed that $|V_{out}| \leq V_{max}$, $|I_{out}| \leq I_{max}$ and $V_{max}/I_{max} = 50\Omega = R_{opt}$. In case that $\text{Re}(Z_{Load}) > R_{opt}$ the RF-PA output power is voltage limited and if $\text{Re}(Z_{Load}) < R_{opt}$ the RF-PA output power is current limited.

If $Z_{ant} \neq Z_0$ ($\Gamma \neq 0$) then reflections occur at the interface of these two

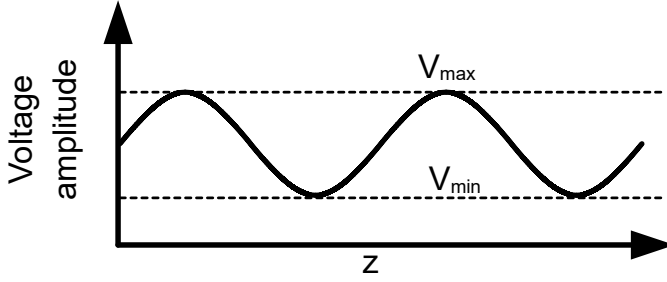


Figure 1.5: Voltage amplitude along a transmission line illustrating VSWR. The VSWR is a function of the distance z to the antenna.

impedances. The incident and reflected wave add to form a standing wave along the transmission line [12], which is shown in Fig. 1.5. If the incident and reflected wave are exactly in phase the maximum voltage amplitude can increase by up to a factor two. The voltage standing wave ratio (VSWR) is defined as the ratio between the maximum voltage V_{max} and minimum voltage V_{min} along the transmission line. Mathematically it is described by

$$\text{VSWR} = \frac{|V_{\max}|}{|V_{\min}|} = \frac{1 + |\Gamma|}{1 - |\Gamma|}. \quad (1.5)$$

The maximum supply voltage reduces with newer CMOS technology nodes, hence the maximum tolerable voltage V_{max} of the RF-PA also decreases for lifetime reasons. To maintain a specific output power P_{out} , the I_{max} has to increase, which cannot be done for a static 50Ω load impedance when V_{max} decreases. There are some possible solutions to increase P_{out} in modern CMOS processes:

- Present the RF-PA with a $|Z_{load}| < |Z_{Ant}|$ by means of an (impedance) matching network.
- Combine the output power of N RF-PAs that can operate at the lower supply voltage to achieve the wanted P_{out} .
- Allow the RF-PA to operate at higher than nominal voltages, allowing to retain $Z_{Load,opt} = V_{max}/I_{max} = 50\Omega$.
- Combinations of the previously mentioned techniques.

The next sections will describe these solutions to increase P_{out} .

Using impedance matching networks

Conventionally an RF-PA is loaded with an antenna that has an impedance Z_{Load} , which is designed to have a nominal impedance of 50Ω . Matching networks can be used to lower the apparent load the RF-PA sees, allowing a higher output power for the same supply voltage and antenna. A schematic overview of a RF-PA with a matching network is shown in Fig. 1.6.

The impedance transformation ratio r is defined as [15]

$$r = \frac{\Re(Z_{Ant})}{\Re(Z_{Load})}, \quad (1.6)$$

where $Z_{Ant} = R_{Ant} + jX_{Ant}$ and $Z_{Load} = R_{Load} + jX_{Load}$ when looking into the matching network. Commonly the matching network used in RF-PAs are low-loss; in the discussions below lossless matching networks are assumed for simplicity reasons.

Lossless matching networks exhibit trade-offs between matching and bandwidth, which is described by the Bode-Fano criterion [16, 17]. Fig. 1.7 shows a system consisting of a lossless matching network that is used to match the parallel RC load. The Bode-Fano criterion for this network states that

$$\int_0^\infty \ln \frac{1}{|\Gamma(\omega)|} d\omega \leq \frac{\pi}{RC}, \quad (1.7)$$

where $\Gamma(\omega)$ is the frequency dependent reflection coefficient seen at the input of the matching network.

When using an infinite number of elements in the matching network the

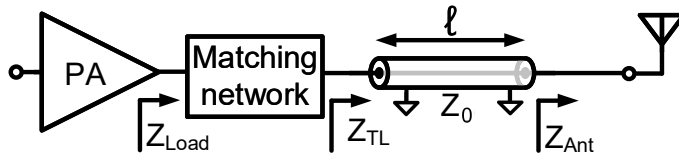


Figure 1.6: (a) PA connected to an antenna via a transmission line. Z_{TL} and Z_{Ant} are respectively the impedance seen looking into the transmission line and antenna, Z_0 is the characteristic impedance of the transmission line and ℓ is the length of the transmission line. P_i and P_r are the incident and reflected power waves.

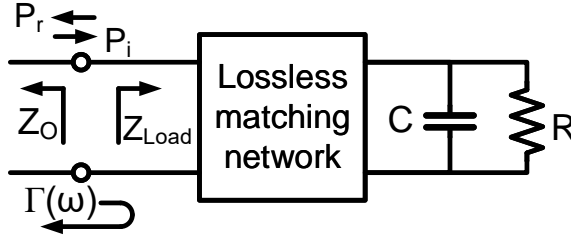


Figure 1.7: Impedance matching for a parallel RC-circuit. $\Gamma(\omega)$ is the frequency dependent reflection coefficient seen at the input of the matching network.

Bode-Fano criterion can also be described as

$$\frac{1}{\ln(|\Gamma|)} = \frac{\pi}{QB}, \quad (1.8)$$

assuming a flat $|\Gamma|$ over a fractional bandwidth B and where Q is the quality factor of the load. The Bode-Fano criterion shows that perfect matching ($\Gamma = 0$) can only be achieved at a single frequency, hence a broader bandwidth comes at the cost of a higher passband reflection coefficient and thus decreases the efficiency of the RF-PA. A high impedance transformation ratio $|r|$ commonly requires a high Q to retain efficiency, thus lowering the fractional bandwidth B over which matching can be achieved.

One of the most common matching networks is the LC-resonance transformer [12], which is shown in Fig. 1.8(a). The topologies shown on the left in Fig. 1.8(a) can be used for $|r| \geq 1$, while the topologies on the right can be used for $0 \leq |r| \leq 1$. These topologies allow for simple integration in CMOS technologies, however they suffer from high losses for high values of $|r|$ [15] due to the Q -factor of the inductors. In case that a high- Q matching is achieved the bandwidth is significantly reduced [18]. Note that matching a purely resistive antenna with a LC-resonance transformer still has a limited bandwidth B , since a reactive element is added to the load impedance when using an LC-resonance transformer that increases the effective Q of the load impedance.

Another solution for impedance transformers is to use magnetically coupled inductors as shown in Fig. 1.8(b). Magnetically coupled inductors can achieve a higher efficiency than LC-resonance transformers for higher $r = N^2$, however a high impedance transformation ratio requires a relative low primary

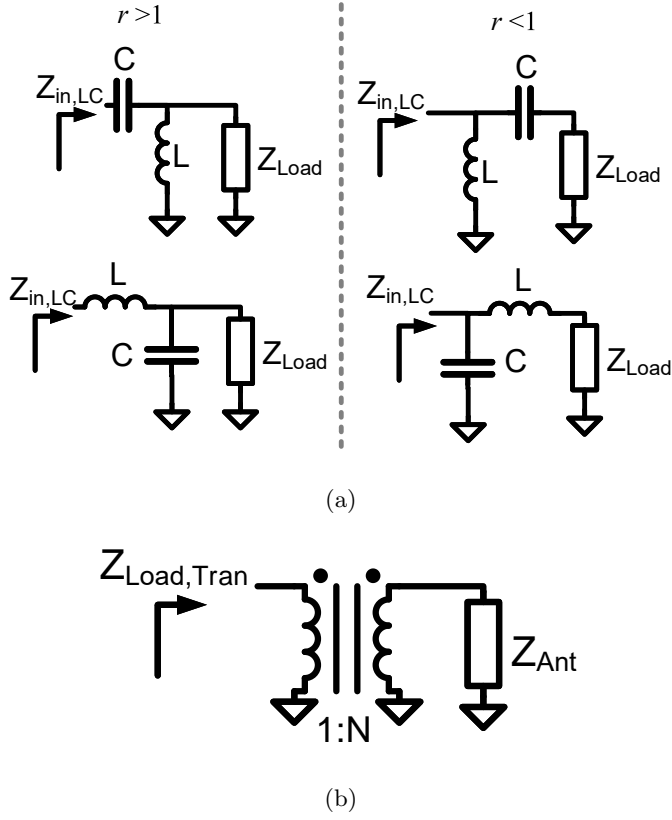


Figure 1.8: Different impedance transformation techniques. (a) The LC resonant impedance transformer. (b) The magnetically coupled transformer impedance transformer.

inductance (in the order of 80 pH at 2 GHz for $r = 50$ in case of 100 % efficiency [15]) making implementation on chip impractical. An ideal transformer based matching network is not limited by the bode-fano criterion. However in practical transformers the impedance of the inductors used can be modelled as an additional inductive load to Z_{Ant} [17], which limits the bandwidth of the magnetically coupled transformer. The bandwidth can be increased by introducing losses in the coupled inductors since it lowers the overall Q of the system.

Figure 1.9 illustrates the effect of using an impedance matching network with $r = 2.5$ on the equi-power contours [19], where $Z_{opt} = 20\Omega$ assuming

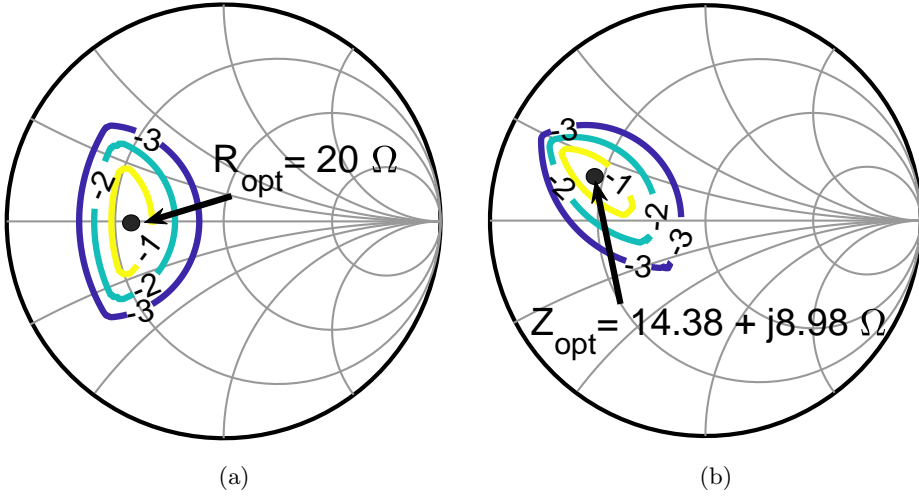


Figure 1.9: (a) Smith chart normalised to 50Ω with the equal power contours normalised to the output power of the RF-PA that has an $R_{opt} = 20\Omega$ when Z_{Ant} is matched to that optimum load impedance R_{opt} by using a matching network. (b) Required compensation for Z_A to compensate for the effect of a shunt capacitor and the equi-power contours when $Z_{Ant} \neq 50\Omega$.

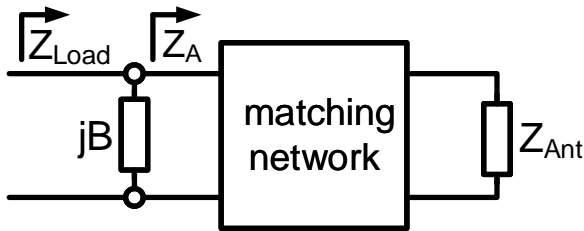


Figure 1.10: Matching network followed with a shunt impedance in front which can model a package parasitic.

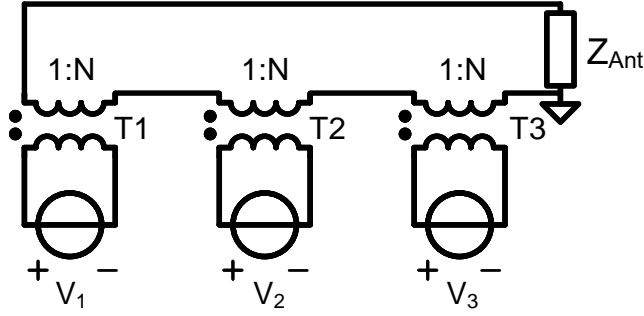


Figure 1.11: Distributed active transformer.

that $Z_{Ant} = 50\Omega$. Note that the equi-power contours are shifted to the left compared to Fig. 1.4. Due to for example package parasitics, the matching network can be followed by e.g. a shunt impedance as shown in Fig. 1.10 which causes the load impedance Z_{Load} to be different from Z_A . To de-embed the effect of the shunt capacitance the impedance looking into Z_A requires the correct compensation as shown in the smith chart in Fig. 1.9(b) for $Z_{Ant} = 50\Omega$, $r = 2.5$ and $B = -32\Omega$. In case that the impedance Z_A is designed such that $Z_A = 14.38 + j8.98\Omega$, the impedance $Z_{Load} = R_{opt} = 20\Omega$, thus allowing the RF-PA to be loaded with the optimum load.

Power combining

Impedance transformation can also be achieved by means of a distributed active transformer (DAT) [15], see Fig. 1.11. It uses M 1: N magnetically coupled transformers where the secondary sides are connected in series effectively summing the individual voltage contributions, allowing high impedance transformation ratios ($r = MN^2$) while retaining a high efficiency. The work in [15] uses 1:1 transformers due to their low loss, equal winding sizes and that they can be implemented as high-Q coupled slab inductors. In case of 1:1 transformers the impedance transformation ratio of a DAT is equal to the number of 1:1 transformers. Note that this power-combining technique exhibits the same type of bandwidth limitations as the magnetically coupled transformers.

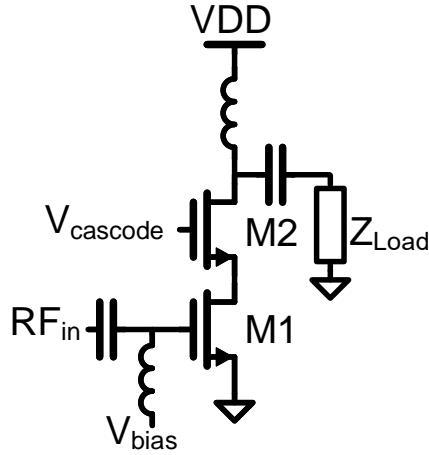


Figure 1.12: RF-PA with cascode transistor (M2). Conventionally Z_{Load} is the impedance seen at the input of the impedance transformers in Fig. 1.8.

Using high voltage devices

The maximum operating voltage decreases with smaller CMOS nodes, resulting in a decrease in the maximum power that can be delivered to a fixed load Z_{Load} , where Z_{Load} is the impedance when looking into one of the impedance transformers from Fig. 1.8 (a) or (b). A solution to increase the RF-PA output power is to allow for higher operating voltages in the RF-PA [20], which can be achieved by means of stacking transistors [21, 22], using thick-gate oxide transistors or a combination of both.

Thick-gate oxide transistors are commonly available in CMOS technologies. They can withstand higher voltages, however their performance is comparable to thin oxide transistors from typically two generations ago [23]. Instead of increasing the gate oxide thickness it is also possible to use transistors with a different topology to increase the breakdown voltage, e.g a laterally-diffused metal-oxide semiconductor (LDMOS) transistors. LDMOS transistors are cost effective RF-power transistors that allow for higher breakdown voltages, while they can still be implemented in a standard CMOS process [24, 25].

1.2 Complex modulation techniques

There is a limit to the maximum number of bits per second that can be transmitted within a certain channel, this limit is called the channel capacity. In 1948 Shannon stated that [26] the upper limit for the maximum channel capacity C within a certain channel bandwidth B is given by

$$C = B \log_2(1 + \text{SNR}), \quad (1.9)$$

where SNR is the signal to noise ratio of the received signal. To approach the upper limit in (1.9) requires complex modulation schemes, like quadrature amplitude modulation (QAM) and orthogonal frequency division multiplexing (OFDM).

1.2.1 Quadrature amplitude modulation (QAM)

In QAM, data is modulated onto two orthogonal carriers, conventionally chosen as $\sin(\omega_c t)$ and $\cos(\omega_c t)$. A schematic overview of a QAM modulator is shown in Fig. 1.13 (a). A serial to parallel (S/P) converter separates the serial input data into two parallel outputs, x_I and x_Q , which are used to weigh the orthogonal carriers. The final output signal is given by

$$x(t) = x_I(t) \cos(\omega_c t) - x_Q(t) \sin(\omega_c t). \quad (1.10)$$

Fig 1.13 (b) demonstrates the serial to parallel conversion. In this example two bits per symbol are used (4-QAM) to modulate the amplitudes of the orthogonal carrier, where $\{x_I, x_Q\} \in \{-1, 1\}$. In this example a binary 0 is mapped to -1 and a binary 1 is mapped to 1. Fig. 1.13 (c) demonstrates a 16-QAM constellation, where $\{x_I, x_Q\} \in \{\pm 1, \pm 3\}$. In this case both $x_I(t)$ and $x_Q(t)$ can take four separate values, hence $2 \log_2(4) = 4$ bits per symbol can be transmitted simultaneously when using 16-QAM. In general square QAM constellations with $M = 2^B$ points ($B \in \mathbb{N}$) allow for B bits to be transmitted per symbol. Figure 1.14 shows a stylistic representation of the spectrum of a M-QAM signal. For a symbol rate T the spectral efficiency η_{QAM} for M-QAM is

$$\eta_{QAM} = \frac{\log_2(M)}{T \cdot BW} \quad [\text{bits/s/Hz}]. \quad (1.11)$$

To approach the limit in (1.9), $M = (1 + \text{SNR})$, where SNR is the signal to noise ratio of the received signal and assuming that $T = 1/BW$ (Nyquist

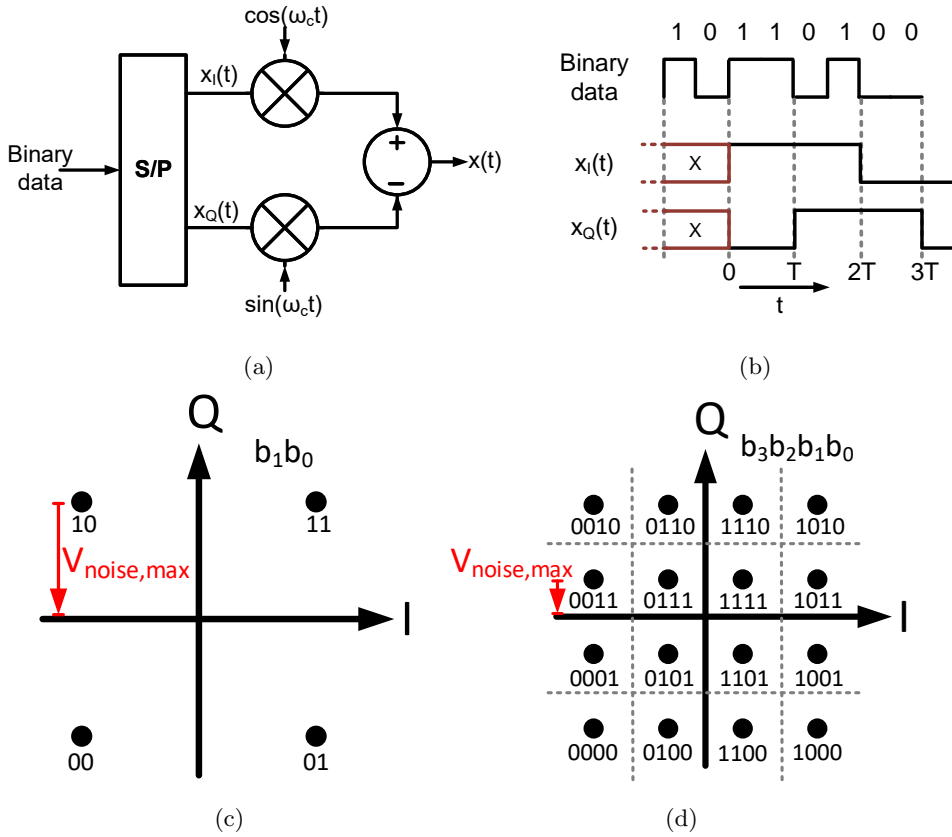


Figure 1.13: (a) QAM modulator (b) Serial to parallel conversion. Only when the first symbol is being loaded the output is undefined. (c) 4-QAM (QPSK) constellation (d) 16-QAM constellation. $V_{\text{noise,max}}$ is the maximum allowable noise voltage before a bit error occurs.

limit). Hence, a higher M requires a higher SNR, which is illustrated in Fig. 1.13(c) and (d) where the maximum allowable noise voltage $V_{\text{noise,max}}$ before a bit error occurs in Fig. 1.13(d) is reduced compared to that in Fig. 1.13(c).

1.2.2 Orthogonal frequency-division multiplexing

Orthogonal frequency-division multiplexing (OFDM) is widely used in wireless communication. In OFDM the information is modulated onto closely spaced orthogonal sub-carriers with spacing Δf and each sub-band can be individually modulated.

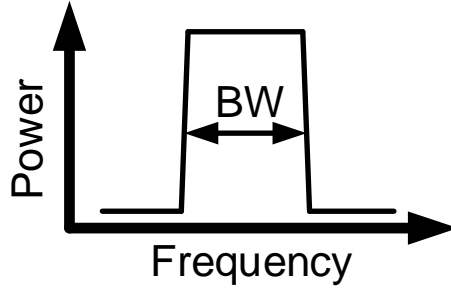


Figure 1.14: Stylistic representation of a M-QAM spectrum. BW is the occupied bandwidth by the M-QAM signal.

A simplified schematic overview of a typical OFDM modulator where each sub-carrier is modulated with 16-QAM is shown in Fig. 1.15. First the serial data stream is split into N multiple parallel data stream, after which each stream is mapped on a 16-QAM constellation ($M=16$), resulting in a set of N complex numbers C . The N complex number streams are then modulated onto N closely spaced sub-carriers (in LTE the sub-carrier spacing $\Delta f = 15\text{kHz}$ [27]), which can be efficiently implemented using the inverse fast Fourier transform (IFFT) [28]. The IFFT produces a complex signal

$$s_n = \frac{1}{N} \sum_{k=0}^{N-1} C_k e^{j2\pi kn/N}. \quad (1.12)$$

The complex signal s_n is split into its real and imaginary components and both are converted to the analog domain by a digital-to-analog converter (DAC). The real and imaginary analog signals are then up-converted to the carrier frequency f_c by multiplying them with $\cos(2\pi f_c t)$ and $\sin(2\pi f_c t)$ respectively. Finally the up-converted signals are added, resulting in the OFDM band pass signal with (ideally) a bandwidth $BW_{OFDM} = \Delta f N$. Ideally OFDM thus has a spectral efficiency

$$\eta_{OFDM} = N \frac{\log_2(M)}{T \cdot BW_{OFDM}} \quad [\text{bits/s/Hz}] \quad (1.13)$$

where T is the OFDM symbol duration and conventionally $T = 1/\Delta f$.

Figure 1.16 shows the spectrum of an OFDM signal with $N=5$ carriers. Here each carrier is spaced by a frequency $\Delta f = 15\text{kHz}$. Note that the peaks

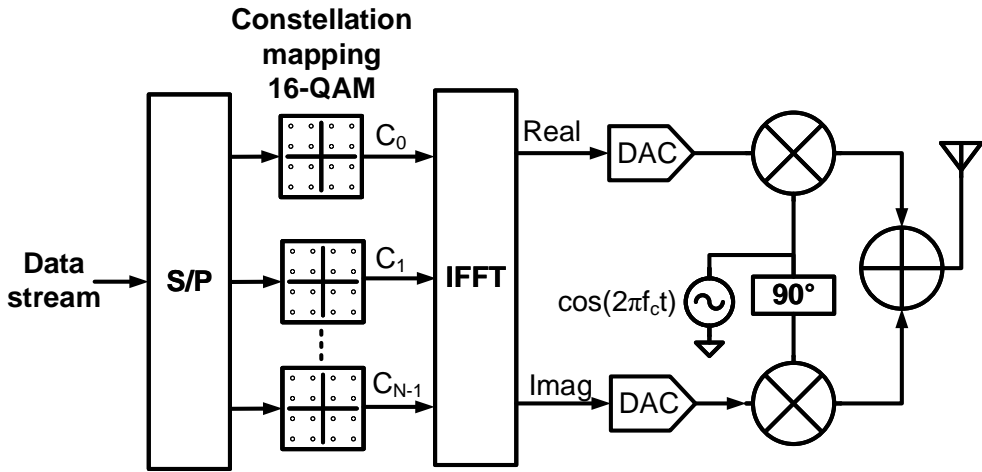


Figure 1.15: OFDM modulator, where each sub-carrier is modulated with 16-QAM.

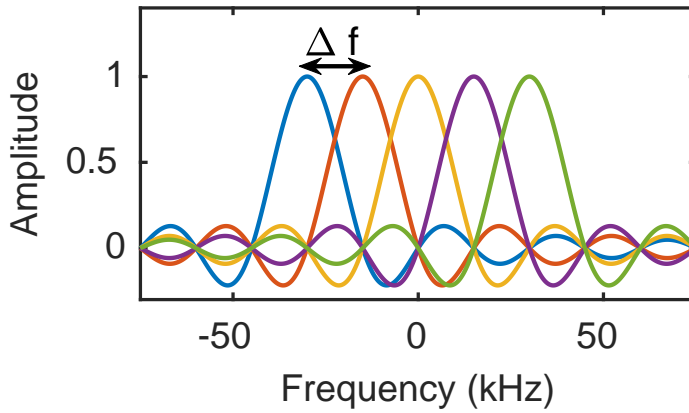


Figure 1.16: Baseband OFDM spectrum where each sub-carrier has a different color. Δf is the frequency spacing between sub-carriers.

of each sub-carrier correspond with the nulls from the other sub-carriers, hence the sub-carriers do not interfere with each other. However this only occurs when the OFDM signal is observed for a duration NT ($N \in \mathbb{N}$) and no symbol transitions occur within that time frame. In case of a delay-dispersive channel the transmitted data is smeared out over a longer duration, possibly causing interference of previously transmitted data with current transmitted data. This effect is called inter-symbol-interference (ISI). To reduce the impact of delay-dispersive channels on OFDM a copy of the last part of the transmitted signal is appended to the signal, which is called a cyclic prefix [7]. By discarding the first part of the received symbol the ISI due to delay-dispersion is removed. Note that the cyclic prefix extends the symbol duration and thus lowers the spectral efficiency of OFDM compared to the ideal case.

For an ideal channel the performance of OFDM is similar to single carrier QAM. However OFDM is more resilient to frequency selective fading compared to a single carrier system [28, 29], since each of the narrow-band sub-carriers can be equalized separately. This allows higher bit rates compared to a single carrier system when the channel exhibits frequency selective fading, allowing OFDM to approach the Shannon information limit [30]. Disadvantages of OFDM are an increased sensitivity to frequency offset and drift [31] and that it requires an RF-PA that can amplify signals with a high peak to average power ratio [32].

1.2.3 Pulse shaping

In digital communication systems, the data is grouped in symbols, where each symbol contains a value that represent a certain set of bits. In the digital domain there is an abrupt change between consecutive symbols, which can be described by a pulse as shown in Fig. 1.17(a). The transmitted pulse corresponds to sinc shaped frequency content as shown in Fig. 1.17(b), which is a relatively wide-band signal. However, the channel over which the data is transmitted is band-limited, resulting in filtering of the transmitted data. This filtering smears out the abrupt change between symbols over a longer duration, resulting in inter-symbol-interference (ISI). ISI degrades the performance of the wireless link by reducing the SNR.

In most communication standards the available bandwidth is limited. If the available bandwidth equals $2/T$ the main lobe of the pulse fits in the

channel bandwidth. However the first side-lobe is only 13 dB weaker than the main lobe [7], which will result in significant inter-carrier-interference (ICI) and thus violates the specifications for most communication standards.

To reduce the occupied bandwidth of the digital data, the pulse is shaped by means of filtering. The filter that would allow for the highest utilization of the channel bandwidth BW is a sinc function [33], which is zero in the time domain at multiples of T except for $T = 0$. Hence when sampling at exact multiples of T there will be no ISI, however small sampling timing errors can result in significant inter-symbol interference.

Conventionally (root) raised cosine filters are chosen as a pulse shape, since they reduce the signal bandwidth compared to a square pulse while also reducing the impact of sampling timing errors on ISI compared to when using a sinc filter. Figure 1.18 (a) and (b) show the impulse response and the spectrum for the raised cosine filter for various α . The raised cosine impulse response is given by [33]

$$h_{RC}(t) = \frac{\sin(\pi t/T)}{\pi t/T} \frac{\cos(\pi \alpha t/T)}{1 - 4\alpha^2 t^2/T^2}, \quad (1.14)$$

where $0 \leq \alpha \leq 1$ is called the roll-off factor and T is the symbol period.

The excess bandwidth (bandwidth occupied by the signal beyond the Nyquist bandwidth BW) is proportional to α , where $\alpha = 0.25$ corresponds to an excess bandwidth of 25%. To fully utilize the channel bandwidth BW the symbol duration $T = (\alpha + 1)/BW$. However, to reduce ICI a small portion of frequency spectrum is kept empty. This empty spectrum is called a guard band and it allows simultaneous transmission neighbouring channels, but it comes at the cost of a decrease in spectral efficiency [7].

There also exists a trade-off between α and peak-to-average power ratio (PAPR) [34], where a lower α results in a lower PAPR. Hence choosing α is a trade-off between ISI, ICI, bandwidth and PAPR. PAPR is further described in section 1.2.4.

Conventionally in a communication system a root raised cosine is used before both the transmitter and the receiver. This results in a overall raised cosine response, while simultaneously allowing matched filtering that can improve the SNR of the received signal [7].

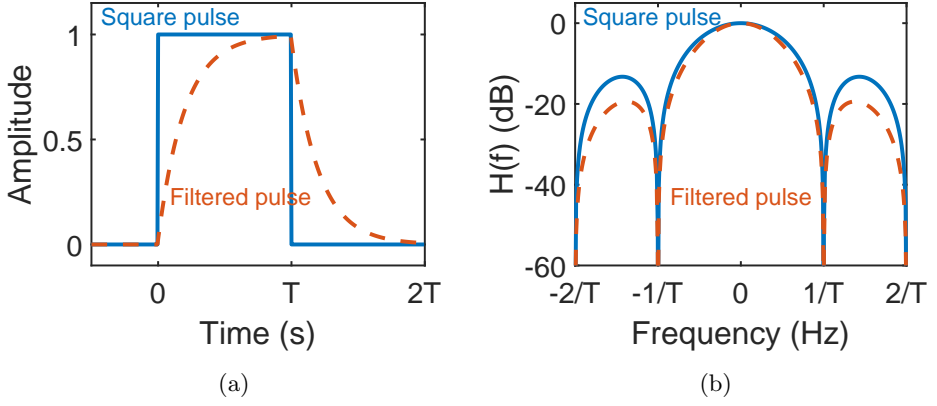


Figure 1.17: (a) Impulse response of a square pulse with duration T . The solid (blue) line is the ideal pulse and the dashed (red) line the filtered pulse due to bandwidth limitations. Note that the dashed line is non-zero during the next symbol duration (T to $2T$), resulting in ISI (b) Frequency response of the square pulse (solid blue line) with duration T and the frequency response of the filtered pulse (dashed red line) from (a).

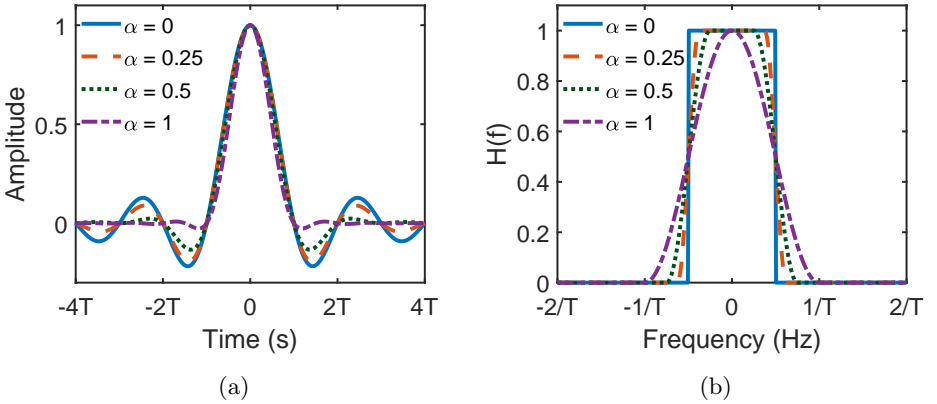


Figure 1.18: (a) Impulse response of a raised cosine filter for different α . The distinct lines correspond to different α for the raised cosine filter. (b) Frequency response of a raised cosine filter for different α .

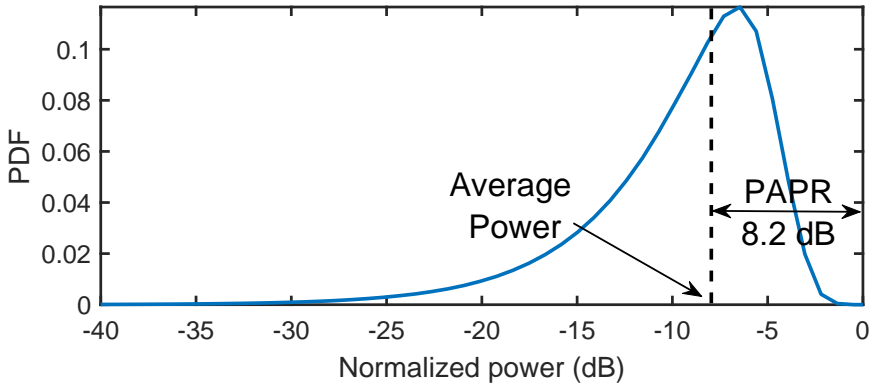


Figure 1.19: Probability density function of a single carrier 1024-QAM signal with root raised cosine filter, with $\alpha = 0.25$. In this case the PAPR = 8.2dB.

1.2.4 Peak to Average power ratio

The peak to average power ratio (PAPR) for RF-PAs is a measure of the peak envelope power divided by the RMS signal power and is defined as [35]

$$\text{PAPR} = \frac{\max |x(t)|^2}{E\{|x(t)|^2\}}, \quad (1.15)$$

where $x(t)$ is the complex baseband signal used to modulate the RF-PA. Very complex modulation schemes, such as 1024-QAM and OFDM with 1024 sub-carriers, exhibit high PAPR. Fig. 1.19 shows the probability density function of a single-carrier 1024-QAM signal versus the signal power normalized to the maximum output power. In this example, when an RF-PA is designed to transmit on average 1 W of power, it has to deliver a peak power of 6.2 W. To enable this peak current the RF-PAs operates for almost the full duration of a modulated signal below its maximum output power (power back-off). This creates headroom for signals with a high PAPR, but comes at the cost of a significantly reduced efficiency [36] (see also chapter 2.2).

The PAPR depends on the used modulation and pulse shaping. The top row in Table 1.1 shows the PAPR for different QAM constellations for a square pulse (no pulse-shaping). In case of square pulses the PAPR differs from 0 dB for QPSK (4-QAM) to 4.5 dB for 1024-QAM, hence a higher spectral efficiency results in a higher PAPR and consequently a lower power efficiency for the RF-PA.

Table 1.1: Simulation results for single carrier PAPR of different QAM constellations without and with RRC filtering. The number of symbols used in the simulation is 10^6 .

QAM	4 (QPSK)	16	64	256	1024
PAPR(dB), square pulse	0	2.6	3.7	4.2	4.5
PAPR(dB), RRC $\alpha = 0.25$	4.9	7.1	7.8	7.9	8.2

To improve the spectral efficiency pulse shaping is used (see section 1.2.3), which increases the PAPR of the used modulation. The work in [34] derives relations for the PAPR of single carrier QAM signals which are filtered by a root raised cosine filter (RRC), showing that the PAPR increases compared to using square data pulses. The bottom row in Table 1.1 shows the simulated single carrier PAPR for different QAM constellations when using a root raised cosine (RRC) ($\alpha = 0.25$) pulse shaping filter [34]. These results show an increase of more than 3.7 dB in PAPR when using a RRC filter ($\alpha = 0.25$) compared to using a square pulse. Compared to single carrier operation, the PAPR in multi-carrier systems such as OFDM can be even higher, where in case of 1024 sub-carriers modulated with 16-QAM (rectangular pulse shape) the PAPR = 13.8 dB [32].

Multiple approaches to reduce the PAPR have been proposed [37], e.g. amplitude clipping, clipping & filtering and coding. While all these techniques reduce PAPR, these also impact other important metrics in a wireless link, such as bit error rate, loss in data rate, and an increase in computational complexity.

1.3 Summary and outlook

With the introduction of IoT the number of wireless devices significantly increased. Full implementation of the wireless IoT node in CMOS technologies is preferred to enable low-cost, low-power and highly integrated devices. The supply voltage decreases with modern CMOS nodes, which complicates the design of RF-PAs. This chapter reviewed some known techniques to enable RF-PAs in modern CMOS technologies, while retaining a relatively high output power. Achieving a high data-rate in the limited available spectrum re-

quires modulation schemes with a high spectral efficiency, such as QAM or OFDM. However, these complex modulations yield a high PAPR. In single carrier systems pulse shaping is used to reduce the occupied bandwidth, but this further increases the PAPR. In conventional OFDM no pulse shaping is used. However, in OFDM the PAPR increases with the number of sub-carriers, hence a similar trade-off between bandwidth and PAPR exists.

Chapter 2 first discusses the efficiency of several RF-PA topologies, after which the effect of complex modulation schemes on the RF-PA efficiency is discussed. Secondly, the effects of non-idealities in the RF-PA on the transmitted complex modulated signal is discussed. Thereafter known techniques to improve RF-PA linearity and efficiency are described. Lastly chapter 2 concludes with an outline of the thesis.

Chapter 2

RF-Power Amplifiers

Transceivers use RF-power amplifiers (RF-PAs) to amplify the power of the modulated RF-signal, allowing transmission of the RF-signal over large distances. RF-PAs handle relatively high currents and voltages and are typically the most power consuming blocks in a transceiver. Because of this they exhibit significant trade-offs between efficiency and reliability. This chapter first provides a definition for efficiency in RF-PAs, after which it discusses some of the most common types of RF-PAs and their performance metrics such as output power, efficiency and linearity. Secondly it describes the impact of nonlinearities in the RF-PA when using complex modulation, followed by techniques to improve the efficiency and linearity of RF-PAs. Lastly this chapter discusses some of the most common breakdown mechanisms in RF-PAs that arises from the high voltages and currents in the RF-PA and it concludes with an outline of this thesis.

2.1 Efficiency

In RF-PAs, "efficiency" describes the RF-PAs ability to convert power from the DC-power supply to RF power, hence efficiency is an important performance metric. Not only will a highly efficient RF-PA increase the operation time from a single battery charge, but it will also reduce the amount of heat generated and thus reduces the required cooling. Mathematically, the drain efficiency

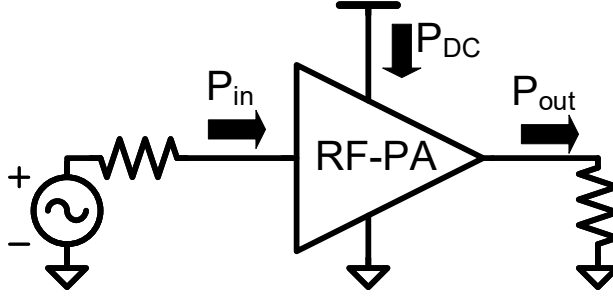


Figure 2.1: Definitions for P_{in} , P_{out} and P_{DC} in an RF-PA.

η_{DE} of the RF-PA is described by

$$\eta_{DE} = \frac{P_{out}}{P_{DC}}, \quad (2.1)$$

where P_{out} is the power delivered to the load at the fundamental frequency and P_{DC} the power drawn from the DC-power supply as shown in Fig. 2.1.

Besides the power drawn from the supply, RF-PAs also require a certain input power to drive them. This input drive power is not taken into account in the drain efficiency, which may obscure the power gain by the RF-PA. For this reason the power added efficiency (PAE) metric is frequently used. This PAE includes the input power into the efficiency equation; in equation it is given by

$$PAE = \frac{P_{out} - P_{in}}{P_{DC}}, \quad (2.2)$$

where P_{in} is the power delivered to the input of the RF-PA at the fundamental frequency.

2.2 Linear vs Switching RF-Power amplifiers

Many types of different RF-PAs exist, yet RF-PAs can be categorized by their operation mode in two categories; linear or switched mode. In a linear amplifier the transistor is used as a variable current source and its first order behaviour exhibits both amplitude and phase linearity [36]. In contrast, switched mode RF-PAs use a transistor as a switch and only have phase linearity. Within these two operation modes different classes of amplifiers exist, which all have

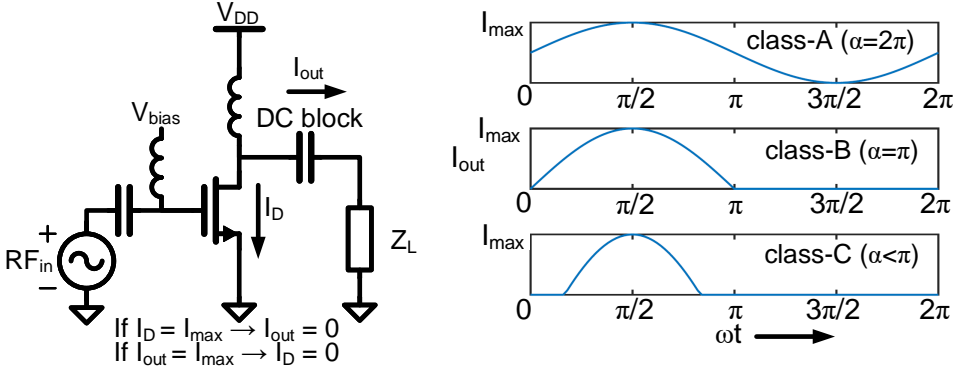


Figure 2.2: Schematic representation of a linear RF-PA together with the current waveforms when the RF-PA is biased in class A,B or C.

different advantages and disadvantages. This section describes both linear and switched mode amplifiers and some of the most common classes of RF-PAs.

2.2.1 Linear RF-PAs

Linear RF-PAs are typically classified by their conduction angle α , which is the proportion of the RF-cycle for which the transistor conducts current [19], see Fig. 2.2. A class-A amplifier conducts over the full RF-cycle and thus has a conduction angle of 2π . A class-B amplifier will only conduct 50% of the time, hence it has a conduction angle of π . Class-C amplifiers have conduction angles $< \pi$. The output waveforms are restored by the resonant load Z_L .

The value of the conduction angle α affects both the RF-PAs output power and efficiency. In this section it is assumed that the input is chosen in such a way that the output current I_{out} of the RF-PA is varied between 0 and I_{max} . The power utilization factor (PUF)[19] is defined as the output power of the device operating in a certain class compared to the same device operating in class-A and can be described as

$$PUF = \frac{1}{\pi} \frac{\alpha - \sin(\alpha)}{1 - \cos(\alpha/2)}. \quad (2.3)$$

RF-PAs with a high PUF can thus produce higher output powers from the same active device. The drain efficiency of a linear amplifier for conduction

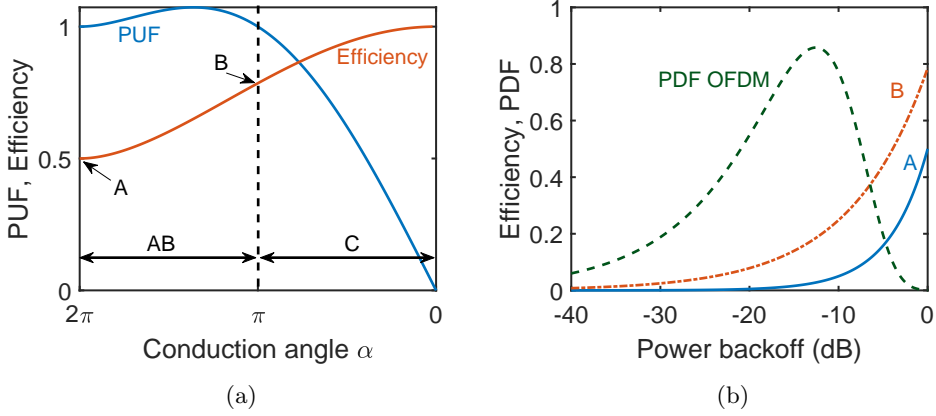


Figure 2.3: (a) RF-PA PUF and efficiency versus the conduction angle α . (b) Class-A (solid blue line) and Class B (dash-dotted red line) RF-PA efficiency for different power back-off levels together with the output power PDF of an OFDM signal.

angles $\alpha \in [0, 2\pi]$ is given by

$$\eta_{DE} = \frac{1}{2} \frac{\alpha - \sin(\alpha)}{2 \sin(\alpha/2) - \alpha \cos(\alpha/2)}. \quad (2.4)$$

Fig. 2.3(a) shows both the PUF and the RF-PA efficiency for different conduction angles. Note that in the ideal case, a class-A PA can only achieve an efficiency of 50%. Higher efficiency, up to 100%, can be achieved for lower conduction angles. However, linear amplifiers achieve this high efficiency at a low PUF [19]; the ideally 100% efficient linear amplifier has zero output power. Additionally, higher efficiency comes at the cost of increased non-linearity [19], thus degrading the quality of the transmitted signal as discussed later in this chapter.

Fig. 2.3(a) shows the maximum achievable efficiency, which occurs at minimum output power. Fig. 2.3(b) shows the efficiency of a class-A (solid blue line) and a class-B (dash-dotted red line) amplifier for different levels of power back-off, which shows that the efficiency of both these amplifiers drops significantly for lower output powers. Fig. 2.3(b) also shows the probability density function of an OFDM signal (number of sub-channels 64 using 16-QAM), describing the likelihood that the RF-PA operates at a certain back-off value. Note that when using modulated signals with a high PAPR (see chapter 1.2.4), such as QAM or OFDM, the RF-PA will almost never emit at

maximum output power. The expected value of the average efficiency of an RF-PA under modulation can be calculated if the probability density function (PDF) of the envelope of the modulated signal is known [36] and is given by

$$\eta_{mod} = E(\eta) = \int_0^\infty \text{PDF}(P) \eta_{PA}(P) dP. \quad (2.5)$$

For a baseband OFDM signal without clipping and a large number (> 64 [38]) of complex modulated sub-carriers the PDF of the instantaneous value of both the in-phase and quadrature amplitude components of the OFDM signal can be described by identical and independent Gaussian distributions with zero mean. Therefore the PDF of the instantaneous value of the envelope of an OFDM signal can be described by a Rayleigh distribution, resulting in a relatively high PAPR as shown in Fig. 2.3(c) by the dashed yellow line. When modulating a class-A and a class-B PA with an OFDM signal with an envelope V_{env} clipped at V_{clip} such that $P(V_{env} < V_{clip}) = 99.99\%$ the expected average efficiency is 5.5% and 23% respectively. This example emphasizes one of the biggest disadvantages of linear RF-PA's, which is the significant decrease in efficiency when amplifying signals with a complex modulation scheme to transmitting a signal with a constant envelope at the maximum output power.

2.2.2 Switched mode amplifiers

In contrast to linear amplifiers where the transistor is used as a transconductance, switched mode amplifiers use the transistor as a switch. Conventionally the active device is hard switched, resulting in only an on- and off-state for the active device. This hard switching limits the operating frequency of a switched-mode PA (SM-PA). However, improvements in CMOS technology increased the maximum operating frequency of SM-PAs, making them a viable option for modern RF-PAs.

Fig. 2.4(a) shows the class-E amplifier, which is one of the most commonly used SM-PA. It consists of a switch operated at the same frequency as the output frequency, a drain inductor L , a shunt capacitor C and a series tuned LC network. When the switch is turned on energy is stored in the inductor L and ideally the capacitor voltage $V_C = 0$, resulting in no power dissipation in the switch. When the switch is turned off the energy in the inductor L gained during the switch on period is fed to the load impedance Z , C and to

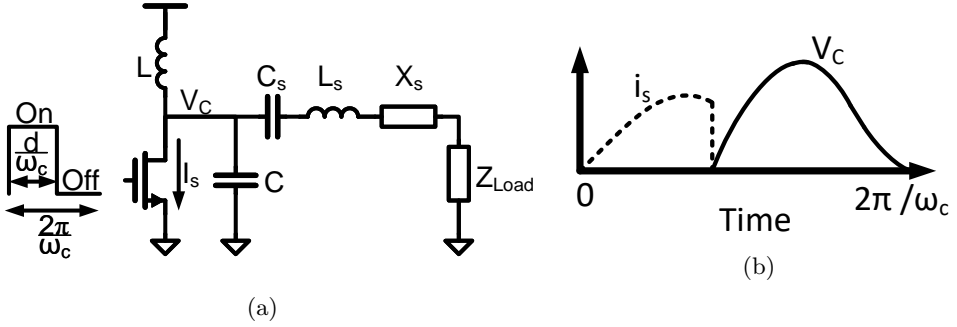


Figure 2.4: (a) Class-E RF-PA schematic. The transistor is hard switched between the on and off state. (b) Switch voltage and switch current during a single switch period.

the series LC network in case of finite Q . Depending on the values of L , C and X_S the drain capacitor voltage V_C meets the criteria in (2.6) and (2.7) [39]. These two conditions are called the zero-level switching (2.6) and zero-slope switching (2.7) conditions, which are both illustrated in Fig. 2.4(b).

$$V_C(2\pi/\omega) = 0 \quad (2.6)$$

$$\left. \frac{dV_C(t)}{dt} \right|_{t=\frac{2\pi}{\omega_c}} = 0 \quad (2.7)$$

The design of class-E amplifiers can be performed by using analytic equations derived in e.g. [39]. However the work in [39] assumes a static load impedance. The work in [40] showed that due to load variations, the peak drain voltage may become $13 \times V_{DD}$ for $|\Gamma| = 0.82$ (compared to $3.65 \times V_{DD}$ for $|\Gamma| = 0$) [40], possibly causing breakdown of the active device.

The class-E amplifier is inherently non-linear due to its switching nature: hard switching causes the output power to be (almost) independent of the input drive power. Because of this, the class-E amplifier on its own can only be used for simple modulation schemes such as on-off keying and phase modulation. To enable the use of a SM-PA together with complex modulation schemes, e.g. outphasing [41] or envelope elimination and restoration techniques [42] should be used (see section 2.4).

2.3 RF-PA distortion and complex modulation

The need for RF-PAs with high linearity came with the introduction of complex modulation schemes where both the amplitude and phase of the signal are modulated, such as QAM and OFDM. Distortion decreases the signal integrity and increases the occupied bandwidth, resulting in a decrease in channel capacity, spectral efficiency (see chapter 1.2) and overall wireless link performance [18, 19]. This section first discusses ways to describe the non-linear relationship between input and output of an RF-PA, after which the metrics that quantify the linearity performance of an RF-PA are described.

2.3.1 AM-AM and AM-PM

In modern communication standards the carrier signal is modulated by both an envelope signal $A(t)$ and phase signal $\varphi(t)$. Most active devices used in RF-PAs, such as transistors, exhibit a non-linear relation between input voltage and output current. Therefore, distortion at the output is dominated by the modulation of the envelope signal $A(t)$. The non-linear relationship between the input signal envelope and output signal envelope is a common source of distortion in RF-PAs and is also known as amplitude-to-amplitude (AM-AM) distortion. Additionally, most RF-PA's also exhibit an input signal amplitude dependent phase shift, which is known as amplitude-to-phase (AM-PM) distortion. The effects of both AM-AM and AM-PM distortion on the output signal can be described by [43]

$$V_{out}(t) = G(A(t)) \cos \left(2\pi f_c t + \phi(t) + \psi(A(t)) \right), \quad (2.8)$$

where $G(A(t))$ describes the AM-AM relation and $\psi(A(t))$ the AM-PM relation.

Both AM-AM and AM-PM distortion describe the periodic steady state non-linear effects of a RF-PA and are thus valid in a narrow-band. However, another source of distortion occurs that depends on the bandwidth of the input signal: memory effects inside the RF-PA. Memory effects can be classified into long and short time-constant effects [44, 45]. Phenomena and circuitry with long time-constants that cause memory effects in the PA are e.g. thermal effects, biasing networks and offset correction loops. Memory effects with a

short time-constant can be caused by e.g. matching networks, filters and the transition time of transistors.

2.3.2 EVM

Due to non-linear amplification by the RF-PA the transmitted constellation points e.g. in QAM modulation can deviate from their ideal locations, where the deviation can be described by an error vector. Fig. 2.5 shows ideal, measured and error vectors. For EVM measurements it is assumed that the transmitted symbols are measured by an ideal receiver. The error vector can be decomposed in a magnitude error and a phase error, which can be related to AM/AM, AM/PM distortion and noise in the RF-PA. In case of multi-carrier systems distortion will introduce a noise-like component in other sub-carriers (see section 2.3.3). The error vector magnitude (EVM) quantifies the RF-PA performance and is normally based on a large number of measurement samples. The RMS EVM is defined as [35]

$$\text{EVM}_{\text{RMS}}[\%] = 100 \times \frac{\sqrt{\frac{1}{N} \sum_{i=1}^N |S_{\text{ideal},i} - S_{\text{meas},i}|^2}}{\sqrt{\frac{1}{M} \sum_{i=1}^M |S_{\text{ideal},i}|^2}}. \quad (2.9)$$

where N is the number of samples, M the number of constellation points, and $S_{\text{ideal},i}$ and $S_{\text{meas},i}$ are the ideal and measured constellation points.

The deviation of the constellation points from their ideal locations may not be detectable if the error is not large enough the cross the decision boundary between adjacent constellation points. However, in case of a noisy environment these deviations might cause the transmitted constellation point to cross the decision boundary [46], which causes a bit error. This lowers the overall channel capacity (since we require a form of error correction to compensate for bit errors, or since the distance between constellation points must be increased which lowers the raw bit-rate/bandwidth) and thus lowers the overall spectral efficiency.

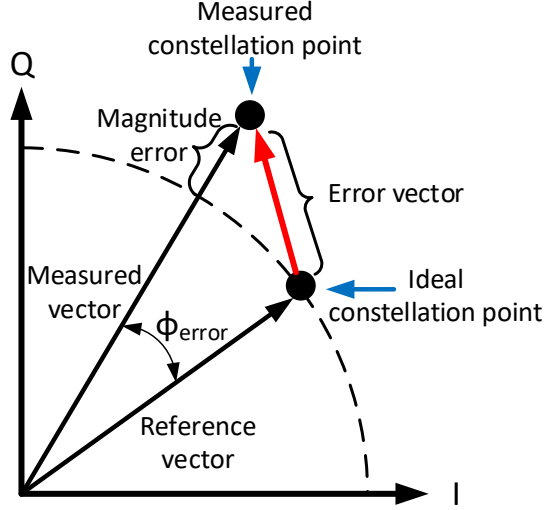


Figure 2.5: Illustration of the error vector concept. The error vector can be described by both a magnitude error and a phase error.

2.3.3 Intermodulation distortion

In case of multi-carrier systems such as OFDM or multi-band systems, non linear amplification causes intermodulation distortion. In contrast to harmonic distortion, intermodulation distortion causes frequency components at the sum and difference of the input frequencies. The effect of intermodulation distortion can be illustrated by a two tone input signal that is amplified by a non-linear amplifier.

The intermodulation frequency components in Fig. 2.6 around $(2\omega_1 - \omega_2)$ and $(2\omega_2 - \omega_1)$ are of special interest, since they end up relatively close to ω_1 and ω_2 . For example in OFDM the sub-carriers are closely spaced at a fixed frequency grid, hence the intermodulation distortion of two consecutive sub-carriers will end up in their neighbouring sub-carriers. Because of intermodulation, OFDM requires PAs with a higher linearity compared to single carrier systems. In multi-carrier systems the number of intermodulation products that end up in a single sub-carrier is proportional with the total number of sub-carriers, which is especially problematic in modern communication stan-

dards that can utilise > 1000 sub-carriers [3].

2.3.4 Spectral regrowth

In addition to in-band intermodulation distortion non-linear amplification distorts the transmitted constellation points and increases the spectral content of the transmitted signal (spectral regrowth). The distortion of the transmitted constellation points increase the EVM, whereas spectral regrowth can result in overlap of (sub-)channels, possibly reducing the SNR in the adjacent channels thus lowering the available channel capacity in these adjacent channels as stated by Shannon (see chapter 1.2). Note that there is a difference between the increase in spectral content between single-carrier and multi-carrier signals. For a single-carrier signal spectral regrowth is the main contributor to a increase in spectral content. For a multi-carrier signal the increased bandwidth is mainly caused by intermodulation distortion (see section 2.3.3), since the bandwidth of a single sub-carrier is relatively small compared to the full signal bandwidth. This section illustrates the cause and effect of non-linear amplification on a single-carrier QAM modulated signal.

Assuming that a QAM modulated signal

$$x(t) = x_I(t) \cos(\omega_c t) + x_Q(t) \sin(\omega_c t) \quad (2.10)$$

is applied to a non-linear RF-PA with primarily third order distortion according to:

$$V_{out} = \alpha_1 V_{in} + \alpha_3 V_{in}^3 \quad (2.11)$$

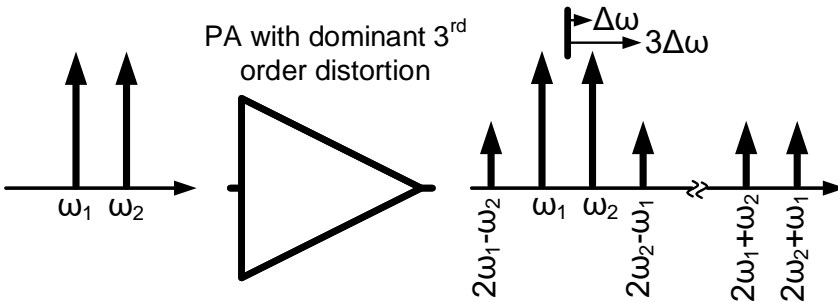


Figure 2.6: Resulting intermodulation products when amplifying a two tone signal by a RF-PA with dominant third order distortion

and assuming that the frequencies around 3ω are filtered out results in

$$\begin{aligned}
 V_{out}(t) = & \underbrace{\alpha_1 \left(x_I(t) \cos(\omega_c t) + x_Q(t) \sin(\omega_c t) \right)}_{\text{Linear component}} + \\
 & \frac{3\alpha_3}{4} \left(x_I(t)^3 \cos(\omega_c t) + x_Q(t)^3 \sin(\omega_c t) + \right. \\
 & \left. \underbrace{x_I(t)x_Q(t)^2 \cos(\omega_c t) + x_I(t)^2 x_Q(t) \sin(\omega_c t)}_{\text{Spectral regrowth}} \right) + \underbrace{\dots}_{\text{Out-of-Band}}, \tag{2.12}
 \end{aligned}$$

where the output signal $V_{out}(t)$ now contains contributions from $x_I(t)^3$ and $x_Q(t)^3$ centered around ω_c . Since the spectra of $x_I(t)^3$ and $x_Q(t)^3$ are broader than that of $x_I(t)$ and $x_Q(t)$, the spectrum of V_{out} is now wider than the spectrum of $x_I(t)$ and $x_Q(t)$, which is called spectral regrowth. Note that spectral regrowth only occurs for signals with a variable envelope [18]. Spectral regrowth not only introduces in-band distortion that degrades the users own link performance, but also causes leakage to neighboring channels that degrade the wireless link performance of other users. The difference in dB between the linear component and the third order regrowth component is

$$\Delta P = 20 \log_{10} \left(\frac{6}{4} \frac{\alpha_3}{\alpha_1} \overline{x_I(t)^2} \right) \tag{2.13}$$

assuming that $x_I(t)$ and $x_Q(t)$ are uncorrelated.

Fig. 2.7(a) shows the effect of spectral regrowth, where an input signal is applied to a non-linear amplifier and the resulting output spectrum is split in its linear (P_1) and third order (P_3) distortion components. Due to spectral regrowth the transmitted signal interferes with neighbouring channels. Because of this interference the SNR in the neighbouring channels decreases, resulting in a decrease of channel capacity. Most communication standards define the upper limit of radiated power as a function of frequency which we call the spectral mask. The spectral mask example is shown in Fig. 2.7(b) and the transmitted signals must stay below the spectral mask to meet the requirements.

2.3.5 Adjacent channel power leakage

As discussed in the previous section, non-linear amplification can increase the bandwidth of the amplified signal due to spectral regrowth. Because of the

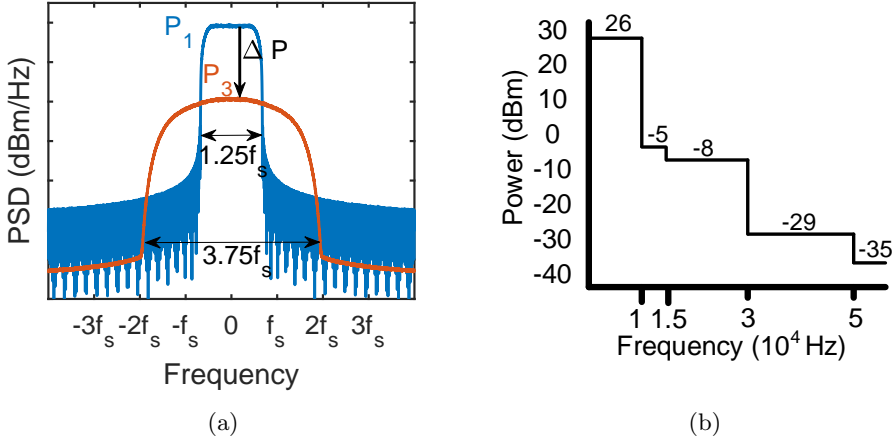


Figure 2.7: (a) Single carrier 1024-QAM signal with a RRC filter with $\alpha = 0.25$ after amplification by a non-linear RF-PA. The linear (P_1) and non-linear (P_3) contributions are split and the maximum power in $P_1 = 10\log_{10}(\overline{x_I(t)^2})$ and $P_3 = P_1 + \Delta P$, where $\Delta P = 20\log_{10}(\frac{6}{4}\frac{\alpha_1}{\alpha_3}\overline{x_I(t)^2})$. (b) The spectral mask example.

increased bandwidth the amplified signal is no longer only transmitted within the bandwidth of the main channel but also in adjacent channels as shown in Fig. 2.8. The ratio between the signal power in the main channel and transmitted in the adjacent channel is called the adjacent channel power ratio (ACPR) and defined as

$$\text{ACPR(dB)} = 10\log_{10}\left(\frac{P_{adj}}{P_{main}}\right) \quad (2.14)$$

where P_{adj} and P_{main} are the signal power in the adjacent channel and the main channel respectively.

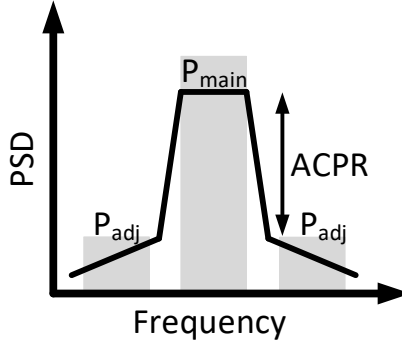


Figure 2.8: ACPR definition; P_{main} and P_{adj} are the power in the main and adjacent channels respectively.

2.4 Power back-off efficiency enhancement techniques

As described in section 2.2 the overall RF-PA efficiency is highest at maximum output power and decreases in back-off. Therefore the overall RF-PA efficiency reduces when amplifying signals with a high PAPR, which is the case for complex modulation (see chapter 1.2.4).

Several efficiency enhancement techniques exist, such as Doherty [47], outphasing [41] and envelope elimination and restoration. Most of these efficiency enhancement techniques improve the efficiency of the RF-PA compared to not using any efficiency enhancement. Using an efficient RF-PA as basis allows an overall higher efficiency. Therefore, this work will focus on switched mode RF-PAs (and especially class-E PAs), since they can (ideally) achieve 100% efficiency. Since Doherty can only be used with linear RF-PAs, thus this section will focus on outphasing and envelope elimination and restoration [42] techniques which both can be combined with switch-mode RF-PAs.

2.4.1 Envelope elimination and restoration

To improve the overall RF-PA efficiency under modulation the envelope elimination and restoration (EER) technique was proposed by Kahn in [42]; the concept is shown in Fig. 2.9(a). In EER the input signal is hence split into its envelope and phase component. The phase component is passed through a

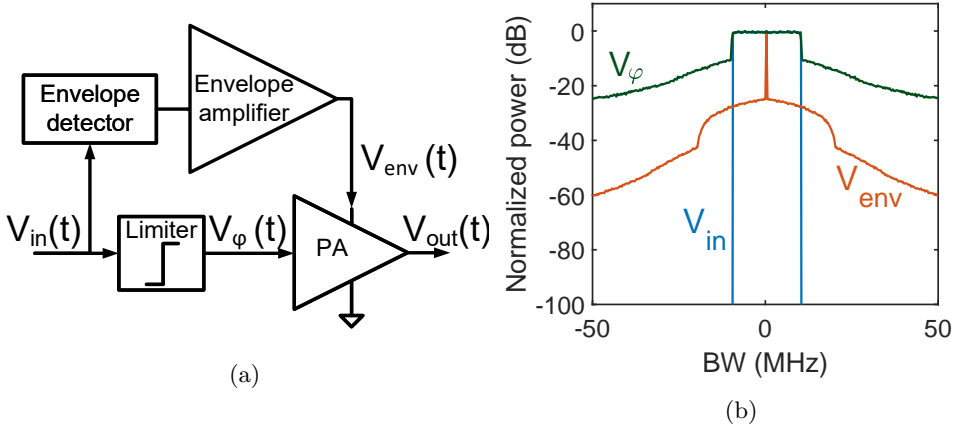


Figure 2.9: (a) Envelope elimination and restoration system diagram. (b) Simulated spectrum of a 20 MHz OFDM input signal (blue) and its envelope (red) and phase spectrum (yellow). Ideally the spectrum of the output signals is a scaled version of the input signal.

limiter, which drives the RF-PA and only modulates the output phase. Since the phase signal contains no amplitude information it can be used to drive an efficient amplifier such as a class-C or a SM-PA. To restore the input signal, the RF-PA output has to be modulated by the input signal envelope which in practice is achieved by modulating the power supply of the RF-PA. The envelope signal is buffered/amplified by an envelope amplifier that drives the RF-PA power supply, increasing the linearity and power constraints on the envelope amplifier. Due to the similarities with a polar representation of the signal, EER is also sometimes referred to as polar modulation.

The phase and envelope components are obtained by passing the input signal through a limiter and an amplitude detector respectively. Modern implementations of EER obtain the phase and envelope signals in the digital domain, which can easily be derived from the digital baseband signals. Since the RF-PA is driven by a constant amplitude, the effect of phase distortion due to amplitude changes at the input of the RF-PA are avoided, changing the requirements of the used RF-PA. However, any non-linearity caused by the envelope amplifier and any non-linear transfer from V_{env} to V_{out} will directly appear at the output of the EER system.

EER has some disadvantage over conventional linear amplification. Firstly,

a significant bandwidth expansion of the input signal results due to the conversion to polar coordinates [48]. An illustration of the bandwidth expansion due to the polar conversion is shown in Fig. 2.9(b). If the bandwidth of the envelope amplifier is smaller than the bandwidth of the envelope signal, or if there is any delay (which can be calibrated out) between the phase and envelope paths, out-of-band emissions will occur which impact the transmitted signal quality [48–50]. Secondly, an efficient envelope modulator is required, since its efficiency directly affects the overall EER systems efficiency. The work in [51] shows that 80% of the power of the envelope signal of a 802.11 a/g OFDM signal is between DC and 250 kHz. To boost overall efficiency, [51] proposes to combine an efficient buck-converter together with a high-bandwidth operational amplifier to form a high efficiency envelope amplifier. Other options for the envelope amplifier include class-G (dual supply) modulators [52] or class-S modulators [53]. Note that any non-linearity in the envelope amplifier will cause AM-AM distortion, but this can be partially compensated for by pre-distortion [19]. Furthermore the output impedance of the modulator should be such that it can efficiently provide the supply voltage of the RF-PA in Fig. 2.4.1(a).

2.4.2 Outphasing

The outphasing technique was proposed by Chireix in 1935 [41] and is shown in Fig. 2.10. An outphasing PA consists of two RF-PAs and a signal component separator (SCS). The SCS transforms the input signal

$$V_{in}(t) = |E_{in}(t)| \cos \left(\omega t + \phi(t) \right) \quad (2.15)$$

into two phase modulated constant envelop signals $s_1(t)$ and $s_2(t)$:

$$s_1(t) = \cos \left(\omega t + \phi(t) + \Delta\theta(t) \right) \quad (2.16)$$

$$s_2(t) = \cos \left(\omega t + \phi(t) - \Delta\theta(t) \right). \quad (2.17)$$

The outphasing angle $\Delta\theta$ is defined as

$$\Delta\theta = \cos^{-1} \left(\frac{|E_{in}(t)|}{E_m} \right), \quad (2.18)$$

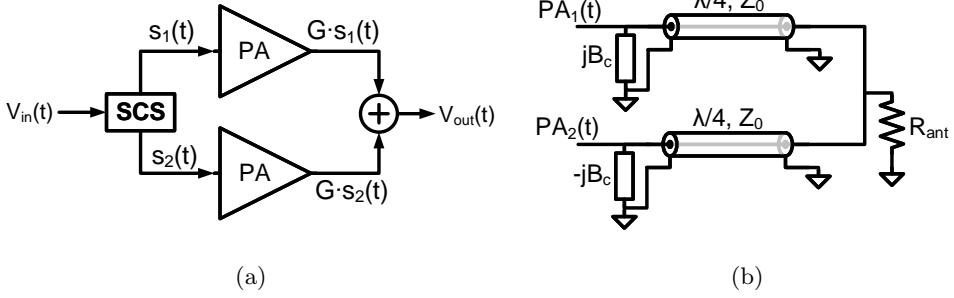


Figure 2.10: (a) Schematic overview of an outphasing PA. (b) Chireix transmission-line combiner.

where E_m is the maximum value of $|E(t)|$. Passing the two phase modulated signals $s_1(t)$ and $s_2(t)$ through two PAs with gain G and summing the two amplified signals results in an output voltage

$$\begin{aligned} V_{out} &= G \cos(\omega t + \phi(t) + \Delta\theta(t)) + G \cos(\omega t + \phi(t) - \Delta\theta(t)) \\ &= 2G \cos(\Delta\theta) \cos(\omega t + \phi(t)) = G \frac{|E_{in}(t)|}{E_m} \cos(\omega t + \phi(t)) \end{aligned} \quad (2.19)$$

Figure 2.11 illustrates the vector addition that takes place in an outphasing PA.

The outphasing RF-PA behaviour as described by (2.19) can be achieved by using an isolated power combiner, such as a Wilkinson combiner. An isolated power combiner allows the RF-PAs to always see their optimum load, resulting in a constant RF-PA power consumption over the entire out-phasing angle. This results in a power-backoff efficiency that is similar to that of the linear RF-PA, hence the efficiency at power-backoff is not improved [54].

Chireix [41] proposed a solution in which a non-isolating power combiner is used together with reactive compensation elements, allowing improvements of the system efficiency at power-backoff compared to using an isolated power combiner. Figure 2.10(b) shows a possible implementation of a non-isolation power combiner consisting of quarter-wavelength transmission lines and the Chireix compensation elements $\pm jB_c$. Because of the non-isolating power combiner the RF-PAs in the two branches load-pull each other. The effective

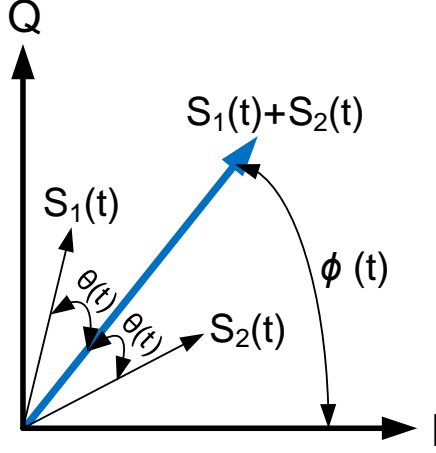


Figure 2.11: Illustration of the vector addition in outphasing.

load admittance Y_1 and Y_2 seen by respectively RF-PA 1 and 2 are [54]

$$Y_1 = \frac{2R_{ant}}{Z_O^2} \cos^2(\Delta\theta) - j \left(\frac{R_{ant}}{Z_O^2} \sin(2\Delta\theta) - B_c \right) \quad (2.20)$$

$$Y_2 = \frac{2R_{ant}}{Z_O^2} \cos^2(\Delta\theta) + j \left(\frac{R_{ant}}{Z_O^2} \sin(2\Delta\theta) - B_c \right) \quad (2.21)$$

where $B_c = \frac{R_{ant} \sin(2\phi_{comp})}{Z_O^2}$. This load-pulling results in a change in the effective load impedance seen by each of the RF-PAs. This allows a change in output power while the RF-PAs can always operate at their maximum voltage output. However, due to these load variations the maximum efficiency in a Chireix outphasing system can be achieved at two outphasing angles $\Delta\theta$. The efficiency of the outphasing system is given by [54]

$$\eta = \frac{2 \cos^2(\Delta\theta)}{\sqrt{(2 \cos^2(\Delta\theta))^2 + (\sin(2\Delta\theta) - \sin(2\theta_{comp}))^2}} \quad (2.22)$$

and the resulting efficiency is plotted in Fig. 2.12(a) versus the outphasing angle $\Delta\theta$ and in Fig. 2.12(b) versus the normalized output power for various compensation angles θ_{comp} .

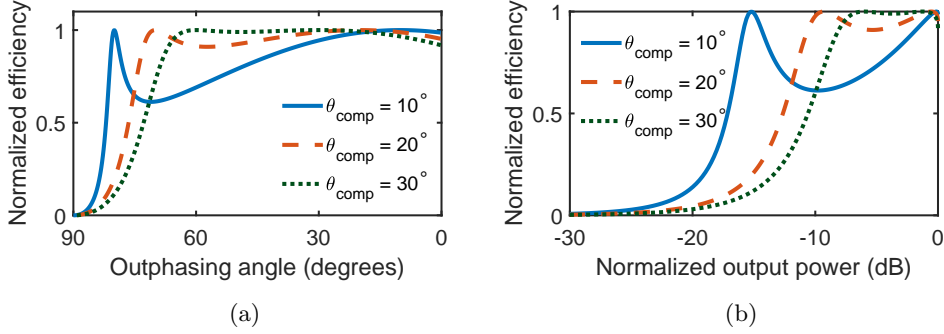


Figure 2.12: Outphasing system efficiency (a) versus outphasing angle. (b) Normalized output power.

Since the signals $s_1(t)$ and $s_2(t)$ have a constant envelope and are only phase modulated, switched-mode RF-PAs can be used in an outphasing amplifier, which can improve the overall amplifier efficiency compared to using linear amplifiers in an outphasing system. However the use of bulky power combiners makes it more difficult to fully integrate outphasing RF-PAs in CMOS technologies. Furthermore significant bandwidth expansion occurs when splitting $V_{in}(t)$ to $s_1(t)$ and $s_2(t)$, which increases the bandwidth requirements on the SCS and the RF-PA [55].

2.5 Linearisation Techniques

The increasing demands of modern communication standards for the RF-PA typically require some form of linearisation of the RF-PA to meet the spectral mask or to reduce EVM. This section describes some known RF-PA linearisation techniques.

2.5.1 Feedforward

In case of non-linear amplification, the output signal can be decomposed into a wanted linearly amplified signal and an unwanted error signal. In feedforward linearisation the error signal is estimated and subtracted from the amplified signal [19, 56], ideally resulting in only the linearly amplified signal at the output of the system. Figure 2.13 shows an example of a feedforward linearisation technique, consisting of a RF-PA, an attenuator and an error amplifier. Here the input signal is subtracted from the attenuated output of the RF-PA, resulting in the error signal $\epsilon(t)$. The error signal is then amplified by a factor A and subtracted from the RF-PA signal, ideally resulting in only the wanted linearly amplified signal at V_{out} .

The biggest advantage of a feedforward system is its stability [56, 57] (assuming that the amplifiers used are stable), but the feedforward linearisation technique also has some drawbacks. The first is the phase shift introduced by both the RF-PA and the error amplifier. These phase shifts result in phase shifts between the input signals to the subtractors, degrading the cancellation

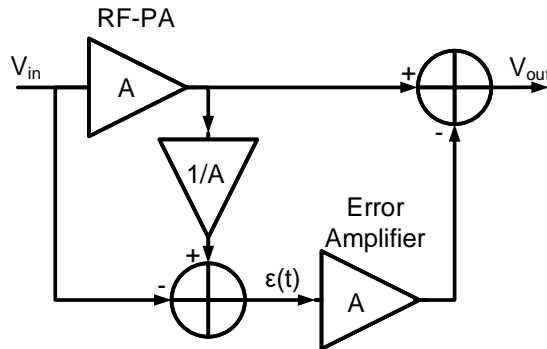


Figure 2.13: Feedforward linearisation technique, where A is the gain of the RF-PA.

of the error signal at the output V_{out} . These phase shifts can be compensated for by inserting delay elements in the path from V_{in} to the subtracter input and just before the positive input of the subtracter at the output. Another disadvantage is the use of the subtracter at the output, since any loss in the output subtracter directly degrades the overall RF-PA efficiency.

2.5.2 Envelope Feedback

Another common way to linearise amplifiers is by means of negative feedback. A possible implementation of negative feedback is by using envelope feedback [58] as shown in Fig. 2.14. The envelopes of the input signal and the output signals are compared and the error signal is used to tune the RF-PA input signal. Envelope feedback can only compensate for AM-AM distortion. AM-PM is not corrected by envelope feedback and envelope feedback can even create extra AM-PM distortion due to the amplitude control action [19].

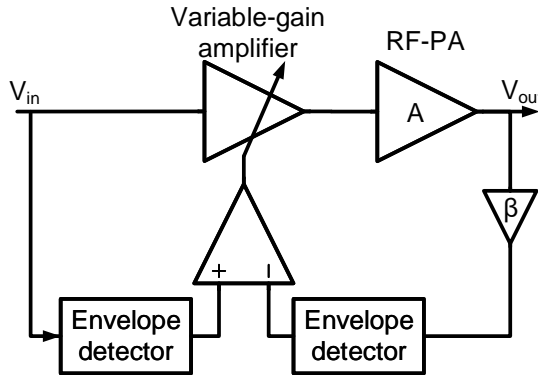


Figure 2.14: Envelope feedback technique.

2.5.3 Cartesian Feedback

Cartesian feedback is a linearisation technique that requires the baseband I and Q components, hence it can only be used in full transmitter systems where the I and Q signal components are readily available. A schematic overview of a Cartesian feedback system is shown in Fig. 2.15. In Cartesian feedback the RF-PA output signal is down converted to baseband by means of a quadrature mixer, resulting in both the I and Q components of the transmitted signal. The

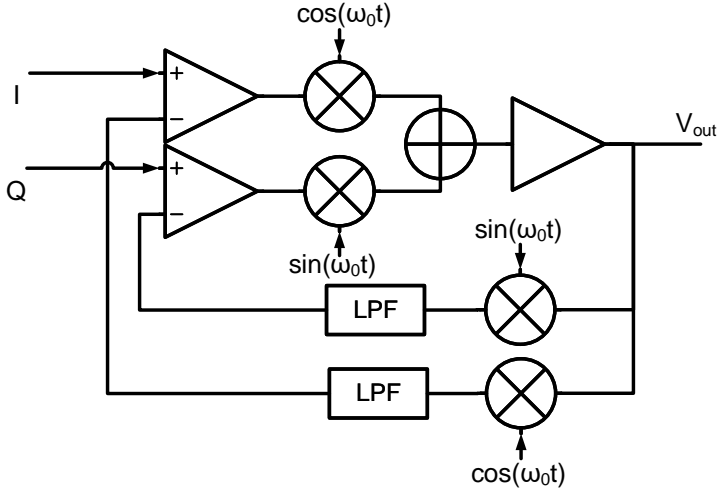


Figure 2.15: Cartesian feedback loop.

down converted I and Q signals are compared with the input I and Q signals, after which the difference is amplified, up-converted and fed to the RF-PA. In this way a negative feedback loop is created, that attempts to make V_{out} equal to the (ideally) up-converted I-Q signal.

An advantage of cartesian feedback is that it uses two decoupled symmetric feedback paths with (ideally) equal gain and bandwidth, reducing the phase-shift between AM-AM and AM-PM processes which is the primary reason for asymmetric IM-sidebands and spectral regrowth [19]. However, the two feedback loops are only decoupled under ideal conditions. Due to phase shifts of the RF-carrier caused by reactive loads, RF-PA delay and delay in the LO the two feedback loops are coupled, reducing the loop stability [59].

2.5.4 Pre-distortion

RF-PAs have a strong trade-off between linearity and efficiency [19], hence efficient RF-PAs typically require some form of linearisation to meet the specifications for modern communication standards. Pre-distortion is a technique in which the input signal is altered in such a way that after amplification by the RF-PA (ideally) only the original input signal is present. Fig. 2.16 shows a typical pre-distortion setup. First the input signal is fed to the pre-distortion

function F , after which the output of the pre-distortion function is fed to the RF-PA with transfer function G . To obtain a linear transfer from P_{in} to P_{out} F is chosen in such a way that $P_{out} = G(F(P_{in})) = K \cdot P_{in}$. Conventionally the function F has some form of gain expansion since most RF-PAs suffer from gain compression due to e.g. limited power supply voltages. Pre-distortion has some drawbacks: its performance is influenced by both PVT and antenna impedance variations (see chapter 7), it cannot correct for abrupt non-linearities [18] and memory effects significantly increase the complexity of pre-distortion.

Pre-distortion of the RF-PA can be implemented in both an analog and digital way. In analog pre-distortion a non-linear device, such as a diode or a non-linear amplifier, is used to create the pre-distortion signal which conventionally has an expanding characteristic [60]. Analog pre-distortion typically has simple structures, low cost and can directly work on the RF-signal, without the need of any extra (base-band) information [61] and focus on cancelling third order distortion. However the complexity of analog pre-distortion significantly increases when cancelling higher order distortion [60]. Furthermore analog pre-distorters are designed within a certain operating point, hence any deviations from this point will reduce the effectiveness of the analog pre-distorter.

With the improvements in CMOS technologies digital pre-distortion (DPD) became more attractive due to its flexibility. Another factor that enables DPD is the availability of the baseband signal in the digital domain [19], which will only be directly available in a full transmit system. DPD can be implemented by a lookup table and can even be made adaptive by using feedback from the RF-PA improving the performance and robustness of the RF-PA [62, 63].

In case of an RF-PA with memory effects the complexity of DPD increases significantly compared to a memory-less DPD. Conventionally a Volterra series is used to describe the non-linear behaviour of RF-PAs that have (significant) memory effects [64]. Conventionally the Volterra series only compensates for the non-linear amplification at a single operating point. Any change in the operating point (e.g. temperature, load impedance, supply voltage, process spread) where the linearisation is performed can significantly limit the ability of the pre-distortion to linearise the RF-PA. Chapter 4 proposes a technique that can characterize the RF-waveform, allowing the pre-distortion to be op-

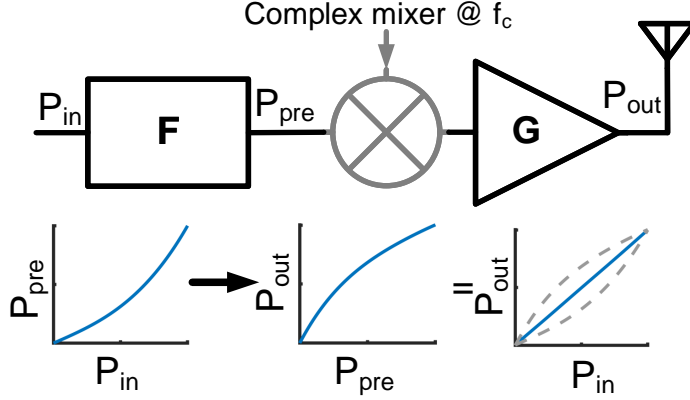


Figure 2.16: Pre-distortion schematic, where the mixer is optional depending on if the pre-distortion is applied on a RF-signal or the baseband signal. The function F is the pre-distortion function and G represents the non-linear behaviour of the RF-PA. The different transfer functions for each block are shown below.

timized for the current operating conditions of the RF-PA. Pre-distortion of RF-PAs with memory effects is still possible [65], even with a more simplified model than the Volterra series. Simplification of the model results in fewer coefficients for the pre-distortion polynomial, reducing the complexity of implementing the pre-distortion algorithm. However, even if pre-distortion can compensate for short time-constant memory effects caused by bandwidth limitations in the matching networks and filters, long time constant memory effects caused by changes in e.g. load impedance variations, temperature and supply voltage can still degrade the pre-distortion effectiveness.

2.6 PA-breakdown

The RF-PA deals with relatively high currents and voltages that can be (significantly) higher than the supply voltage. If these voltages and currents exceed the maximum values of the device, the performance of the RF-PA can be significantly reduced and even fully break the RF-PA. This section discusses some of the most common breakdown-effects in RF-PAs.

2.6.1 Gate-oxide breakdown

The maximum gate-source and gate-drain voltage decreased with the advances in CMOS, due to a decrease in the thickness of the gate-oxide. When the thickness of the gate oxide decreases direct tunnelling current (≥ 5 MV/cm field strength in the (equivalent) SiO_2 oxide thickness.) becomes more dominant [66] compared to Fowler-Nordheim tunnelling (≥ 10 MV/cm). The tunnelling current that flows through the gate-oxide can cause defects in the oxide, even though the current is significantly smaller compared to the Fowler-Nordheim tunnelling current. These defects can create an ohmic path between the gate and the underlying silicon [67], which permanently damages the device.

The work in [68] describes the effect of gate-oxide breakdown on the RF-performance of a NMOS transistor. Even though the device remains operational when some of the fingers in the transistor exhibit gate-oxide breakdown the RF-performance is degraded significantly. However, gate-oxide breakdown has some frequency dependence showing an increase in the voltage headroom for higher frequencies [69], thus improving reliability at RF-frequencies compared to having (quasi) DC stress levels.

2.6.2 Hot carrier degradation

Modern CMOS technologies allow for short channel length devices. A high voltage (e.g. >1.2 V in 65nm) over a short channel device results in a high lateral electric field that accelerates the carriers. Some of these carriers achieve a very high energy and are called "hot energy carriers". These hot carriers can collide with the lattice before arriving at the drain, which can cause impact ionization. Impact ionization can cause surface defects, which can reduced the

carrier mobility increasing the on-resistance of the device. Furthermore impact ionization can cause trapped charge in the gate-oxide or oxide/silicon interface. This shifts the local threshold voltage resulting in an increased on-resistance of the device, which degrades the CMOS RF-transistor performance.

Hot carrier degradation requires simultaneously a high drain current and a high drain-source voltage [67] in the active device. This makes linear amplifiers prone to hot carrier injection, since they can have simultaneous a high voltage over the active device while current flows through it. In SM-PAs this overlap is ideally prevented, making SM-PAs less prone to hot carrier degradation.

2.6.3 Punch-through

In a standard CMOS process, the transistor's drain-bulk and source-bulk diode are normally reverse biased. If a high enough voltage is applied to the drain, the depletion layer of the drain-bulk diode extends to the depletion layer of the source-bulk diode, which lowers the potential barrier that stops current from flowing between the drain and source [67]. Note that this current can exist even without any significant gate-bias and can create its own hot-carriers. These hot-carriers can damage the interface between the silicon and the gate-oxide when a collision with a high enough energy occurs, thus degrading the performance of the CMOS RF-transistor. In contrast to gate-oxide breakdown and hot carrier degradation, punch-through does not directly affects the RF-PA performance [20]. However, when the punch-through current is sustained it can result in thermal failures.

2.6.4 Drain-bulk breakdown

As discussed in the section about punch-through standard CMOS has a drain-bulk diode, where the bulk is conventionally connected to a fixed potential. This diode has a reverse-breakdown voltage, hence it is important to keep the drain-bulk voltage below the break-down voltage [67]. In a 65nm CMOS process this break-down voltage is above 10 V, hence drain-bulk breakdown normally poses no serious problem for RF-PA designs.

2.6.5 Electromigration

Electromigration is the transport of mass in metals when the metal is stressed at high current densities. Due to the decreasing CMOS feature size the current densities in the interconnections has increased, resulting in a higher change of failure due to electromigration [70]. In case of RF-circuits electromigration can induce delay failures, before eventually opens or shorts in the interconnect occur due to the transport of mass [71].

2.7 Thesis outline

CMOS technology can be used to enable highly integrated transceivers. However, the maximum allowable voltages decreased with newer CMOS nodes which poses challenges for the reliability and output power of CMOS RF-PAs. Furthermore, external influences might change the antenna impedance which can degrade the RF-PA performance and possibly even permanently damage the RF-PA. Additionally modern communication standards use complex modulation to improve spectral efficiency, which require linear RF-PAs and reduces the overall RF-PA efficiency.

This thesis aims at improving the performance, reliability and robustness of CMOS RF-PAs and in particular the class-E RF-PA. The focus is on in-chip measuring the RF-waveform in a RF-PA and using the acquired information to improve performance, reliability and robustness. Previous works used sensors that registers properties of the RF-waveform such as peak-voltage, DC-level or power sensors [72, 73] which tune bias networks or load impedance tuners to improve performance, reliability and robustness. This effectively implements a transmitter system that adapts its properties to maintain maximum performance under PVT and load impedance variations. The used sensors should not significantly increase the power consumption and occupied area. However, the previous mentioned sensors all give indirect information on the waveforms in and around the PA, whereas actual waveforms determine the RF behaviour (and performance) of the PA. If the RF-waveform shape is know it can be used to improve efficiency by means of waveform shaping [36] or it can be used in adaptive digital predistortion (ADPD) systems to improve linearity.

The structure of this thesis is as follows:

- Improving the performance and reliability of RF-PAs requires information about their operating conditions. Chapter 3 describes the use of N-path circuits for voltage measurements in RF-PAs. First it will give a short introduction into N-path circuits and their operation. Afterwards the major differences between N-paths for RF-PA measurements and receivers are discussed, since conventionally N-path circuits are primarily used in receivers.
- Chapter 4 discusses the design of an RF-waveform characterizer that measures the DC component and the first 3 harmonics of RF signals by applying a DFT to 8 (ideally) equally spaced quasi-DC output voltages. Conventionally in these types of systems accuracy is limited by sample timing accuracy, which in our case are mainly due to delay cell mismatch. A novel way to cancel delay cell mismatch is introduced, that significantly increases measurement accuracy at the cost of only a small power and area increase.
- Chapter 5 introduces a technique that allows an increase in the Nyquist-Shannon bandwidth by sampling a RF-waveform at two non-integer multiple sample rates. This technique can be combined with the RF-waveform characterizer from Chapter 4 to increase the number of harmonics that can be characterized, while only requiring a small area and power overhead. This allows the implementation of a self-adaptive TX system, increasing both the overall performance and robustness against both PVT and antenna load variations.
- Chapter 6 describes a technique to self-protect class-E PAs to decrease their sensitivity to load variations, relying on tuning of the switch-tank relative-resonance frequency, implemented by an on-chip Switched-Capacitor Bank (SCB). To validate the technique, load-pull measurements are conducted on a class-E PA implemented in a standard 65nm CMOS technology, employing an off-chip matching network, augmented with a fully automated self-protective control loop.
- Chapter 7 demonstrates a polar class-E PA with an on-chip waveform characterizer enabling adaptive digital pre-distortion (ADPD) to preserve the linearity of the PA under load mismatch. The presented ADPD

corrects both AM/AM and AM/PM distortions, which are prominent in the demonstrated PA, while simultaneously correcting for slow memory effects without the need for complex memory DPD algorithms. Load-pull measurements demonstrate that target EVM and adjacent channel power ratio (ACPR) can be maintained in a significantly larger area on the Smith chart going from 50Ω optimized static DPD to our ADPD for a 2 GHz 1024 QAM signal with 1 MSym/s symbol rate.

- Chapter 8 summarizes each chapter along with the original contributions found in this thesis. Afterwards recommendations for future work to improve RF-PA performance are given.

Chapters 4,6 and 7 are reformatted from published work in [74–76] and chapter 5 is reformatted from work that is currently accepted for publication in a future edition of the IEEE Transactions on Circuits and Systems I: Regular Papers.

Chapter 3

N-path circuits

The increasing number of wireless devices resulted in a crowded radio spectrum, which requires receivers that can select only the wanted signal band to enable reliable wireless links. Therefore high-Q filtering is important to improve receiver selectivity, for which traditional receivers use surface acoustic wave (SAW) filters at the input of the receiver. However, these SAW filter are bulky and inflexible, which is unwanted for programmable and flexible receivers. To reduce the required area and cost of the filter, implementation and integration of the filter in CMOS is preferred.

In 1947 Barber proposed a technique based on switches and capacitors that could achieve programmable high-Q filtering [77], but this technique relied on mechanical components for switching the capacitors. N-path circuits (or commutated networks as they are called in [78]) consist of N switch-R-C networks and a programmable clock frequency. The advances in CMOS technologies enabled better switches, higher capacitor densities and programmable high frequency clocks, making N-path circuits ideal candidates for integration in advanced CMOS technologies.

N-path circuits are conventionally used in mixer-first receivers [79, 80], since they can simultaneously achieve programmable high-Q filtering and highly linear down-conversion of the RF-signal. The high linearity of N-path circuits enables measurements of relatively high voltage waveforms, such as found in an RF-PA. However, using N-path circuits to characterize an RF-PA in a transmitter, changes the N-path requirements compared to those in a receiver. This chapter first gives an introduction into the operation of N-path

circuits after which the differences between using a N-path circuit in a waveform characterizer in a transmitter and in a receiver are discussed. Finally the effects of sampling bandwidth and timing accuracy on the output waveforms are discussed.

3.1 Operation

The top of Fig. 3.1 shows the schematic of an N-path circuit, where $N=8$. It consists of a signal source with source resistance R and 8 switched capacitors C that are clocked at f_s . It is assumed that during operation the capacitors in the N-path filter are sequentially connected to the resistor for a duration of $T_{on} = \frac{1}{Nf_s}$ and that only a single switch is conducting at the same time to prevent cross talk between the capacitors. When a switch is conducting, the respective capacitor is connected to the resistor and depending on the RC-time constant (partially) charged to the RF-input voltage.

The RC time constant plays a major role in the circuits behaviour. Two operation modes of the N-path circuit can be distinguished based on the RC

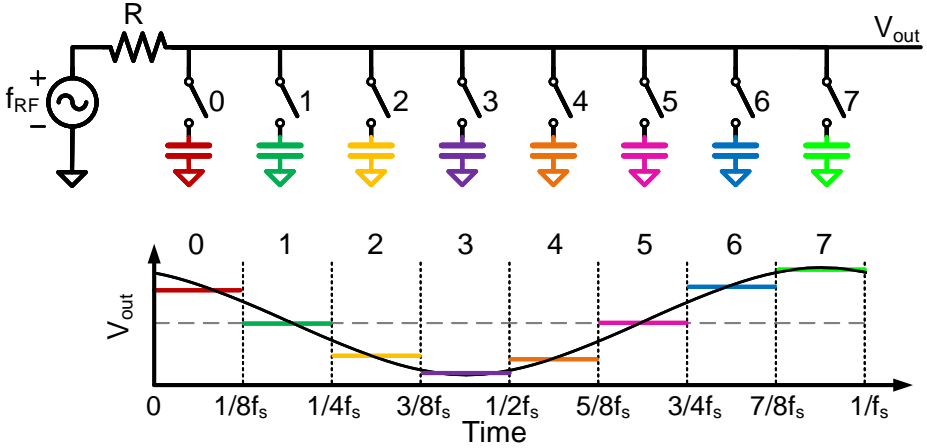


Figure 3.1: N-path switched R-C filter where $N = 8$, $f_{RF} = f_s$, $T_{on} = \frac{1}{Nf_s}$ and $T_{on} \ll 2RC$. The top part shows the circuit, while the bottom part shows the time-domain waveform of V_{out} . Here the solid black line is the RF-input signal, while the horizontal lines correspond to the voltage on the capacitor directly above.

value and the on-time of the switch [81]:

$$\text{Sampling region:} \quad T_{on} \gg 2RC \quad (3.1a)$$

$$\text{Mixing region:} \quad T_{on} \ll 2RC \quad (3.1b)$$

In case that the N-path circuit operates in the sampling mode, the capacitor voltages settle to (almost) the input voltage within the on-period of the switch. However, in the mixing region the capacitor voltages in the N-path circuit will only settle to the input signal over many cycles of the clock and only if $f_{RF} \approx nf_s$, where $n \in \mathbb{Z}$. The bottom of Fig. 3.1 shows the steady-state output waveform of a N-path circuit operating in mixer mode, where the colours in the waveform match the voltage on the corresponding capacitor and $f_{RF} = f_s$. In case that the input frequencies are not close to the switching frequency the capacitors will see different parts of the input signal, hence the capacitor voltage will on average have a mean of zero resulting in filtering of the RF-input signal.

The work in [82] shows that N-path filters operating in the mixing region exhibit narrow-band, high-Q filtering and a lower noise figure compared to sampling mode operation, hence N-path filters in receivers are conventionally used in the mixing region. In [83] the harmonic transfer function of a single kernel (single switch-R-C circuit) in the N-path filter is derived and is given by

$$H_{eq}(f) = \frac{1}{1 + j2\pi fRC} \frac{1 - \beta e^{-j2\pi fT_{on}}}{1 - \beta e^{-j2\pi fT_s}}, \quad (3.2)$$

where $\beta = \exp(-\frac{T_{on}}{RC})$ and $T_s = \frac{1}{f_s}$. Fig. 3.2 shows the magnitude of the harmonic transfer function $H_{eq}(f)$ of a N-path filter. Note that in case $T_{on} = \frac{T_s}{N}$ the N-th harmonic is cancelled.

The bandwidth of a N-path filter depends on the values of R, C and the number of paths. In case that the capacitor is only connected to the input for $\frac{1}{N}$ -th of the clock period, the resistance is effectively increased by a factor N. The N-path filter bandwidth is given by [78]

$$f_{-3dB} = \frac{1}{\pi NRC}. \quad (3.3)$$

The N-path filter can also be used as a passive mixer, when instead of using the voltage V_{out} the voltages over the capacitors are used. Since the RF-signal

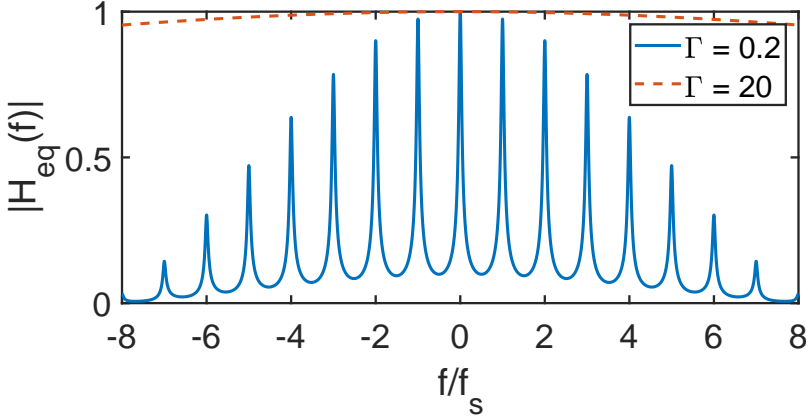


Figure 3.2: Harmonic transfer function $|H_{eq}(f)|$ of a N-path ($N=8$) filter where $T_{on} = \frac{T_s}{N}$ and $\Gamma = \frac{T_{on}}{RC}$.

is multiplied with the LO, which conventionally is a square wave, not only the RF-band at the LO frequency is down-converted but also bands around multiples of the LO as described by (3.2). In case of a direct-downconversion mixer the down-converted signals become indistinguishable from the harmonic images, which can be stronger than the desired signal. Traditionally these harmonic images can be removed by means of a filter at the RF-input, however these filters are bulky and inflexible.

Another solution to reject harmonic images from degrading the quality of the desired signal is to reduce the effective harmonic content of the LO waveform. The work in [84] implements a harmonic rejection receiver by over-sampling the RF-input by 8 times, after which a discrete time (DT) mixer down-converts the signal. The DT mixer as shown in Fig. 3.3(a) periodically weighs the input samples by either ± 1 or $\pm 1 + \sqrt{2}$, which correspond to the coefficients of a sine or cosine with frequency f_c sampled at $8f_c$. This enables the signal around f_c to be down-converted without the harmonic images at $2f_c$ to $6f_c$.

The work in [85] proposes a two stage poly-phase harmonic rejection mixers, which is shown in Fig. 3.3(b). Here harmonic rejection is achieved by two-stage iterative weighting and summing of the RF-input signal, which significantly improves the harmonic rejection over traditional mixers with only a single stage [85].

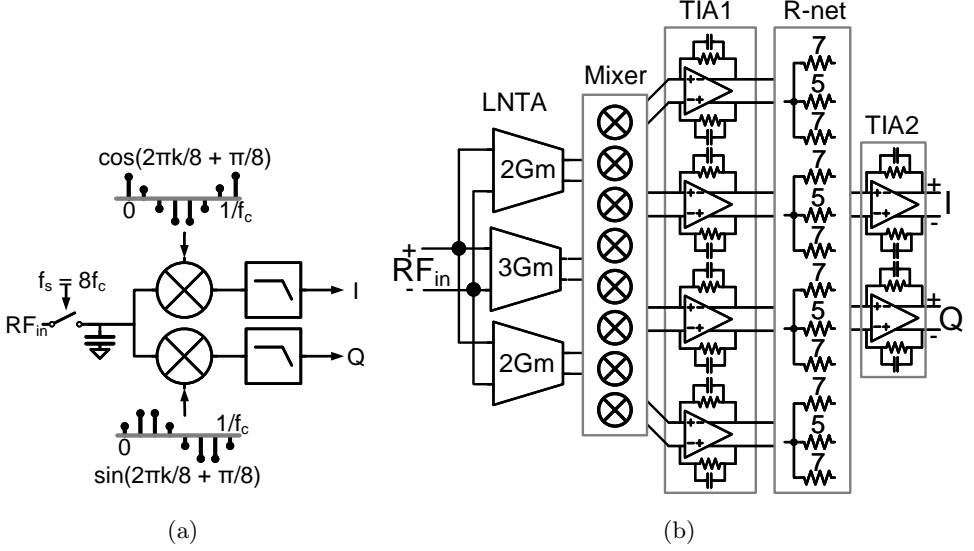


Figure 3.3: (a) The DT mixer from [84]. (b) Two stage harmonic rejection in N-path mixers as described in [85].

3.2 Receiver vs Waveform characterizer

When using a N-path receiver as a waveform characterizer in an RF-PA, different design choices can be made compared to the design of a conventional receiver. This section describes the major differences between N-path circuits in receivers and using one in transmitters, such as harmonics, signal strength, noise and input impedance.

3.2.1 Harmonics

In wireless communication the wanted signal is normally centred around a single carrier frequency, hence most receivers are build to select only a certain band around the carrier frequency while suppressing all other bands. In contrast to signals at the input of a receiver, signals inside an RF-PA can contain higher harmonics of the signal. Note that signals at the antenna of the RF-PA are typically filtered, hence higher harmonic content is (significantly) suppressed. To fully characterize the RF-PA these higher harmonics are important, since they may be used as indicators for the efficiency, linearity and reliability of the RF-PA. Therefore the proposed system will measure relevant

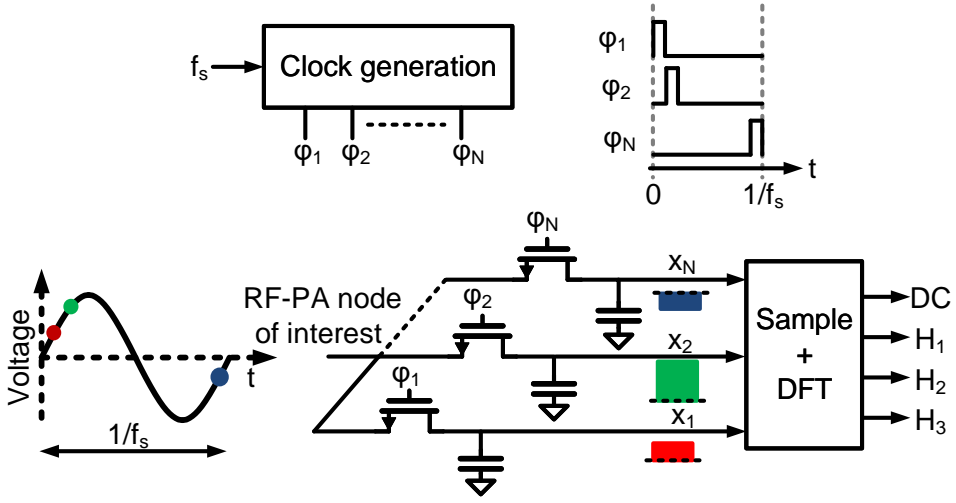


Figure 3.4: Schematic overview of the RF-waveform characterizer.

internal nodes of the RF-PA, which can contain higher harmonics of the RF signal.

Figure 3.4 shows a schematic overview of a circuit that can measure the harmonics of an RF-waveform; further on this system is denoted as an RF-waveform characterizer. It consists of a clock generation circuit connected to N passive mixers, that down-convert the RF-waveform with N time-shifted non-overlapping clocks. Due to the phase transparency of the passive mixer each of the capacitors contains a phase shifted down converted version of the input signal, where the phase depends on the LO phase.

In the waveform characterizer it may be required to separate the fundamental frequency and its multiples, to allow separate characterization of e.g. the AM-AM, AM-PM and intermodulation products. Separating the harmonics can be done by mixing with 8 equally spaced phases, comparable to conventional N -path mixers with harmonic rejection [85, 86]. Instead of weighting and summing the voltages over the capacitors in the analog domain they are converted to the digital domain instead as shown in Fig. 3.4. The complex magnitude of the signal harmonics can be acquired by performing a discrete

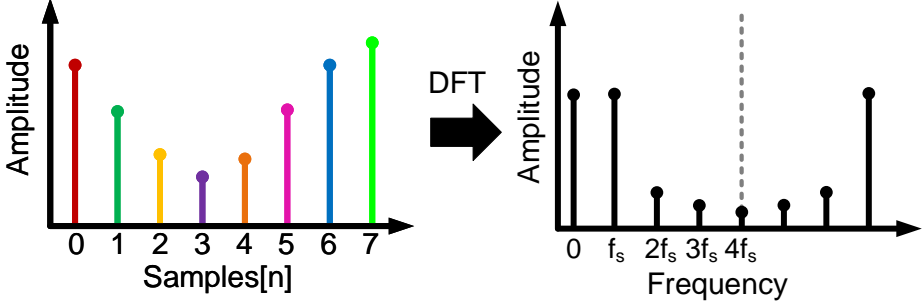


Figure 3.5: Capacitor samples and the DFT of these samples. The clocks for each path in the N-path circuit are spaced by $T_s = \frac{1}{f_s}$, which results in a f_s spacing in the frequency domain. This allows characterization of the harmonics of the RF-input signal.

Fourier transform (DFT)

$$X_k = \sum_{n=0}^{N-1} x_n e^{-jkn \frac{2\pi}{N}}, \quad (3.4)$$

where x_n is the sampled voltage of the n-th capacitor and X_k is the set of complex magnitudes. In case that f_s is equal to the center frequency of the transmitted signal, the set X_k corresponds to the complex magnitude of the harmonics of the RF-input signal. Fig. 3.5 shows an example of the capacitor voltages and the resulting DFT. Here an 8-point DFT is performed, resulting in both magnitude and phase information about the DC voltage and the first 3 harmonics of the RF-signal. Since discrete-time samples are used, aliasing occurs that affects the estimation accuracy of the complex amplitudes of the RF-waveform harmonics.

In case that the N-path circuit operates in mixer mode $T_{on} \ll RC$ and assuming that $f \approx mf_s$ the ratio between the conversion gain of the higher harmonics ($m \neq 1$) compared to the first harmonic ($m = 1$) can be approximated by [83]

$$\left| \frac{H_{eq}(mf_s + \Delta f)}{H_{eq}(f_s + \Delta f)} \right| \approx \left| \frac{\text{sinc}(mD)}{\text{sinc}(D)} \right|. \quad (3.5)$$

Hence, to use the N-path circuit to characterize higher harmonics in an RF-PA requires gain compensation for the higher harmonics, which can easily be

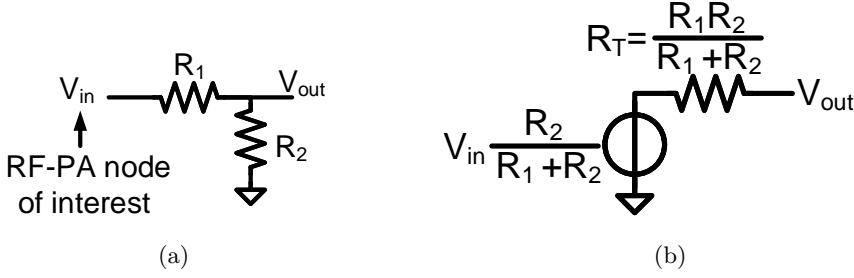


Figure 3.6: (a) Resistive divider to attenuate the RF-PA signal of interest so that it can be measured by the waveform characterizer. (b) Thévenin equivalent of the resistive divider.

performed in the digital domain.

3.2.2 Signal strength

The power of a received signal and a transmitted signal can be orders of magnitude apart, hence the requirements on the input of the N-path circuit differs for both scenarios. Conventionally the RF-PA signal has to be attenuated before it can be measured by the RF-waveform characterizer to maintain linearity and to prevent breakdown of the switches.

A simple implementation of a signal attenuator is the resistive voltage divider as shown in Fig. 3.6(a), where its Thévenin equivalent is shown in Fig. 3.6(b). Figure 3.7 shows the resistive divider, where the output is connected to the RF-waveform characterizer. The gain of the (loaded) attenuator is

$$A_L = \frac{R_2 / Z_{in}}{(R_1 + R_2 / Z_{in})}. \quad (3.6)$$

Here Z_{in} is the input impedance of the RF-waveform characterizer, which for frequencies close to the switching frequency (or multiples of the switching frequency) is approximately given by [87]:

$$Z_{in}(n f_s) = \frac{H_{0,SW}(n f_s) R_T}{1 - H_{0,SW}(n f_s)} \quad (3.7)$$

$$H_{0,SW}(n f_s) \approx \frac{2N \left(1 - \cos(2\pi n D) \right)}{4D(n\pi)^2} + (1 - ND) \quad (3.8)$$

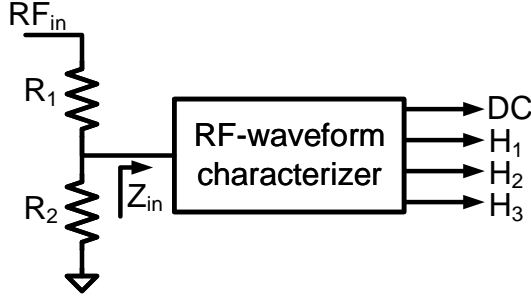


Figure 3.7: Resistive attenuator followed by the RF-waveform characterizer. Z_{in} is the impedance looking into the RF-waveform characterizer.

Assuming that $N = 8$ and $D = \frac{1}{8}$ yields $Z_{in} \approx 18.85R_T$ where the Thévenin equivalent resistor $R_T = \frac{R_1 R_2}{R_1 + R_2}$ for frequencies around the fundamental frequency. By using equation (3.7), the Thévenin equivalent resistor R_T and assuming that $D = \frac{1}{N}$ the loaded gain A_L can be calculated by

$$A_L = \frac{R_2}{R_1 + R_2} \frac{N^2(1 - \cos(2\pi n D))}{2(\pi n)^2}. \quad (3.9)$$

In contrast to a receiver, the input impedance of the waveform characterizer should be high to reduce the impact on the measured node. This allows for small switches, resulting in a high input impedance and a reduction in the required clock power compared to that in a standard receiver design. The impedance seen from the RF-PA is equal to $R_{in} \approx R_1 + R_2$, which can be designed as a high ohmic load, preventing significant loading of the RF-PA. Note that attenuation, input resistance and bandwidth are all depending on the values of R_1 and R_2 , which introduces design trade-offs.

Clock feed-through of the waveform characterizer can cause unwanted signals to be injected into the RF-input node. These injected signal might be radiated by the antenna, possibly resulting in violations of the spectral mask and an increase in EVM. The resistive attenuator also increases the reverse isolation between the RF-waveform characterizer and the RF-input node. Figure 3.8 shows an example of a signal that is injected into the resistive divider, where H_1 , H_2 and H_3 correspond to the harmonics of the RF-PA center frequency. The transfer from the RF-waveform characterizer to the RF-input

is

$$H_{\text{reverse}} = \frac{R_1 Z_{PA}}{R_1 + Z_{PA}}. \quad (3.10)$$

Conventionally $R_1 > Z_{PA}$, hence the attenuator also reduces the effect of the signals injected by the RF-waveform characterizer on the RF-input.

3.2.3 Noise

A waveform characterizer for RF-PAs measures signals with a significantly higher power level than a receiver, hence the added noise by the waveform characterizer has less impact on the signal to noise ratio (SNR) compared to the situation in a receiver. However, the SNR at the input of the RF-waveform characterizer is still an important metric as it will determine the accuracy with which the RF-waveform characterizer can characterize the RF-waveforms, thus it directly influences the accuracy of e.g. an adaptive DPD system.

Figure 3.9 shows the dominant noise sources in the system, which are the thermal noise sources from the resistive divider and the noise generated by the RF-waveform characterizer. To evaluate the impact of these noise sources on the SNR of the measured signal the noise is referred to the input and the input referred noise can directly be related to the SNR if the RF-signal power is known. This section provides a brief overview of the most important sources of noise in a waveform characterizer.

First the attenuation network adds thermal noise while simultaneously attenuating the input signal, hence it degrades the SNR of measurement. The

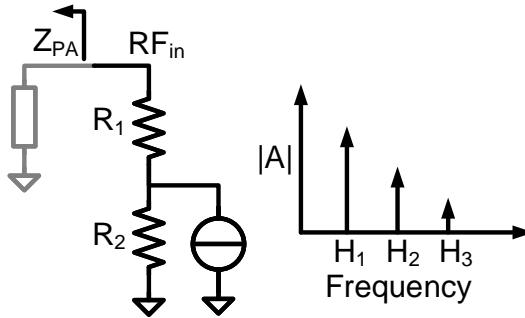


Figure 3.8: Attenuation of e.g clock leakage from RF-waveform characterizer to RF-input. Z_{PA} is the impedance looking into the RF- node.

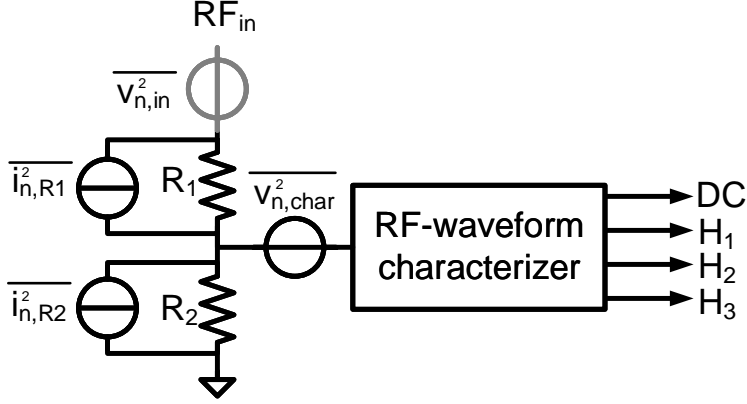


Figure 3.9: RF-waveform characterizer with the dominant noise sources. Note that $\overline{v_{n,in}^2}$ is the input referred noise of all the individual noise sources.

input referred noise of the resistive divider as shown in Fig. 3.6(a) is equal to

$$\overline{V_{n,in,att}^2} = 4k_B T R_1 \left(1 + \frac{R_1}{R_2} \right), \quad (3.11)$$

where k_B is the Boltzmann constant and T is the temperature.

The N-path mixer itself also impacts the noise. Being a passive circuit the noise factor of a single path in a N-path passive mixer is determined by its loss and is[88]

$$F = \frac{1}{D \text{sinc}^2(D)} \left(1 + \frac{R_{sw}}{R} \right), \quad (3.12)$$

where conventionally $D = \frac{1}{N}$, R_{sw} is the switch on-resistance and R the source resistance. In case of a waveform characterizer, R can be large, which reduces the effect of the switch on-resistance on the noise factor. This allows for using smaller switches and thus reduces the area and power overhead of the RF-waveform characterizer.

By combining (3.11) and (3.12) the total input referred noise for a single path in the N-path passive mixer can be calculated and is given by

$$\begin{aligned} \overline{v_{n,in}^2} &= \overline{v_{n,in,att}^2} \cdot F \\ &= \frac{4k_B T}{D \text{sinc}^2(D)} \left(R_1 \left(1 + \frac{R_1}{R_2} \right) \right) \left(1 + \frac{R_{sw}(R_1 + R_2)}{R_1 R_2} \right). \end{aligned} \quad (3.13)$$

3.3 Sample bandwidth

The RF-waveform characterizer uses the N-path filter in the mixing region, hence multiple samples are needed for an accurate estimation of the RF-waveform. To accurately characterize the RF-PA node voltages in and around the RF-PA, the bandwidth of the waveform characterizer should be higher than the bandwidth of the effect caused by a process that is currently being observed. In case of process, voltage and temperature spread these changes can be relatively slow. However, in case of a modulated signal, the RF-waveform characterizer requires a bandwidth larger than the bandwidth of the modulated signal to enable e.g. adaptive DPD during normal operation.

The bandwidth limitations in a waveform characterizer using a N-path circuit is primarily determined by the RC constant of the switch-R-C kernel and the switch on-time T_{on} . The bandwidth of the RF-waveform characterizer for $T_{on} = \frac{T_s}{N}$ can be modelled as a simple switch-R-C circuit and is given by (3.3). Fig. 3.10(a) shows the impulse response $h(t)$ of a RC-lowpass filter. Note that after a single symbol period $h(t) \neq 0$, hence previous transmitted symbols will still interfere with the current transmitted symbol. This is highlighted in Fig. 3.10(b) where a data-stream is passed through a RC low-pass filter with $RC = 0.5T_s$. Here the input data-stream is spread out over multiple symbols, hence previously transmitted symbols interfere with the currently transmitted symbol. This is called inter-symbol-interference, which degrades the quality of the waveform estimation. The spreading of the input signal over time can

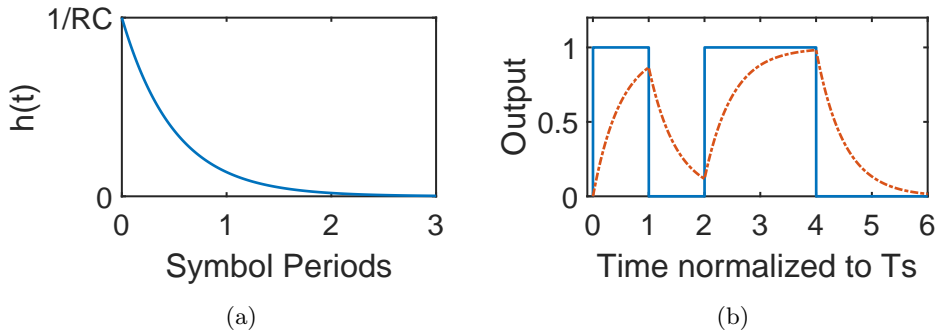


Figure 3.10: (a) RC-circuit impulse response. In this case $RC = 0.5T_s$. (b) Data stream (solid line) together with the data-stream after passing it through the RC filter (dash-dotted line).

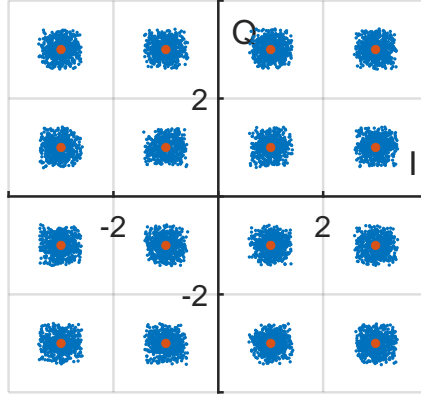


Figure 3.11: Simulated single carrier 16-QAM constellation shaped with a raised cosine filter ($\alpha = 0.25$) where the $B_{RC} = BW_{sig}$. The blue dots are the simulated constellation points and the red dots are the ideal constellation points. The simulated EVM = 10.8%.

be described by the group delay, which is given by

$$\tau_G(f) = -\frac{1}{2\pi} \frac{d(\arg(H(f)))}{df}. \quad (3.14)$$

If the group-delay is varying over frequency the delay of these frequency components will also vary, resulting in spreading the transmitted signal over more than a single symbol period. The group delay of a RC-lowpass filter is given by

$$\tau_{RC}(f) = \frac{RC}{1 + (2\pi fRC)^2}. \quad (3.15)$$

Even if the RC-lowpass filter bandwidth is equal to the signal bandwidth the RC-lowpass filter introduces a significant group delay, degrading the performance of the RF-waveform characterizer.

Figure 3.11 shows the effect of a RC-lowpass filter on a single carrier 16-QAM modulated signal shaped with a raised cosine filter ($\alpha = 0.25$). In this simulation the -3dB bandwidth of the RC-lowpass filter is equal to the bandwidth of the modulated signal. The bandwidth limitations in this example result in a simulated EVM = 10.8%. Note that this bandwidth limitation can be compensated for in the digital domain.

3.4 Timing accuracy

The timing of the LO clock affects the sampling accuracy, since the voltage over the capacitors is determined by the average value during the on-period of the clock. Fig. 3.12 shows the effect of phase noise on the edges of the LO clock. Due to the random nature of phase noise the timing of the clock edges will differ from edge to edge and thus also the period over which the input signal is averaged, resulting in noise at the output. Phase noise in the clocks will thus directly affect the accuracy of the RF-waveform characterizer. The EVM_{RMS} is given by [89]

$$\text{EVM}_{\text{RMS}} = \sqrt{\frac{1}{\text{SNR}} + 2 - 2 \exp\left(-\frac{\sigma^2}{2}\right)}, \quad (3.16)$$

where σ is the rms LO phase error, $\text{SNR} = E_s/N_0$, E_s the average symbol energy and N_0 the noise spectral density. A high rms LO phase error can thus limit the accuracy of the RF-waveform estimation. In LTE the minimum requirements for the EVM level are 3.5% for 256-QAM [3], which results in a maximum acceptable $\sigma = 2^\circ$ when assuming an infinite SNR at the input of the characterizer. An equal distribution of the 3.5% EVM over both the SNR and the rms LO phase error results in a $\text{SNR} = 32$ dB and a $\sigma = 1.4^\circ$. In case of a higher phase error the signal can be averaged to increase the measurement accuracy, but this reduces the speed at which the RF-PA can be adapted.

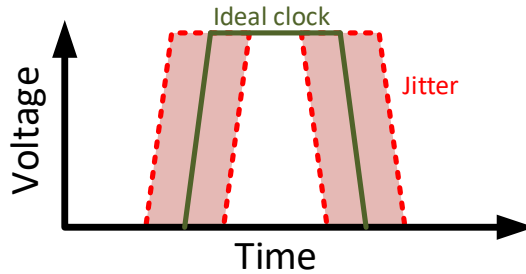


Figure 3.12: Ideal clock and clock with jitter. The ideal clock edges are in green and the possible clock edge positions for a clock with jitter are in the red shaded areas.

Compared to conventional receivers the requirements on phase noise are reduced when using a N-path circuit as waveform characterizer. In a receiver

multiple strong interferers can be present that can end up on the signal of interest due to reciprocal mixing, reducing the signal to noise ratio. In case of a waveform characterizer in an RF-PA there is only a single strong signal with its harmonics present, hence the effect of reciprocal mixing is significantly reduced.

The multi-phase clock for the waveform characterizer can be derived from the LO that is typically present in a transceiver by means of an integer-N phase locked loop (PLL). Since the requirements on phase noise are relaxed in a waveform characterizer, the PLL can be small and low power. Note that for a stand alone transmitter a reference clock needs to be provided for the integer-N PLL to operate.

Chapter 4

A Delay Spread Cancelling Waveform Characterizer for RF Power Amplifiers

Fully integrated RF-transceivers in advanced CMOS processes are common in many modern communication devices ¹. In these, especially RF-Power amplifiers (RF-PA) are affected by Process-Voltage-Temperature (PVT) spread and source and load impedance mismatch. Both effects degrade RF-PA linearity and efficiency. Different handling conditions of the device can significantly change the antenna impedance [14], resulting in reflections that may damage the RF-PA. To compensate for these effects, Adaptive Digital Pre-distortion together with multi-harmonic adaptive matching networks and tunable bias networks can be used, where Adaptive matching networks can be efficiently designed [90]. Currently, implemented compensation techniques utilize temperature sensors, DC-sensors, power detectors [91] or peak detectors [73] to control bias networks or load impedance tuners to compensate for PVT spread and load impedance mismatch. However, with these techniques information about the shape of the RF-waveform is lost.

Proper control of Adaptive Digital Pre-distortion and multi-harmonic adaptive matching networks requires data on RF-PA linearity and impedances that

¹This chapter consists of material previously published in IEEE Transactions on Circuits and Systems Part II: Express Briefs [74] and it is reformatted to a thesis form.

can be derived from the harmonics of internal RF-waveforms. Here the 1st harmonic contains information about e.g. impedance matching and output power. The 2nd harmonic can be used to tune bias networks to improve efficiency and both the 2nd and 3rd harmonics can be used to improve linearity and to increase RF-PA efficiency [92] by using Adaptive Digital Pre-distortion and multi-harmonic adaptive matching networks.

This chapter presents a 65 nm CMOS RF-waveform characterizer that characterizes the DC value and the first 3 harmonic components of an input RF-waveform. The characterizer first mixes the RF-waveform using a N-path type mixer, after which a DFT yields the harmonic content of this waveform. For this type of sampling system, delay cell mismatch limits the accuracy of the waveform estimation. Our RF-waveform characterizer introduces a novel method to cancel the effects of this delay cell mismatch.

This chapter first introduces in Section 4.1 the RF-waveform characterizer and the circuits used to sample the RF-waveform. In Section 4.2 the impact of delay errors on the performed DFT is discussed and a delay spread cancellation technique is introduced, that significantly increases the accuracy of the RF-waveform characterizer at the cost of only a modest power and area penalty. Section 4.3 gives experimental results of the impact of the delay spread cancellation technique, followed by the conclusion in Section 4.4.

4.1 Sampling Circuit

Any periodic waveform can be described by a Fourier sum of harmonic sinusoids, which are fully described by their phase, amplitude and frequency, where typically only the frequency of the first harmonic is known in transmit systems. Our RF waveform characterizer “samples” the RF-waveform period into a set of (ideally) equally spaced quasi-DC samples on which a DFT is applied to obtain the DC term and the amplitude and phase information of up to 3 harmonics. When sampling across a known impedance in series with the RF-PA output, e.g. part of a matching network, the output power of the RF PA harmonics can be derived per harmonic allowing multi-harmonic tuning.

Fig. 4.1 shows the block schematic representation of one channel (for simplicity reasons) of the RF-waveform characterizer. It consists of a Delay Line (DL) locked to the RF-signal that creates 8 non-overlapping (ideally

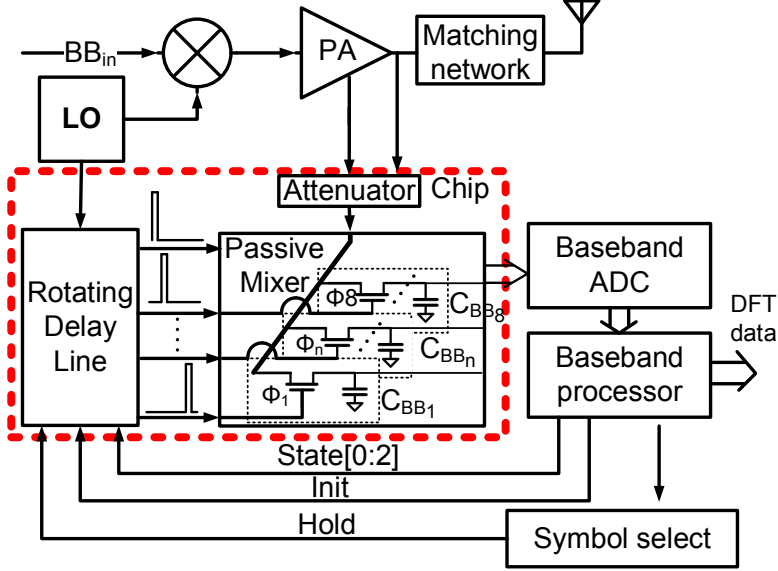


Figure 4.1: Overview of the designed system; one out of two channels is shown for simplicity. The integrated part is depicted in the dotted box.

uniformly spaced) pulses over one period of the RF signal that drive the 8-phase passive mixer. The mixer downconverts the RF-waveform to quasi-DC voltages on capacitors C_{BBn} , after which the voltages at C_{BBn} are converted to the digital domain by a baseband ADC. Switching of the mixer upconverts the switch-C RC frequency domain behaviour to harmonics of the clock signal, resulting in only harmonics of the RF-signal being downconverted to baseband. The mixer bandwidth is given by $BW = D \cdot f_{rc}$ [81], where D is the duty-cycle of the mixer pulse and f_{rc} the RC bandwidth of the switch-C network. In our case $D = 1/8$ and $f_{rc} = 1/(2\pi \cdot 5 \text{ k}\Omega \cdot 10 \text{ pF}) \approx 3.2 \text{ MHz}$ resulting in $BW \approx 400 \text{ kHz}$, which is fast enough to characterize the effects of PVT spread. After sampling, the baseband processor applies an 8-point DFT to obtain the DC value and the first 3 harmonics of the RF input signal. A front-end 10x attenuator ($9 \text{ k}\Omega + 1 \text{ k}\Omega$ in series) is used since the breakdown voltage of the used technology is 1.2 V, while voltages in the RF PA can be significantly higher [93]. This attenuation prevents breakdown of the passive mixers and also limits the feedthrough of the passive mixer clock to the RF-input signal below -80 dBm.

Fig. 4.2 shows a more detailed schematic overview of one channel of the

4. A DELAY SPREAD CANCELLING WAVEFORM CHARACTERIZER FOR RF POWER AMPLIFIERS

implemented circuit. It consists of a rotating delay line (see Section III), a pulse shaper and a switching matrix that ensures that the mixers sample the RF-signals on the correct baseband capacitors C_{BBn} . The pulse shaper converts the 50% duty cycle square wave to $\leq 12.5\%$ duty cycle pulse required to drive the 8-phase passive mixer, enabling the down-conversion of both even and odd harmonics. The large RC time constant in the mixer results in sinc-filtering of the downconverted RF-signal [81], which can easily be compensated for in the digital domain. Also, the passive mixer behaves like an N-path filter; hence the input impedance of the sampling system equals $18.85 \times R_{switch}$ of the mixer [87]. In our case the input impedance of the sampling system is about 100 k Ω , therefore negligibly loading the attenuator.

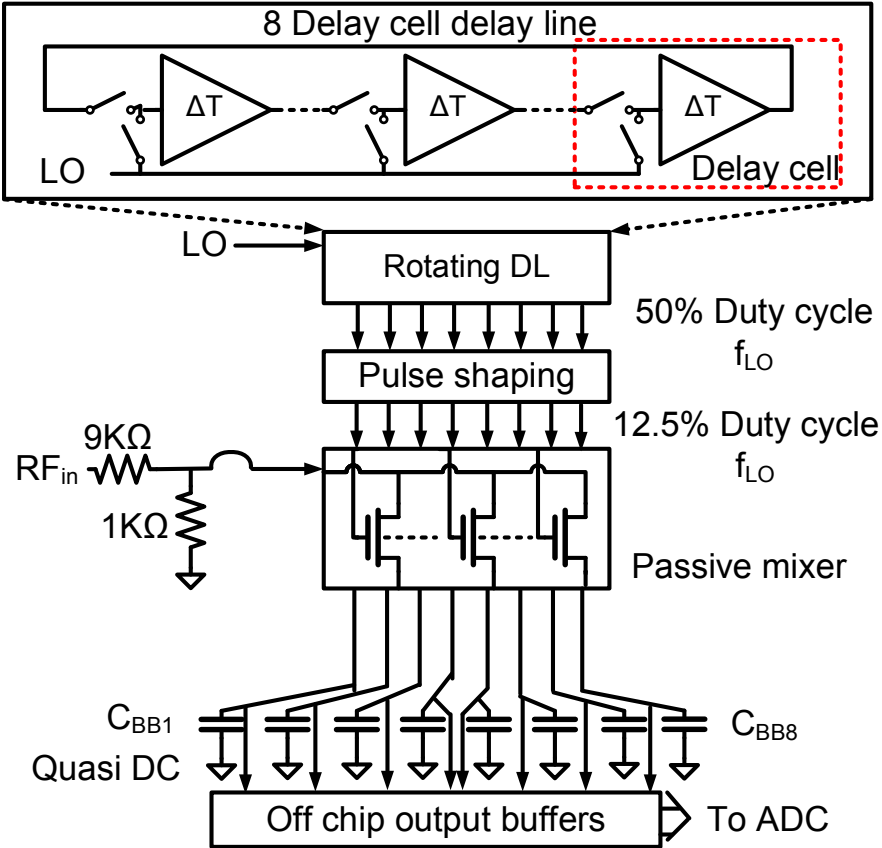


Figure 4.2: Overview of the designed rotating delay line system.

4.2 Delay Spread Cancellation

A DFT assumes uniformly distributed sample points over a beat period, which in our demonstrator is the period of the first harmonic of the RF signal. However, delay cell mismatch causes static random mismatch between the sample points, resulting in delay errors Δt_{ϵ_N} (Fig. 4.3). In a locked delay line, the variance of the delay over the delay line [94] (Fig. 4.3) is given by:

$$\sigma_{\Delta_{tn}} = T_{Ref}^2 \frac{n(N-n)}{N^3} \sigma_{\epsilon n}^2 \quad (4.1)$$

where $\sigma_{\Delta_{tn}}$ is the systematic mismatch after n cells, $\sigma_{\epsilon n}$ is the individual delay cell mismatch, N is the number of delay cells and n being the n -th output tap of the delay line. Both distribution are assumed to be normally distributed with a zero mean. The static random mismatch causes leakage between DFT bins in the DFT due to the ideal sampling moments becoming non-ideal, thereby reducing the dynamic range of the waveform estimation. Impedance level scaling (wider components in the delay cell and a proportional increase in power consumption) can alleviate mismatch-limited accuracy at the cost of area and power dissipation.

We implemented a power and area efficient method to ideally cancel the effect of delay spread in individual delay cells. This method is based on the statistical properties of mismatch having a zero mean (equation (4.2)), and properties of the variance in a Delay Locked Loop (DLL) as shown in equation (4.1).

$$\sum_{n=1}^N \Delta t_{\epsilon n} = 0 \quad (4.2)$$

Cancellation of the impact of delay variations is implemented by rotating the N individual delay cells in the delay line in N steps, as shown in the top part of Fig. 4.4. Delay cell rotation is implemented by switches in front of all delay cells (see Fig. 4.2), that either connect the delay cell input to the previous delay cell or to the LO. For each of the N rotation states the waveform is measured and after one full rotation there are $N \times N$ per-rotation-state measurements (as depicted in the bottom part of Fig. 4.4) and all delay cells have occupied every position exactly once. Then the average timing error at each position equals the average error of every delay cell, which is zero

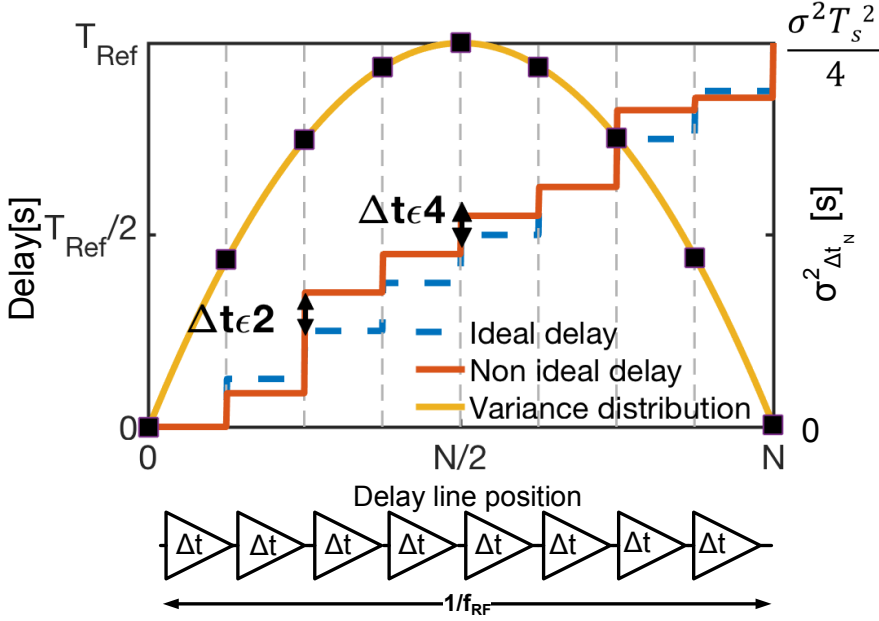


Figure 4.3: Variance of the delay and delay distribution over the delay line for a standard DLL. N is the length of the delay line. Note that the variance of the delay over the line is zero at the begin and end of the line. This results in the average delay error being zero over the entire delay line when locked.

in a locked delay line. Consequently, digitally averaging the N per-rotation waveform measurements yields full cancellation of the delay cell spread at all sample time instances thereby vastly improving the accuracy of the waveform estimation without an area and power penalty. We call this technique Delay Spread Cancellation (DSC). Note that this is in contrast to Dynamic Element Matching, where due to mismatch shaping or mismatch scrambling, errors are effectively converted into noise [95].

DSC significantly improves the average sampling timing accuracy of the system, however after averaging of the voltage waveforms a residual error voltage waveform is still present. To illustrate the effect of DSC on this residual voltage error waveform we calculate the expected error signal power. First we calculate the Taylor expansion of a sine wave at a sample moment T_0 when

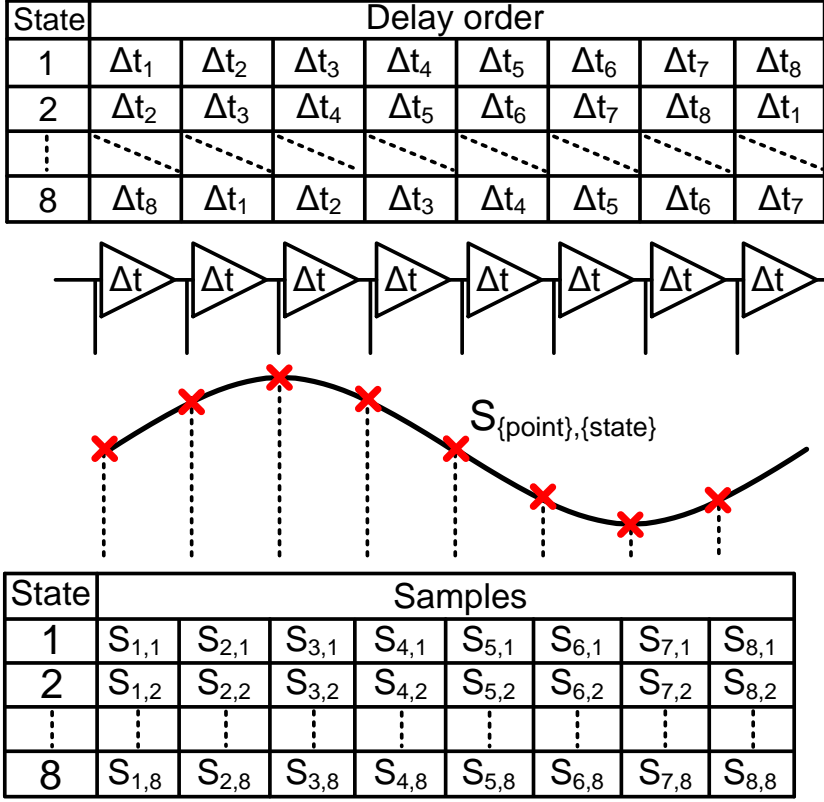


Figure 4.4: Rotation order of the delay elements. Every delay element is used in every place in the delay line exactly once. During every rotation state the waveform is sampled, resulting in a $N \times N$ matrix, where N is the number of samples per period. In this work $N=8$. After one full rotation cycle is complete the results are averaged.

we apply DSC:

$$\begin{aligned}
 f(t) &= \frac{1}{N} \sum_{n=0}^N \sum_{m=0}^{\infty} \frac{f^{(m)}(T_0)}{m!} (t - T_0)^m \\
 &= \frac{1}{N} \sum_{n=0}^N \left[f(T_0) + \frac{\partial f(T_0)}{\partial t} (t - T_0) + \right. \\
 &\quad \left. \frac{1}{2} \frac{\partial^2 f(T_0)}{\partial t^2} (t - T_0)^2 + \frac{1}{6} \frac{\partial^3 f(T_0)}{\partial t^3} (t - T_0)^3 + \dots \right]
 \end{aligned} \tag{4.3}$$

where m denotes the m -th harmonic of the sampled signal. Now we use equation 4.3 to calculate the effect of the delay cell mismatch Δt_{en} . Note that the

zero order term

$$\frac{1}{N} \sum_{n=0}^N f(T_0) = f(T_0) \quad (4.4)$$

is the ideal sample point. The effect of DSC is emphasized when we combine equation (4.2) and the first order term in equation (4.3) resulting in:

$$\frac{1}{N} \sum_{n=0}^N \frac{\partial f(T_0)}{\partial t} (\Delta t_{en} - T_0) = 0 \quad (4.5)$$

showing the cancellation of the error in first order. The dominant error is now given by the second order term in the Taylor expansion. Calculating the expected value for the error at sample moment T_0 we combine the second order term in equation (4.3) and equation (4.1) resulting in:

$$E \left[\frac{1}{2} \frac{\partial^2 f(T_0)}{\partial^2 t} \underbrace{\frac{1}{N} \sum_{n=0}^N (\Delta t_{en} - T_0)^2}_{\sigma_n^2} \right] = \frac{1}{2} \frac{\partial^2 f(T_0)}{\partial^2 t} T_{Ref}^2 \frac{n(N-n)}{N^3} \sigma_{en}^2 \quad (4.6)$$

Fig. 4.5 shows the simulation results of the effect of delay cell mismatch on the leakage of an ideal sinusoid to other bins in the DFT; here $H_1(\circ)$, $H_2(-)$ and $H_3(+)$ represent the 1st, 2nd respectively the 3rd harmonic of the input signal. The dotted lines are w/o DSC, the solid lines are with DSC. A locked delay line was simulated with delay cells that have mismatch. The mismatch is modelled as a normally distributed gain error in the ideal delay of the delay cells as shown in equation (4.7), where Δt_n is the delay of the n^{th} delay cell, T_{ref} the reference period and σ_{en} the delay cell mismatch corresponding to the n^{th} delay cell.

$$\Delta t_n = \frac{T_{ref}}{N} (1 + \sigma_{en}) \quad (4.7)$$

After adding mismatch the delay of all the cells is normalized so that the sum of all delays is equal to T_{ref} , after which the system is locked to the reference period. The sample instances of the locked delay line are now used to ideally sample a sinusoidal wave on which a DFT is performed. Fig. 4.5 shows the results of this simulation for both the conventional case and the case where delay spread cancellation is applied. From Fig. 4.5 it can be concluded that the system with delay spread cancellation behaves like a second order system

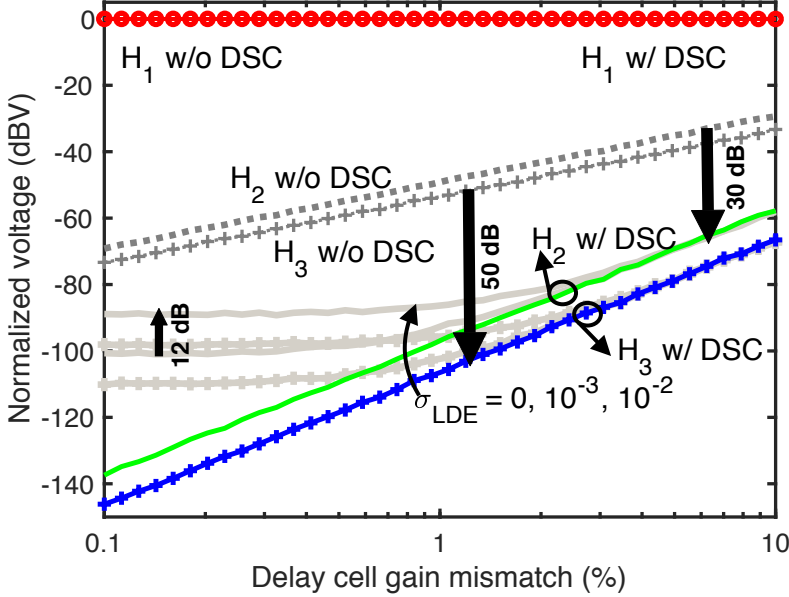


Figure 4.5: Simulated effect of delay cell mismatch on leakage of H_1 into H_2 and H_3 in the DFT, assuming a sinusoidal input signal. The dotted lines are the results without DSC, where the solid lines without markers are the results after Delay Spread Cancellation (DSC) for H_2 for 3 different values of the layout dependent (relative) error to T_{Ref} , σ_{LDE} . The results for H_3 with DSC are the solid lines with + as marker.

with a 40 dB/decade slope, complying with equation (4.6). For a typical delay cell mismatch in our 65 nm CMOS process of $\sigma_{\Delta tn} = 4.5\%$ a gain in dynamic range of 35 dB is observed.

Layout dependent matching and load matching errors impact the performance of the waveform characterizer, limiting the maximum dynamic range of the waveform characterizer. There are two types of layout dependent effects: in-loop and out of loop. Doubling the layout dependent effects in-loop (σ_{LDE}) decreases the DR by 12 dB, due to the system being second order after rotation. Note that for the same reason, doubling the frequency for some matching level also decreases the DR by 12 dB (see Fig. 5, light grey solid lines. H_2 has no markers, H_3 is marked with a +). σ_{LDE} is the standard deviation of the layout dependent time error relative to T_{Ref} . The out of loop error presents itself as deterministic sampling jitter comparable to that in ADCs.

4.3 Measurement Results

4.3.1 System measurements

A demonstrator chip with a maximum input signal frequency of $f_0 = 1.1$ GHz and two channel input is designed to prove the principle of using the rotating delay line for the RF-waveform characterizer. The operating frequency is limited by the switches in front of the delay cell, the output buffer of the delay cell and the loading of the delay cell by the pulse shapers. Fig. 4.6 shows the photograph of the designed demonstrator chip. The two channel characterizer occupies a total active area of 0.11mm^2 of which 0.05mm^2 is occupied by the 16 capacitors. The overhead to implement the delay cell rotation is only $800\text{ }\mu\text{m}^2$. The measurement setup consists of two signal generators (Agilent E8267D) to create the clock and RF-waveform signal, 8 SMUs (2x HP4156Bs') to digitize the capacitor voltages and a computer running MATLAB to only perform the averaging, an 8 point DFT, sync compensation and rotation. The SMUs could be replaced by a 10-bit ADC (to cover the full dynamic range of the RF-waveform characterizer). At the maximum RF signal input frequency of f_0 the power consumption equals 18.6 mW under continuous operation.

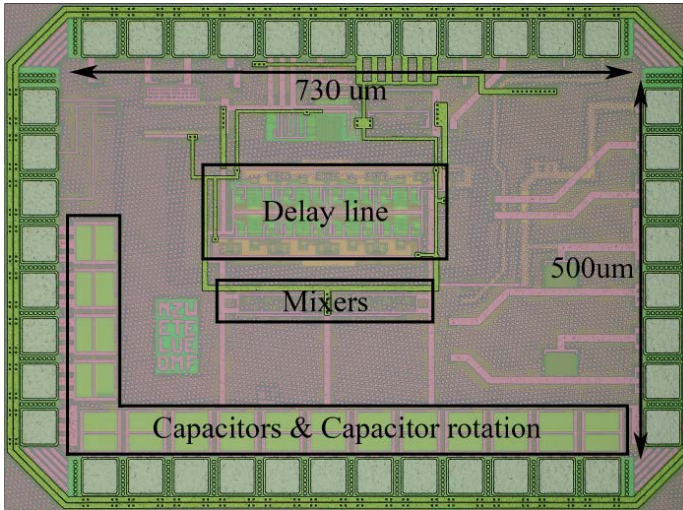


Figure 4.6: Chip photo of the two channel waveform characterizer.

To demonstrate the performance of the RF-waveform characterizer, the harmonic spectrum of two power-combined signal generators is measured. This

measurement mimics a PA during normal operation, where the measurements are performed before the matching network on internal signals of an integrated RF-PA. These internal signals before the matching network can contain significant harmonic content at the 2^{nd} and 3^{rd} harmonic. The output power of the first harmonic should remain constant during normal operation and the spurious emissions are measured and are to be reduced. The output of the first generator is a +10 dBm sine wave at frequency f_0 . The power of the second sine wave generator is swept from -10 to 20 dBm at a frequency of $2 \cdot f_0$ (Fig. 4.7) or $3 \cdot f_0$ (Fig. 4.8) mimicking non-linearities in the RF-PA. The harmonics of the generators used for signal generation are well below the harmonics caused by non-linear effects in the RF-waveform characterizer. Fig. 4.7 and Fig. 4.8 show the three estimated harmonics of our system, as function of the 2^{nd} and 3^{rd} harmonic input power. In both graphs, the measured data per state is shown in grey, while the result after delay spread cancellation is shown in black. The highest improvement in accuracy is observed for low input powers as shown in Fig. 4.7, where the SNR of the 3^{rd} harmonic is improved by 20 dB by the introduced delay spread cancellation compared to using a conventional static delay line. The slope of the 3^{rd} harmonic in Fig. 4.7 is non-zero due to non-linear effects in the integrated mixer, where mixing of the 1^{st} harmonic with the internal LO causes the static power level of the 2^{nd} harmonic in Fig. 4.8. The linearity of the RF-waveform characterizer is determined from the input power to output power slope. This slope is fitted with a polynomial function, where an ideal linear system only has a first order term. The second order term of the normalized polynomial function is the dominant non-linearity in the system and thus limits the overall linearity of the system. The second order terms of the two polynomial functions equals 0.0073 and 0.0094 for respectively the 2^{nd} and 3^{rd} harmonic power sweeps, resulting in a 7.1 and 6.7 bit linearity. In a similar way the linearity for the first harmonic is derived to be 6.8 bit. The SFDR is derived from Fig. 4.8, where the difference in power between the 1^{st} harmonic and the 2^{nd} harmonic is 24 dB. Extensive Spectre simulations show that clock feedthrough is the dominant limiting contribution for SFDR in our demonstrator chip.

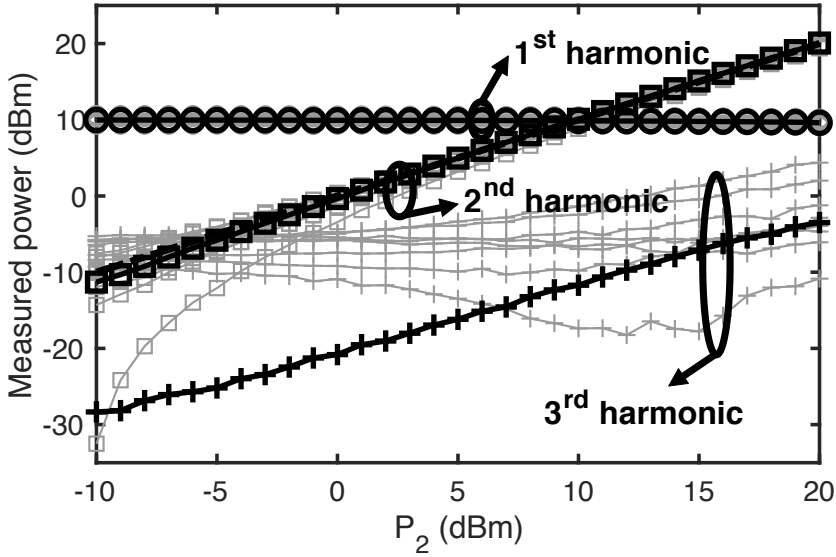


Figure 4.7: Harmonic power spectrum for different values of P_{in2} at $2 \cdot f_0$. $P_{in1} = 10$ dBm at f_0 , $P_{in3} = -\infty$ dBm at $3 \cdot f_0$. Ideal values are in dashed black lines, average over rotation states in solid black lines and per-rotation state values are in grey.

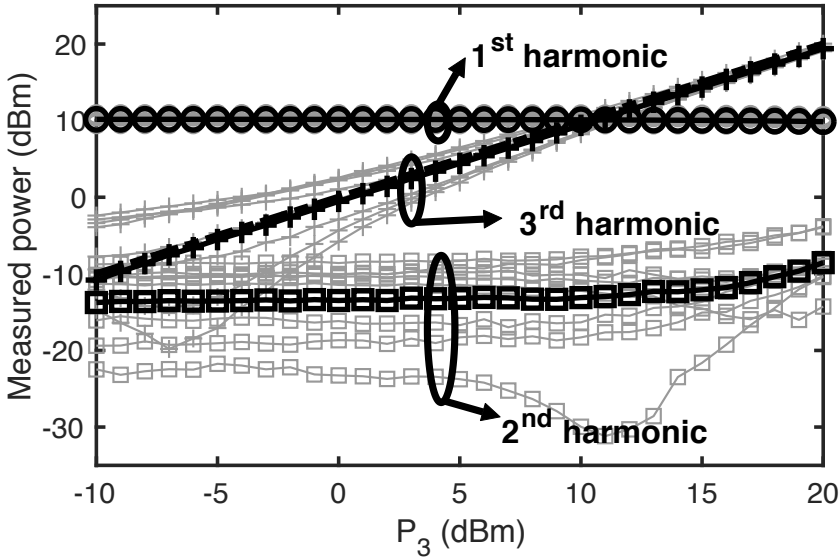


Figure 4.8: Harmonic power spectrum for different values of P_{in3} at $3 \cdot f_0$. $P_{in1} = 10$ dBm at f_0 , $P_{in2} = -\infty$ dBm at $2 \cdot f_0$. Ideal values are in dashed black lines, average over rotation states in solid black lines and per-rotation state values are in grey.

4.3.2 Measurements on a misbiased RF-PA

As next demonstration, the output of a Mini-Circuits ZX60-1215LN-S+ amplifier was measured. The amplifier is intentionally biased in such a way that it works far in compression. The input power of the 1st harmonic to the Mini-Circuits amplifier is swept from 0 to 10 dBm at an operating frequency $f_0 = 1.1$ GHz. The higher harmonics created by the generator are well below the harmonics generated by the Mini-Circuits amplifier under these conditions, therefor are not affecting the measurements. The output of the amplifier is measured both with the designed waveform characterizer system and using a spectrum analyzer (Agilent E4404B) for comparison. From Fig. 4.9 it can be concluded that the output power of the RF PA can be determined within 0.2 dB, 0.9 dB and 4 dB accuracy for respectively the 1st, 2nd and 3rd harmonic with delay spread cancellation compared to 0.3 dB, 3 dB and 14.7 dB for the static delay line. The 1st and 2nd harmonics results of our RF-waveform characterizer after applying DSC are comparable to the results measured by the spectrum analyser. Especially for the 3rd harmonic the accuracy of the measurement results is significantly increased by rotating the delay line and averaging the measurement results to achieve delay spread cancellation.

Comparing to [91], our work measures the phase and magnitude of the DC and first 3 harmonics of an RF-waveform instead of only derived parameters such as output power, DC current sensors and temperature sensors. This measured information about the RF-waveform shape allows ADPD. The total power consumption of the sensors in [91] is 18.4 mW, where our demonstrator consumes 18.6 mW.

4.4 Conclusion

We present a 0.11mm^2 two-channel RF waveform characterizer to measure two RF-channels at about 6.8-bit accuracy, capturing e.g. the output and/or the internal signal of an RF-PA, thereby allowing ADPD and adaptive matching networks. We introduce delay spread cancellation as a power efficient module to significantly increase accuracy. By rotating the N delay elements inside the delay line exactly N times delay spread is fully cancelled, yielding on average ideal sample time instants. Applying DSC in a signal waveform sampler,

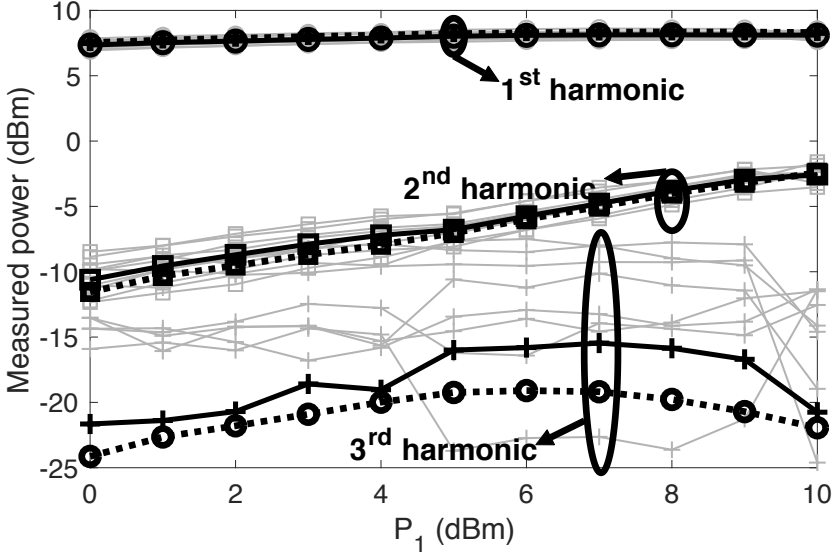


Figure 4.9: Harmonic spectrum Mini-Circuits PA for different RF-PA input powers measured after the matching network with the designed system. Spectrum analyser values are in dashed black lines, average over rotation states in solid black lines and per-rotation state values are in grey.

the SNR of the measurement system increases by up to 20 dB without any significant increase in area ($800\mu m^2$) and power consumption (1 mW). In our implementation, clock feedthrough limits its measurement accuracy. The system can easily be integrated with an RF-PA due to its relatively small size. The 6.8-bit linearity of the measurement system is maintained from -10 dBm to 20 dBm of RF input power at 1.1 GHz while consuming 18.6 mW (delay line, mixer and capacitor rotation for two channels) under continuous operation for our proof-of-principle demonstrator.

Chapter 5

Reconstructing Aliased Frequency Spectra by Using Multiple Sample Rates

5.1 Introduction And Prior Art

With the advancements in technology the energy consumption for digital signal processing (DSP) has seen a tremendous decrease ¹. Before physical (analog) signals can be processed by DSPs they have to be converted to the digital domain by an analog-to-digital converter (ADC). This digitization process involves the conversion of a continuous-time continuous-amplitude analog signal to a discrete-time discrete-amplitude digital signal. The conversion from continuous-time to discrete-time may give rise to aliasing. Aliasing might cause different signal frequencies to become indistinguishable of each other, thus resulting in frequency ambiguity. Anti-aliasing filters circumvent aliasing by filtering frequencies outside the desired Nyquist zone (usually the first Nyquist zone is desired). However if these other (mostly higher) frequencies contain useful information, this information also gets removed.

The work in [96] solves frequency ambiguity due to aliasing by sub-sampling a sine wave with a time difference between two sampling clocks of the same

¹This chapter consists of material currently in the final review stage for publication in IEEE Transactions on Circuits and Systems Part I: Regular Papers and it is reformatted to a thesis form.

frequency, resulting in a frequency-dependent phase shift. However, this solves the frequency ambiguity for a single tone only. The work in [97] proposes an approach that requires $(N+1)$ co-prime time-delays and $(N+1)$ ADCs for estimating N frequency components. But even in narrow band systems N is typically large, making this approach impractical.

Another method to estimate frequency content outside the desired Nyquist band is sub-sampling the input signal with different co-prime sample rates [98] and then calculating multiple DFTs corresponding to these sample rates. The frequency corresponding to each DFT bin can be related to the (corresponding) co-prime sample rates through a modulo operation and a residue. Using the Chinese remainder theorem [98] on this set of residues allows the determination of the unknown input frequencies. However, this method requires at least as many co-prime samplers as the number of frequencies to be estimated, which significantly increases system complexity.

The work in [99] demonstrates spectral estimation and identification of sinusoidal signals using co-prime samplers. In contrast to [98] the signal is sampled at sub-Nyquist rate by only two co-prime samplers to obtain two sparsely sampled data sets of the input signal. Spectral identification of the input signal is then performed by estimating the (time) average auto-correlation over multiple “snapshots” (time domain blocks) of the two sparsely sampled data sets. The accuracy of the spectral estimation (and auto-correlation) depends on the length of the time interval over which the averaging takes place. This results in a large latency in the overall signal estimation as highlighted in [99], thereby making it impractical to be used for real-time reconstruction of signals.

This chapter proposes a deterministic algorithm to remove frequency ambiguity due to aliasing by sampling the signal at only two distinct non-integer multiples of each other sample rates. This allows the algorithm to unalias signals that may be spread over multiple Nyquist zones while simultaneously keeping the aggregated bandwidth close to the Nyquist-Shannon sampling limit. The proposed algorithm requires signals that have an orthogonal frequency basis. This allows the signal to be sampled without any spectral leakage, which ensures that every spectral contribution occupies a single distinct frequency after sampling. The proposed algorithm could find applications in areas such as RF waveform characterization [74] (Appendix C) and built-

in self-test of transceiver signal chains to improve digital pre-distortion and reliability, IQ reconstruction and other application scenarios as long as the frequencies of interest are known and the signal is orthogonal.

The structure of the chapter is as follows. Section II revisits the constraints on the sample rate for baseband and band-limited signals and shows the effect of frequency ambiguity due to aliasing. Section III introduces the proposed deterministic algorithm for resolving multiple simultaneous band-limited signals. Section IV compares the proposed algorithm with other techniques. Section V discusses the limitations of this algorithm under non-ideal conditions. Section VI shows experimental verification of the algorithm, along with a qualitative comparison with conventional sampling techniques. Although all examples and test signals used in this chapter are orthogonal frequency-division multiplexing (OFDM) signals, the proposed algorithm can be used to detect and reconstruct signals with any orthogonal frequency basis as shown in section III. Section VII summarizes the findings in this chapter.

5.2 Frequency ambiguity due to aliasing

Frequency ambiguity arises when two aliases or the baseband signal and an alias fold on top of each other. When sampling a signal aliasing can occur, which can result in signals folding on top of each other making them indistinguishable, hence resulting in frequency ambiguity. This work assumes that $x(t)$ contains uniformly spaced orthogonal discrete-frequency sub-carriers with frequency spacing f_o . Most modern communication systems use signals with some form of orthogonal frequency basis for modulation such as OFDM and orthogonal on-off keying (OOK). This work aims at more efficiently approaching the Nyquist-Shannon limit for input signals with an orthogonal frequency basis that are spread over multiple frequency bands (e.g. multi-band OFDM). To retain orthogonality of the sub-carriers in each symbol, both the symbol period must be a multiple of $\frac{1}{f_o}$ and the complex value of the sub-carriers must remain constant within a symbol period [28].

$x(t)$ can be described as a set of L orthogonal sub-carriers, which may be non-contiguous in the frequency domain. Since $x(t)$ is a band-limited signal

it can also be represented by

$$x(t) = \sum_{l=1}^L \left(A_l e^{j2\pi S_l f_o t} + A_l^* e^{-j2\pi S_l f_o t} \right) \quad (5.1)$$

where $0 \leq t < \frac{1}{f_o}$, S is the set of L down-converted modulated sub-carriers, $S_l \in \mathbb{N}$ is the l^{th} element in S , A is a set containing the complex values (magnitude and phase) of the sub-carriers in S , A_l is the l^{th} element in A , $|S|$ and $|A|$ are the ranks of S and A respectively and $L = |S| = |A|$. Please note that in (5.1) A_l can be a complex number. Different orthogonal signals (such as OOOK or MFSK) differ in the M-ary encoding scheme, which corresponds to a different complex value A_l in (1) e.g. $A_l = \{0, 1\}$ in OOOK. The proposed algorithm does not depend on the chosen modulation scheme, as long as the modulation scheme has an orthogonal frequency basis.

The straightforward way to convert an analog signal to a time-discrete signal without any aliasing is to sample the signal at a frequency higher than twice the highest frequency component in the signal, such that

$$f_s \geq 2f_o \cdot \max(S). \quad (5.2)$$

However this is inefficient as the frequency content between the N band-limited signals lacks any information, yet is processed.

According to the Nyquist-Shannon theorem [100], an analog signal can be reconstructed without loss of information if f_s is higher than twice the bandwidth of the signal. The minimum sampling rate $f_{s,\min}$ for $x(t)$ is therefore:

$$f_{s,\min} > 2|S|f_o. \quad (5.3)$$

If f_s is chosen to satisfy the Nyquist-Shannon limit as defined in (5.3), then aliasing can occur [101, 102], since $2|S|f_o \leq f_s \leq 2f_o \cdot \max(S)$.

Sampling $x(t)$ uniformly at a rate f_s results in:

$$y(t) = x(t) \cdot p(t), \quad (5.4)$$

where $p(t)$ is a series of Dirac delta pulses:

$$p(t) = \sum_{r=-\infty}^{\infty} \delta\left(t - \frac{r}{f_s}\right)$$

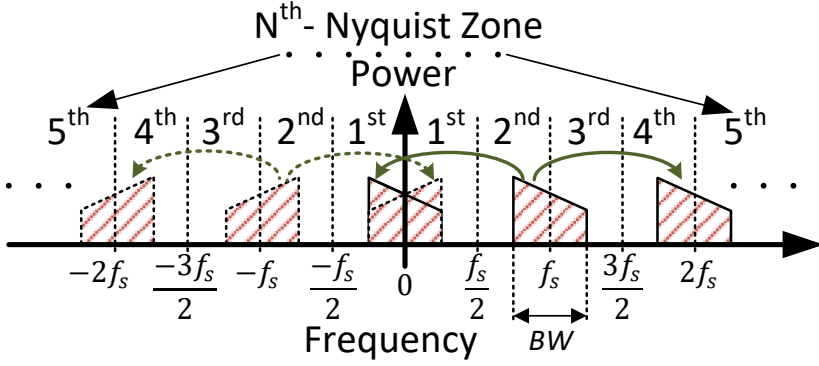


Figure 5.1: Aliasing of a band-limited signal centred around f_s to the baseband for the case e.g. $r = \{-1, 1\}$ in (5.5).

where $r \in \mathbb{Z}$. The Fourier transform of $y(t)$ can be written as:

$$Y(f) = f_s \sum_{r=-\infty}^{\infty} X(f - rf_s) \quad (5.5)$$

where $X(f)$ is the Fourier transform of $x(t)$.

The work in [101] and [103] showed that there are upper and lower bounds on f_s when directly sampling multiple band-limited signals that are spread over multiple Nyquist zones. If these boundary conditions for f_s are not satisfied, then some frequency components alias on top of each other making them indistinguishable, resulting in frequency ambiguity as illustrated in Fig. 5.1.

IQ reconstruction can remove a specific frequency ambiguity due to aliasing [101], as shown in Fig. 5.2. However, frequency components in higher Nyquist zones (frequency band from $\frac{(N-1)f_s}{2}$ to $\frac{Nf_s}{2}$ where $N > 1$, see Fig. 5.2), all fold into the first Nyquist zone. As shown in Fig. 5.2(e) these signals (from multiple Nyquist zones) become indistinguishable and cannot be recovered with IQ reconstruction. We present an algorithm that allows more flexibility in allocation of component carriers which can be spread over multiple Nyquist zones.

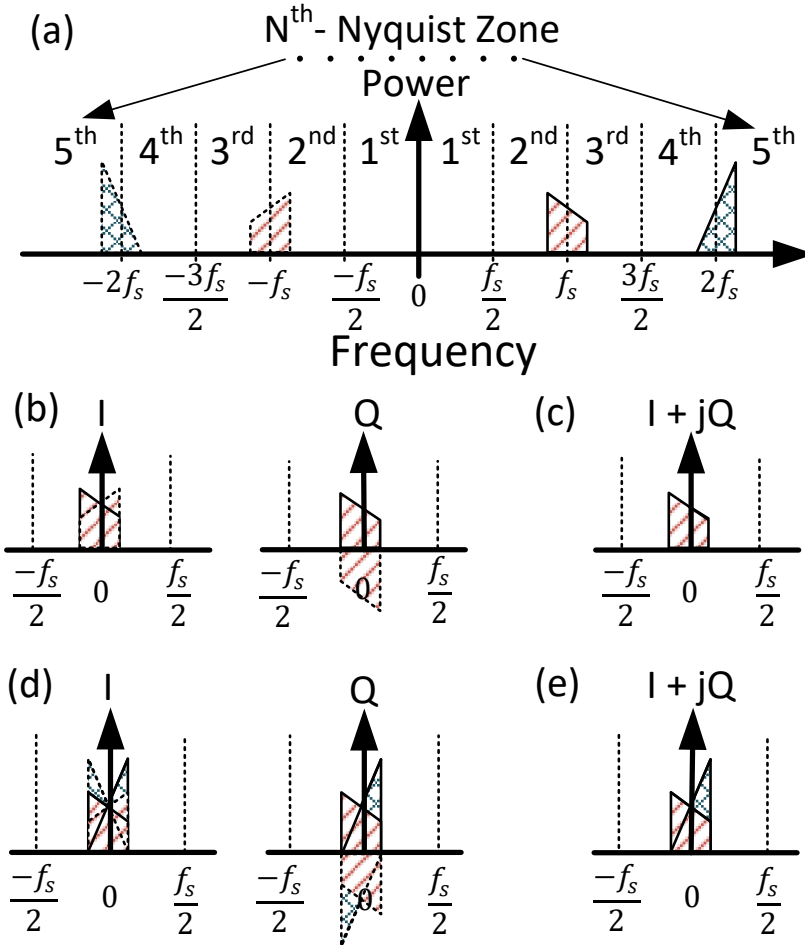


Figure 5.2: (a) Two bandpass signals in different Nyquist zones where the frequency components of the band-limited signals are on either side of the sampling frequency f_s . (b) I and Q power spectra after sampling when only the signal in (a) centred around f_s is present. (c) $I + jQ$ spectrum from (b) where the original input spectra can be recovered (d) I and Q power spectra after sampling when both signals in (a) are present (e) $I + jQ$ spectrum from (d) where the original input spectra cannot be distinguished from each other.

5.3 Multi-rate Unaliasing

This section presents a mathematical description of an algorithm that can resolve frequency ambiguity due to aliasing, by using multiple sample rates that are non-integer multiples of one another. We denote this algorithm as the multi-rate unaliasing (MRU) algorithm.

5.3.1 MRU Algorithm

In this section we present an algorithm that utilizes two samplers with distinct sampling frequencies to enable demodulation of orthogonal signals from several Nyquist zones. Simultaneously it allows an aggregated sample rate close to the aggregated bandwidth of $2f_o|S|$. Sampling the signal at different sample rates creates unique aliasing patterns for the same input signal spectrum as described by (5.5). A system of independent linear equations can be formulated that describes these aliasing patterns, allowing for reconstruction of the input spectrum. The limitations of the MRU algorithm on the maximum aggregated bandwidth and maximum input signal frequency are discussed.

The discrete-time sequence $d[n]$ at the output of the sampler contains the weight of the impulse train in the uniformly sampled signal $y(t)$ in equation (5.4) for sampling intervals T_s :

$$d[n] = y(nT_s) \quad (5.6)$$

where $T_s = \frac{1}{f_s}$ and n is the sample index. When sampled at $f_s = Mf_o$ the duration of a symbol period equal to $\frac{1}{f_o}$, $d[n]$ has length M , which will be used as the DFT length. We assume that these M -samples belong to a single symbol to retain orthogonality between symbols. This ensures that the spectral content of each sampled symbol is mapped uniquely to a single DFT bin, allowing reconstruction by the MRU algorithm. The M -point DFT of $d[n]$ is:

$$D[k] = \frac{1}{M} \sum_{n=0}^{M-1} d[n] e^{-j2\pi \frac{n}{M} k} \quad 0 \leq k \leq M-1. \quad (5.7)$$

By combining (5.6), (5.7) and using

$$\frac{1}{M} \sum_{n=0}^{M-1} e^{\pm j2\pi S_l \frac{n}{M}} e^{-j2\pi k \frac{n}{M}} = \begin{cases} 1 & \text{when } k = \pm S_l \mp rM \\ 0 & \text{otherwise.} \end{cases} \quad (5.8)$$

$D[k]$ can be written as

$$D[k] = \sum_{l=1}^L \left(\sum_{r=-\infty}^{\infty} \left(A_l \delta(S_l - k - rM) + A_l^* \delta(S_l + k - rM) \right) \right). \quad (5.9)$$

$D[k]$ is the discrete-frequency representation of the input signal $x(t)$ and its aliases after sampling at a rate $f_s = Mf_o$. We now reformulate (5.9) in vector form as:

$$D[k] = \mathbf{P}[k] \mathbf{A} \quad (5.10)$$

where \mathbf{A} is a $2L \times 1$ column-vector containing both A_l and A_l^* and where $\mathbf{P}[k]$ is a $1 \times 2L$ row-vector describing the contributions of \mathbf{A} to the value of $D[k]$, and contains information about the aliasing pattern. $\mathbf{P}[k]$ is ordered in such a way that the even and odd elements respectively describe the contributions of \mathbf{A} and \mathbf{A}^* . This representation is chosen for convenience and does not further affect the algorithm. Thus:

$$P[k, 2l] = \sum_{r=-\infty}^{\infty} \delta(S_l - k - rM), \quad (5.11)$$

$$P[k, 2l + 1] = \sum_{r=-\infty}^{\infty} \delta(S_l + k - rM) \quad (5.12)$$

where $0 \leq k \leq M - 1$ and $P[k, l] \in \{0, 1\}$.

Combining the M linear equations for $D[k]$ into one matrix yields

$$\mathbf{D} = \mathbf{P} \mathbf{A} \quad (5.13)$$

where \mathbf{P} is an $M \times 2L$ matrix. The aliasing pattern of \mathbf{A} to \mathbf{D} depends on the signal frequencies relative to the sampling frequency. Changing the sampling frequency changes the aliasing pattern, resulting in a different \mathbf{P} .

Fig. 5.3 shows the conceptual diagram of the MRU algorithm. The switches S_1 and S_2 are samplers that are clocked respectively at two different (non-integer multiple) sample rates $M_1 f_o$ and $M_2 f_o$. To demonstrate the effectiveness of MRU, the input signal $x(t)$ is directly generated from a signal source and is sampled by both S1 and S2. In a practical system $x(t)$ would be

the signal after frequency translation. This results in two complex DFTs $\mathbf{D}_{\mathbf{M}_1}$ and $\mathbf{D}_{\mathbf{M}_2}$ after performing the DFT on $d_{M_1}[n]$ and $d_{M_2}[n]$. $\mathbf{D}_{\mathbf{M}_1}$ and $\mathbf{D}_{\mathbf{M}_2}$ are column vectors with sizes $M_1 \times 1$ and $M_2 \times 1$ respectively. The two DFTs are concatenated into a column vector $\mathbf{D}_{\mathbf{c}}$ of length $(M_1 + M_2) \times 1$ resulting in

$$\mathbf{D}_{\mathbf{c}} = \begin{bmatrix} \mathbf{D}_{\mathbf{M}_1} \\ \mathbf{D}_{\mathbf{M}_2} \end{bmatrix}. \quad (5.14)$$

In mathematical terms concatenation is equivalent to the collection of output DFTs from both the samplers and vertically appending the DFTs to create a new matrix.

The two distinct sets of aliasing patterns corresponding to the sample frequencies $M_1 f_o$ and $M_2 f_o$ ($\mathbf{P}_{\mathbf{M}_1}$ and $\mathbf{P}_{\mathbf{M}_2}$) are formed by using (5.11) and (5.12) and are concatenated as

$$\mathbf{P}_{\mathbf{c}} = \begin{bmatrix} \mathbf{P}_{\mathbf{M}_1} \\ \mathbf{P}_{\mathbf{M}_2} \end{bmatrix} \quad (5.15)$$

where $\mathbf{P}_{\mathbf{c}}$ has size $(M_1 + M_2) \times 2L$. The reconstructed complex value vector $\mathbf{A}_{\mathbf{R}}$ can then be described as

$$\mathbf{A}_{\mathbf{R}} = \mathbf{P}_{\mathbf{c}}^{-1} \mathbf{D}_{\mathbf{c}} \quad (5.16)$$

where $\mathbf{P}_{\mathbf{c}}^{-1}$ is the left inverse of $\mathbf{P}_{\mathbf{c}}$. $\mathbf{A}_{\mathbf{R}}$ contains the estimated complex value (magnitude and phase) information of the sub-carriers in the signal $x(t)$. Performing an IFFT on the sub-carriers corresponding to the signal of interest in $\mathbf{A}_{\mathbf{R}}$ will result in the respective time domain estimate of $x(t)$. An example demonstrating MRU is shown in Appendix A.

The maximum bandwidth that can be reconstructed depends on the number of unique samples taken by the two samplers over the sampling interval T_s . The total number of samples equals $(M_1 + M_2)$, whereas the common (coinciding) number of samples equals $\text{gcd}(M_1, M_2)$, where $\text{gcd}(\cdot)$ represents the greatest common divisor. Then the rank($\mathbf{D}_{\mathbf{c}}$) = $(M_1 + M_2) - \text{gcd}(M_1, M_2)$, which allows to resolve $\left\lfloor \frac{M_1 + M_2 - \text{gcd}(M_1, M_2)}{2} \right\rfloor$ frequency components. For orthogonal frequency components and a sampling interval $T_s = \frac{1}{f_o}$ the bandwidth that

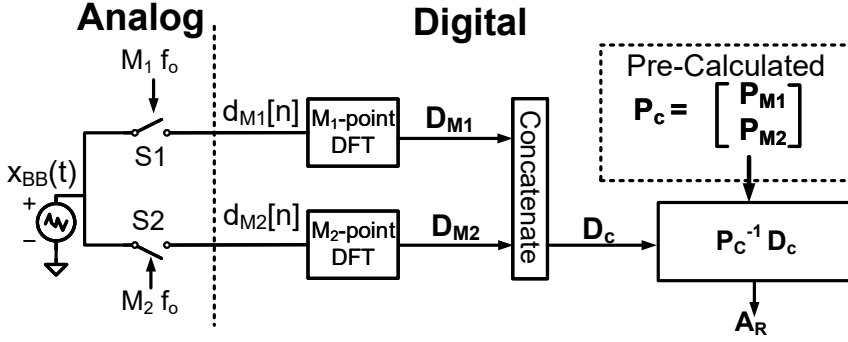


Figure 5.3: Schematic overview of MRU. The two samplers S_1 and S_2 are clocked at $M_1 f_o$ and $M_2 f_o$ respectively. After a period of $\frac{1}{f_o}$, M_1 and M_2 point DFTs are calculated and combined into \mathbf{D}_c . The vector \mathbf{D}_c and matrix \mathbf{P}_c allow for reconstructing the complex value (magnitude and phase) vector \mathbf{A} .

can be properly converted equals

$$BW_{\max} = \left(\left\lfloor \frac{M_1 + M_2 - \gcd(M_1, M_2)}{2} \right\rfloor - 1 \right) \cdot f_o \quad (5.17)$$

Note that in contrast to co-prime sampling systems [99], $\gcd(M_1, M_2) = 1$ is not required in our sampling system. The only requirement is that M_1 and M_2 are non-integer multiples of each other, as otherwise (5.17) reduces to:

$$BW_{\max} = \left\lfloor \frac{\max(M_1, M_2)}{2} \right\rfloor \cdot f_o \text{ for } \frac{M_1}{M_2} \text{ or } \frac{M_2}{M_1} \in \mathbb{N} \quad (5.18)$$

which is in accordance to the well known Nyquist theorem.

In a conventional Nyquist sampling system a single continuous signal band with bandwidth BW is sampled by a single sample frequency f_s . MRU allows for the bandwidth (5.17) to be spread over the frequency range for which the aliasing pattern \mathbf{P} is uniquely defined. This frequency range is:

$$0 \leq f \leq \text{lcm}(M_1, M_2) \cdot f_o \quad (5.19)$$

where $\text{lcm}(\cdot)$ represents the least common multiple.

The aliasing patterns as described by (5.11) and (5.12) have a periodicity of M . For the two sample rates M_1 and M_2 this results in an overall periodicity of the combined aliasing pattern that is the lcm of the two sample rates. This

means that the input signal frequencies can be spread over the frequency range given by (5.19) before MRU cannot solve frequency ambiguity due to aliasing.

One of the considerations in the selection of M_1 and M_2 is the total aggregated bandwidth, see (5.17), which is maximized when $\gcd(M_1, M_2) = 1$ (i.e. M_1 and M_2 are co-prime). Another point of consideration is the maximum frequency span over which the aggregated bandwidth can be spread out, see (5.19), which again is maximized when M_1 and M_2 are co-prime. Lastly, it follows that for co-prime M_1 and M_2 the aggregated sample rate $(M_1 + M_2) \cdot f_o$ can remain close to the Nyquist-Shannon limit of $2f_o|S|$ as long as all sub-carriers contribute to an increase of $\text{rank}(\mathbf{P}_c^{-1})$ in (5.16).

5.4 Qualitative Comparison of MRU with other techniques

5.4.1 Time-interleaving versus MRU

Time-interleaving of N sub-rate ADCs increases the aggregated bandwidth [104]. This requires a sample clock with N equally spaced phases, where the phase accuracy requirement increases N -fold to maintain the distortion performance [105, 106]. The increase in aggregated bandwidth increase the frequency span of a Nyquist zone, however the problem of aliasing will still occur (but at a higher frequency). In contrast to time-interleaving MRU allows an increase in aggregated bandwidth by using multiple sample rates that are non-integer multiples of one another. Any timing mismatch between the sample clocks can be fully compensated for by the MRU algorithm as described in section 5.5.2. However MRU needs the two samplers to both have a bandwidth equal or higher than the full signal bandwidth, where a time interleaved ADC only requires a single high-bandwidth sampler. The sub-ADCs in a time-interleaved ADC can have a lower bandwidth and thus consume less power.

MRU also allows for flexibility in the allocation of the aggregated bandwidth to different Nyquist zones. It is possible to combine MRU together with time-interleaving, however each time-interleaved ADC has to be calibrated as in a conventional time-interleaved system before MRU can be applied.

5.4.2 Anti-aliasing versus MRU

Increasing the order of the anti-aliasing filter or increasing the oversampling ratio increases the amount of suppression for signals outside the first Nyquist zone. However, any aliasing that occurs will still degrade the signal to noise ratio (SNR) of the reconstructed signal. MRU is not used to suppress the signals outside the first Nyquist zone and can be combined with multiple bandpass filters with distinct center frequencies. This will prevent strong signals outside the first Nyquist zone from saturating the ADC so that MRU can be used to unalias them. If after filtering a strong alias (such as an out-of-band interferer) folds into the band of interest, the wanted signal and the alias become indistinguishable. If the strong alias does not saturate the ADC, MRU can resolve this frequency ambiguity as long as the original frequency band of the alias is known, increasing the SNR of the wanted signal. MRU can be expanded to include more than two samplers, increasing the aggregated bandwidth over which the aliasing pattern \mathbf{P} is uniquely defined (5.19). Using more samplers with non-integer sample rates would therefore allow unaliasing of multiple interferers from the wanted signal which would otherwise be impossible with just conventional filtering [107, 108].

The programmability in [107] does allow multiple Nyquist zones to be covered, however the power consumption of such a programmable anti-alias filter is orders of magnitude more than the two ADCs used in our MRU algorithm. Even with the analog front-end driver in medium resolution state-of-the-art ADCs [109], the power consumption is lower than the state-of-the-art anti-aliasing filter for comparable analog bandwidth and SNR[108]. Furthermore, the filters in [107, 108] require a clock signal that has orders of magnitude higher frequency than the bandwidth of the signal itself. In comparison to this the presented MRU algorithm is based on sub-sampling and does not require a high frequency clock signal. However, MRU requires an additional sub-sampling clock frequency and extra digital signal processing.

5.4.3 Potential advantages of MRU

MRU allows for flexibility in the allocation of frequency bands, thereby providing more programmability compared to solutions with a single sampler. In a conventional sampling system aliasing can be prevented by changing the

sampling frequency. However, in case of a minimum sampling rate, the precision of the sample rate must increase for signals in higher Nyquist zones to prevent aliasing [101]. When multiple bandpass signals are present, the range of sample frequencies that do not alias will also decrease [102]. In contrast to conventional systems the clock rates in MRU have to be multiples of f_o , meet the aggregated bandwidth requirement in (5.17) and the bandpass signals should be in the frequency range as defined in (5.19) to prevent any aliasing that cannot be resolved.

Other potential advantages of MRU are the reduced sample-rate (and thus the digital data rate), since the aggregated sample rate can be significantly lower than $2f_o(\max(S) - \min(S))$. Furthermore MRU might in some scenarios replace the anti-aliasing filter as long as the occupied frequencies before aliasing are known and the signal does not clip the ADC. Furthermore, the proposed MRU algorithm requires samples over one single symbol period $\frac{1}{f_o}$, just as a conventional sampling scheme. The latency in [99] is approximately K times longer compared to conventional sampling, where K is the number of snapshots (300 and 2000 in [99]) used in averaging.

The MRU algorithm can also be extended to work directly with IQ signals. These systems typically already use two ADCs, hence the extra ADC overhead is removed when applying MRU in these systems. The modified equations for the reconstruction of IQ signals are given in Appendix B, along with the simulation results.

5.5 Impact of non-idealities

So far, it was assumed that the two samplers are ideal. However, in an actual implementation the digitized output suffers from non-idealities, e.g. gain mismatch, time delays, offsets, quantization and thermal noise. Any deviation from the ideal conditions degrades performance. This section discusses the impact of the most important non-ideal effects, using the reconstruction of OFDM signals as demonstration vehicle.

5.5.1 Inaccuracy propagation: the matrix condition number

The quantization noise and thermal noise of the ADC causes errors in the computation of \mathbf{D}_c . These errors propagate through the system of linear equations resulting in an error in the reconstructed complex value (magnitude and phase) vector, \mathbf{A}_R . The sensitivity of \mathbf{A}_R to these (small) errors depends on the condition number of \mathbf{P}_c , as \mathbf{P}_c has to be inverted. The condition number of a matrix is defined (in dB) as:

$$\kappa = 20 \log \left(\frac{\sigma_{\max}}{\sigma_{\min}} \right) \geq 0 \text{ dB} \quad (5.20)$$

where σ_{\max} and σ_{\min} are the largest and smallest singular values of the matrix.

A higher value of κ indicates a higher propagation of estimation errors in \mathbf{D}_c to the elements in \mathbf{A}_R and thus indicates a higher in error vector magnitude (EVM). Fig. 5.4 shows the impact of κ on the SNR of the reconstructed frequency spectra assuming two samplers with respective sample rates of 4.86 MHz ($M_1 = 324$) and 5.13 MHz ($M_2 = 342$) which yields an aggregated bandwidth of $BW_{\max} = 4.86$ MHz. For the simulation results in this figure, the aggregated signal bandwidth is increased from 490 kHz to BW_{\max} . For $BW < \frac{\max(M_1, M_2)f_o}{2}$ the signal conversion can be done by a single sampler, resulting in $\kappa = 0$. For $BW \geq \frac{\max(M_1, M_2)f_o}{2}$ the MRU algorithm is used resulting in $\kappa > 0$.

Fig. 5.4 shows both the condition number of \mathbf{P}_c and the maximum SNR degradation for different aggregated signal bandwidths for these sample rates. Additive white gaussian noise is used as the signal $x(t)$ to determine the SNR degradation due to the condition number. The SNR degradation reported is the difference between the noise power of an ideal sampling system (switches S_1 and S_2) operating at twice the aggregated bandwidth and that of the MRU algorithm. In order to show the effect of the condition number of the matrix \mathbf{P}_c on the SNR, the aggregated bandwidth of the MRU algorithm is varied. The ADCs sample rates are fixed at 4.86 MS/s and 5.13 MS/s. The ADCs in MRU might have a higher sample frequency than in a Nyquist rate sampling system, resulting in a lower noise power per DFT bin in MRU. This effect has been compensated for in the simulation results by normalizing the simulated SNR by the oversampling ratio. The maximum difference in the noise power between the additive white gaussian noise and the MRU output is reported in

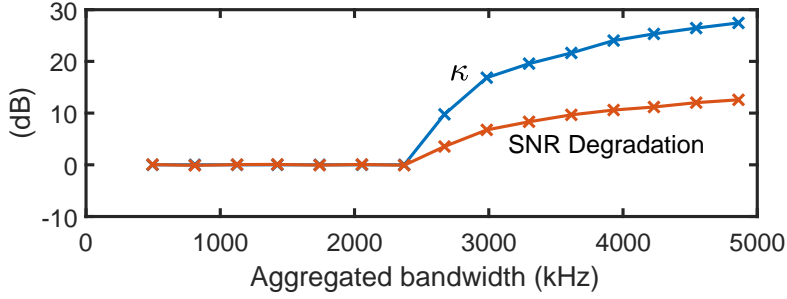


Figure 5.4: Condition number of \mathbf{P}_c and maximum SNR degradation for different aggregated signal bandwidths. The ADC sample rates are 4.86 MHz and 5.13 MHz. The SNR gain due to oversampling is compensated for in these results.

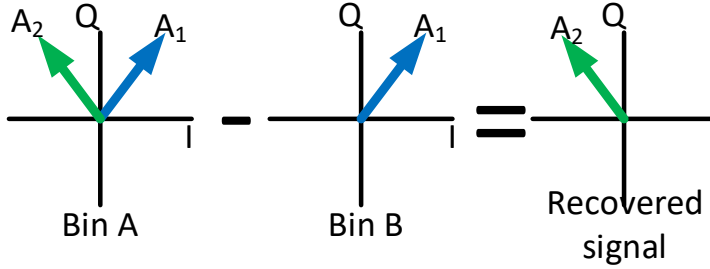


Figure 5.5: DFT Bin A contains both the complex vectors A_1 and A_2 and DFT bin B only contains A_1 . By subtracting Bin B from Bin A the complex vector A_2 is recovered for ideal sampling.

Fig. 5.4. Figure 5.4 illustrates that a higher condition number κ thus results in a higher SNR degradation, thus reducing the accuracy of the reconstruction. Note that in general the SNR degradation depends on the relative aggregated bandwidth with respect to the aggregated sample rate, hence a wide-band system can achieve similar results.

5.5.2 ADC Non-idealities and Calibration

This section discusses the most typical non-idealities for AD converters to be present. With ideal sampling, the algorithm performs the operation as shown in Fig. 5.5; A_2 is calculated by subtracting Bin B from Bin A resulting exactly in the actual vector A_2 .

Timing Mismatch

In Section III it is assumed that the two different sampling frequencies $M_1 f_o$ and $M_2 f_o$ have a common rising edge at the beginning of the sample sequence, resulting in $d_{M_1}[1] = d_{M_2}[1]$. This ensures that the complex values \mathbf{A} in \mathbf{D}_{M_1} and \mathbf{D}_{M_2} retain the same phase.

In case there is no common rising edge at the beginning of the sample sequence, and therefore no common first sample, $d_{M_1}[n]$ and $d_{M_2}[n]$ are effectively sampled with a constant time delay Δt between them.

Another source of timing mismatch is the path delay difference between individual paths. The switches S_1 and S_2 shown in Fig. 5.3 are part of a linear time variant system, therefore path delay mismatch between the two samplers S_1 and S_2 can be treated in the same manner as the static clock timing mismatch.

Time delay results in a phase rotation of $D[k]$ and is described by:

$$D_{\Delta t}[k] = \sum_{l=1}^L \left(\sum_{r=-\infty}^{\infty} (A_{\varphi,l} \delta(S_l - k - rM) + A_{\varphi,l}^* \delta(S_l + k - rM)) \right) \quad (5.21)$$

where $A_{\varphi,l} = e^{j\varphi_o S_l} A_l$, $A_{\varphi,l}^* = e^{-j\varphi_o S_l} A_l^*$ and $\varphi_o = 2\pi f_o \Delta t$. Fig. 5.7 illustrates the impact of a time mismatch.

The resulting DFT vector from (5.21) is described by:

$$\mathbf{D}_{\Delta t} = \mathbf{P}_{\varphi} \mathbf{A} \quad (5.22)$$

where \mathbf{P}_{φ} is described by:

$$P_{\varphi}[k, 2l] = \sum_{r=-\infty}^{\infty} \left(e^{j\varphi_o S_l} \delta(S_l - k - rM) \right) \quad (5.23)$$

$$P_{\varphi}[k, 2l + 1] = \sum_{r=-\infty}^{\infty} \left(e^{-j\varphi_o S_l} \delta(S_l + k - rM) \right). \quad (5.24)$$

The calibration for timing mismatch is done by providing a known single sinusoidal signal as the input and comparing the phase of the two output

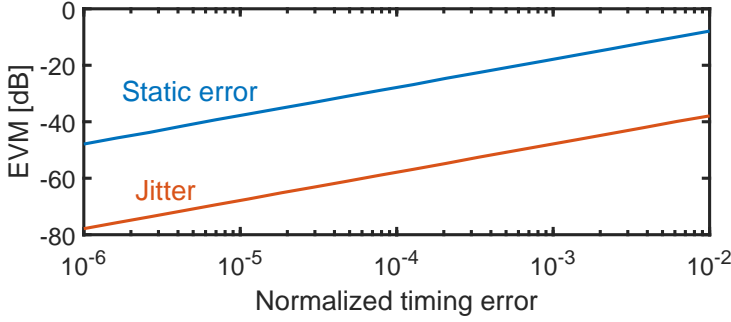


Figure 5.6: Simulated EVM versus normalized timing error for a static timing error and jitter. The static time delay error is defined between the common rising edges of the two sample clocks and the error is normalized to $\frac{1}{f_o}$, which. The timing error caused by jitter is added to both the ADC sampling clocks. The standard deviation of the jitter is normalized to the ADC sampling period.

DFTs at the input sinusoidal frequency. The timing mismatch is calculated from the phase difference by

$$\Delta t = \frac{\Delta\phi}{2\pi f_{\sin}} \quad (5.25)$$

where $\Delta\phi$ is the phase difference between the two output DFTs at the input sinusoidal frequency, f_{\sin} . This is a one-time calibration.

Fig. 5.6 shows the (MATLAB) simulated effect of static timing mismatch between the first rising edges of both sample clocks on the expected EVM when using MRU. Here the timing mismatch is normalized to the symbol period $\frac{1}{f_o}$. The EVM degradation without any calibration due to timing mismatch is 10dB/decade, which behaves similarly to SNR degradation due to timing mismatch in non-calibrated two-channel time-interleaved ADCs [105].

Another source of timing mismatch is jitter in the ADC clocks, which causes dynamic errors in Δt . In conventional ADCs jitter decreases the SNR of the sampled waveform, hence it will also decrease the accuracy of the MRU algorithm. Conventionally jitter (due to noise) is a random process, which can often be described by a Gaussian distribution with zero mean and standard deviation σ_t . Fig. 5.6 shows the simulated EVM for different σ_t normalized to the ADC sample period.

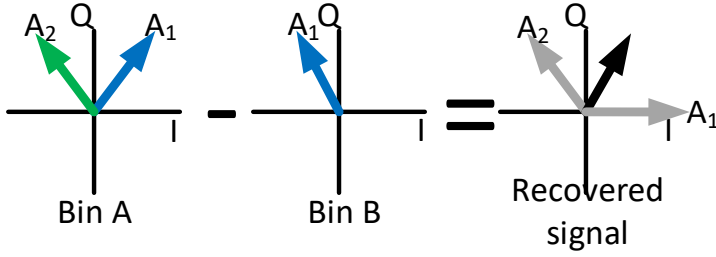


Figure 5.7: Signal recovery in the presence of time difference between the sample points at the start of the beat pattern. Here DFT Bin A contains both the complex vectors A_1 and A_2 and DFT bin B only contains a time shifted version of A_1 . By subtracting Bin B from Bin A the complex vector A_1 is only partially cancelled and still contributes to the estimation of A_2 .

Gain error

The MRU algorithm uses two samplers, or two ADCs. These ADCs may have differences in their transfer from the analog input voltage to the digital code, resulting in a static gain error. The MRU algorithm however assumes the contributions of \mathbf{A} to \mathbf{D}_{M_1} and \mathbf{D}_{M_2} to be equal, leading to errors, see Fig. 5.8. In this work the ADCs are assumed to have unity gain. To compensate the gain error α_{ADC} , \mathbf{D}_C must be normalized to the gain of the ADC $(1 + \alpha_{\text{ADC}})$:

$$\mathbf{D}_{C,\text{norm}} = \begin{bmatrix} \frac{\mathbf{D}_{M_1}}{1 + \alpha_{\text{ADC}1}} \\ \frac{\mathbf{D}_{M_2}}{1 + \alpha_{\text{ADC}2}} \end{bmatrix}. \quad (5.26)$$

A static gain error can be compensated for in the digital domain and is performed by comparing the magnitude of two output DFTs at the input sinusoidal frequency.

Fig. 5.9 shows the simulated effect of the gain error α_{ADC} on EVM when using MRU. In this simulation it is assumed that only a single ADC has a gain error, and the other ADC has unity gain. The EVM degradation due to the gain error α_{ADC} is 10dB/decade, which is similar to SNR degradation due to gain errors in time-interleaved ADCs [105]. Furthermore, simulations demonstrate that dynamic gain errors follow the same trend as static gain errors.

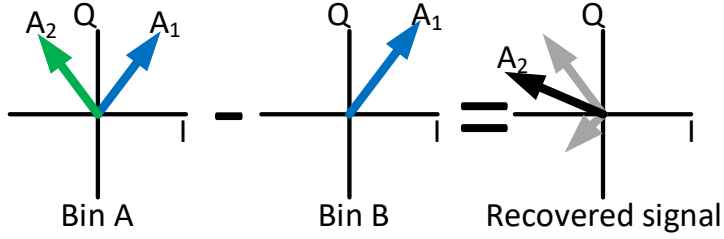


Figure 5.8: Signal recovery in the presence of gain mismatch between the ADCs. DFT Bin A contains complex vectors A_1 and A_2 and DFT bin B contains a scaled version of A_1 . By subtracting Bin B from Bin A the complex vector A_1 is only partially cancelled and still contributes to the estimation of A_2 .

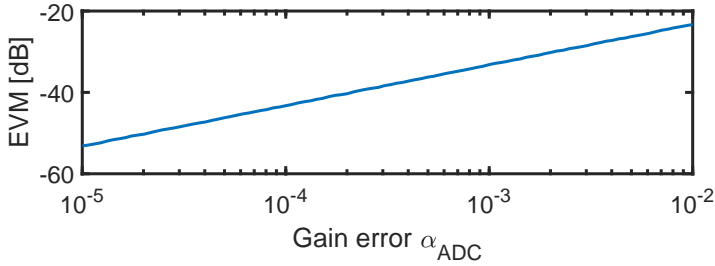


Figure 5.9: Simulated EVM versus gain error α_{ADC} . In this simulation only a single ADC has a gain error, and the other ADC has unity gain.

Offset

Offset of both ADCs end up in the first bins of \mathbf{D}_{M_1} and \mathbf{D}_{M_2} . The resulting dataset is obtained by concatenating the two DFT datasets and not by switching between the outputs of the two ADCs. Therefore there is no up-conversion of the DC-offset; consequently offset errors can be compensated in the same manner as for a traditional ADC. The offsets for the two ADCs are obtained from the DC bin of the respective output DFTs.

5.6 Measurement results

Fig. 5.10 shows the measurement test board containing two energy and area-efficient 10 bit SAR ADCs as presented in [110], which are used in this demon-

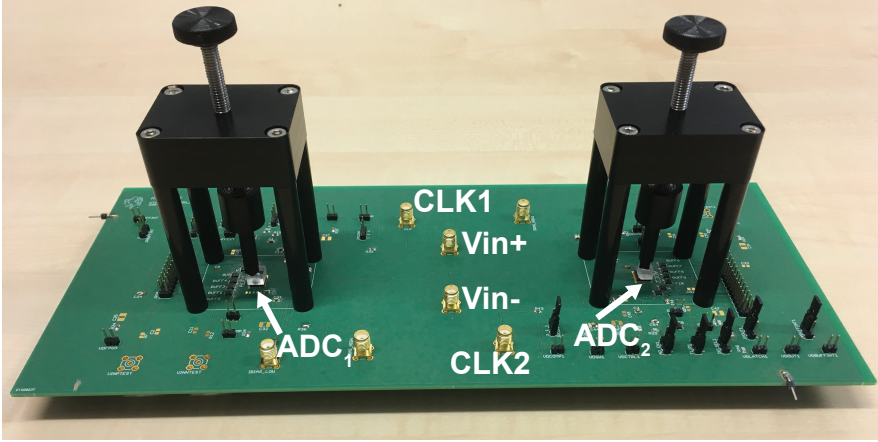


Figure 5.10: Photograph of the measurement PCB.

strator since they were available in this project. Note that the algorithm is not limited to low speed ADCs and can also be used with high speed ADCs. The two ADCs share the same differential inputs and are clocked separately. The ADC architecture is an asynchronous one wherein the falling edge of the sample clock denotes the end of the sampling period and the internal logic controller is self-timed and generates all the ADC conversion cycles.

The accuracy of the ADCs limit the maximum achievable EVM and the relation between SNR and EVM_{RMS} is $\text{EVM}_{\text{RMS}} \approx \text{SNR}^{-\frac{1}{2}}$ [111] for a noise limited system. For the ADCs used in the measurements, the signal to noise and distortion ratio the signal to noise and distortion ratio (SINAD) > 56 dB, hence the EVM can be determined up to an accuracy of approximately 0.16% which is sufficient for most applications. For example 256-QAM LTE requires an $\text{EVM} < 3\%$ [112] for which typically 8 to 12 bit ADCs are used [113, 114].

Fig. 5.11 shows the block diagram of the measurement setup. At the end of each conversion, the signal EoC indicates to the FPGA to latch the data for reconstruction. The ADC output bits are collected by the respective FPGAs (serial-to-parallel conversion), which then connects to a computer with MATLAB running the MRU algorithm.

To demonstrate the effectiveness of MRU three different measurements are performed. For these measurements OFDM signals are used, since they are a well known type of orthogonal signal. Appendix C discusses the charac-

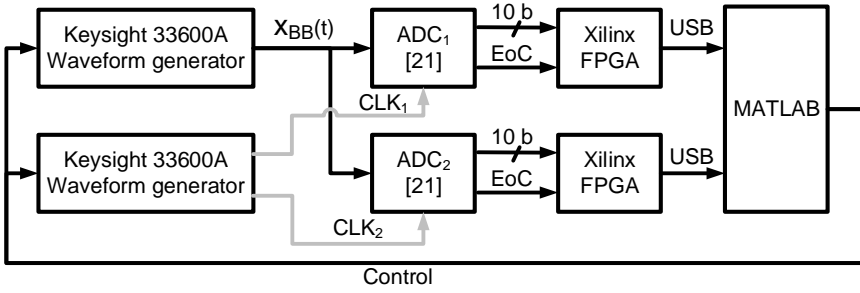


Figure 5.11: Block diagram of the measurement setup.

terization of the harmonics of an RF-signal as another use case. The first measurement demonstrates the ability of MRU to separate an OFDM signal where due to sampling sub-carriers are aliased into the first Nyquist zone, hence becoming indistinguishable from each other. The second measurement demonstrates that MRU can be used to reconstruct aliased signals outside the first Nyquist zone, where a single OFDM band covers higher Nyquist zones. The third measurement combines the results of the two previous measurements for a dual-band signal, demonstrating the ability of MRU to simultaneously resolve for frequency ambiguity and individually reconstructs the band-pass signals. Although the test signals used in this section are OFDM, MRU in general can be used to detect and reconstructs signals with any orthogonal frequency basis.

5.6.1 Reconstruction of an aliased signal centred around $f_s/2$

To demonstrate the algorithm a 180 kHz BW OFDM signal centred around 2.505 MHz and ranging from 2.415 MHz to 2.595 MHz is used as a test signal. This signal mimics a continuous signal down-mixed to baseband, having no out-of-band frequency components. The OFDM signal consists of 12 sub-carriers spaced at 15 kHz modulated with a 16-QAM constellation and a Null-carrier at 2.505 MHz for a total of 13 sub-carriers. The Null-carrier is used as a reference for reconstruction and does not influence the performance of the MRU algorithm. Since the sub-carrier spacing is 15 kHz, $f_o = 15$ kHz to retain orthogonality of the sub-carriers after sampling. The input signal spectrum is shown in Fig. 5.12(a).

This OFDM signal is simultaneously sampled by ADC_1 and ADC_2 at 4.86

5. RECONSTRUCTING ALIASED FREQUENCY SPECTRA BY USING MULTIPLE SAMPLE RATES

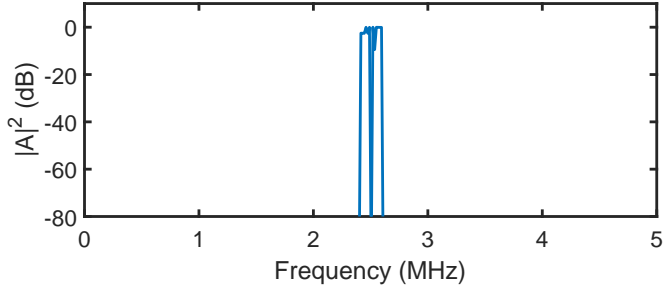
Table 5.1: Aliasing pattern when the OFDM signal is sampled at 4.86 MS/s as described by (5.5). Only aliasing to the first Nyquist zone is shown ($r=-1$ and $r=0$).

	Input frequency	Frequency after sampling
$r = -1, f + f_s$	-2.595 MHz	2.265 MHz
	-2.415 MHz	2.445 MHz
$r = 0, f$	2.415 MHz	2.415 MHz
	2.595 MHz	2.595 MHz

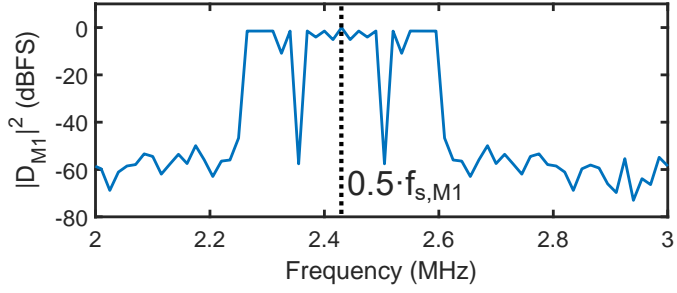
MS/s ($M_1=324$) and 5.13 MS/s ($M_2=342$) respectively, since these sample rates are close to the maximum sample rates of the available ADCs. However, the MRU algorithm can be extended to (significantly) higher sample rates and correspondingly a higher aggregated input signal bandwidth. After sampling the input signal with these sample rates aliasing occurs. For simplicity only aliasing to the positive half of the first Nyquist zone is considered and is shown in Table 5.1. The sampled signal frequency span ranges from 2.265 MHz to 2.595 MHz and the frequency range from 2.415 MHz to 2.445 MHz now contains multiple aliased carriers to a single DFT bin. Similarly the aliasing for ADC_2 is calculated and shown in Table 5.2. Here the frequencies from 2.535 MHz to 2.595 MHz contain multiple aliased carriers to a single DFT bin. Fig. 5.12(b) and 5.12(c) show the output spectra $|\mathbf{D}_{\mathbf{M}_1}|^2$ and $|\mathbf{D}_{\mathbf{M}_2}|^2$ of respectively ADC_1 and ADC_2 zoomed in around the signal of interest for a single OFDM symbol out of a 200 symbol sequence. After sampling the data is passed to the MRU algorithm to reconstruct the input signal. M_1 and M_2 are selected such that the two ADCs operate near to their maximum throughput rate. If the ADCs can operate at higher sample rates, M_1 and M_2 can be increased while keeping the aggregated bandwidth constant. This has similarities with oversampling and would result in a decrease in the condition number, thereby improving the SNR (and EVM), see Fig. 5.4.

Consequently, a conventional sampling system cannot reconstruct this (aliased) signal without changing the sample frequency. Even so, when the signal frequency changes or an additional bandpass signal is added the constraints on the sample rate to prevent any aliasing increases in conventional sampling.

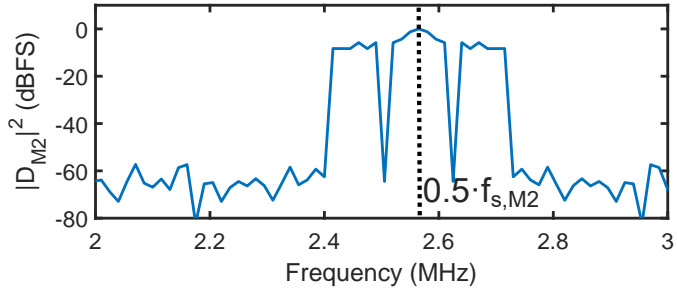
Fig. 5.12(d) shows the output of the MRU algorithm and Fig. 5.12(e)



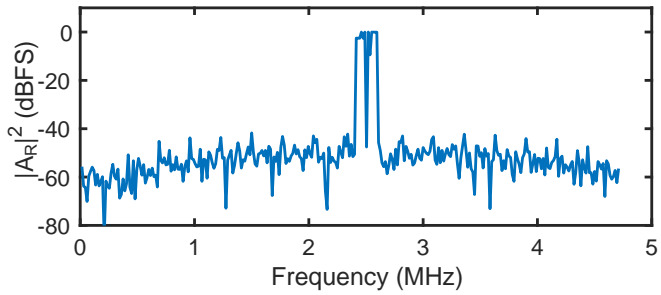
(a)



(b)



(c)



(d)

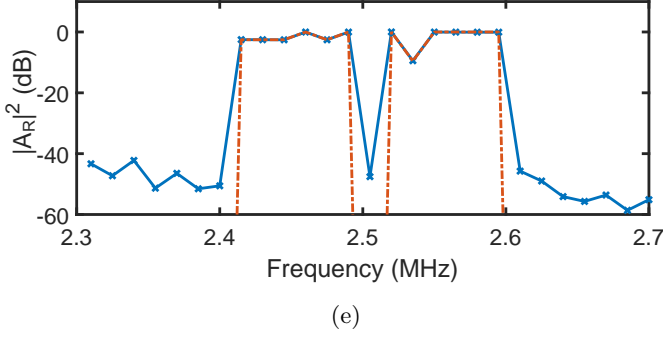


Figure 5.12: Measured spectral snapshot of a single OFDM symbol out of a 200 symbol sequence with 12 sub-carriers centred at 2.505 MHz. (a) The spectrum of the 180 kHz OFDM signal centred at 2.505 MHz. (b) Zoomed in DFT spectrum $|\mathbf{D}_{\mathbf{M}_1}|^2$ around the signal of interest when the input signal is sampled at 4.86 MS/s. (c) Zoomed in DFT spectrum $|\mathbf{D}_{\mathbf{M}_2}|^2$ around the signal of interest when the input signal is sampled at 5.13 MS/s. (d) Reconstructed spectrum of the OFDM symbol by using the MRU algorithm. (e) Zoom-in of (d) showing both the measured (solid line) and ideal input (dash line) signals.

Table 5.2: Aliasing pattern when the OFDM signal is sampled at 5.13 MS/s as described by (5.5). Only aliasing to the first Nyquist zone is shown ($r=-1$ and $r=0$).

	Input frequency	Frequency after sampling
$r = -1, f + f_s$	-2.595 MHz	2.535 MHz
	-2.415 MHz	2.715 MHz
$r = 0, f$	2.415 MHz	2.415 MHz
	2.595 MHz	2.595 MHz

shows a zoom in together with the ideal input signal. The reconstructed signal shows that the OFDM signal is indeed centred around 2.505 MHz and the frequency ambiguity in the DFTs of ADC_1 and ADC_2 is resolved. The power level of the sub-carrier at 2.505 MHz is 9.5 dB lower than the maximum measured sub-carrier power as it lies on the inner circle of the 16-QAM constellation in Fig.5.13. The effect of ADC noise and condition number is barely visible in Fig. 5.12(e): the measured and ideal input spectra lie on top of each other. The recovered spectra in Fig. 5.12(e) seems to approach the

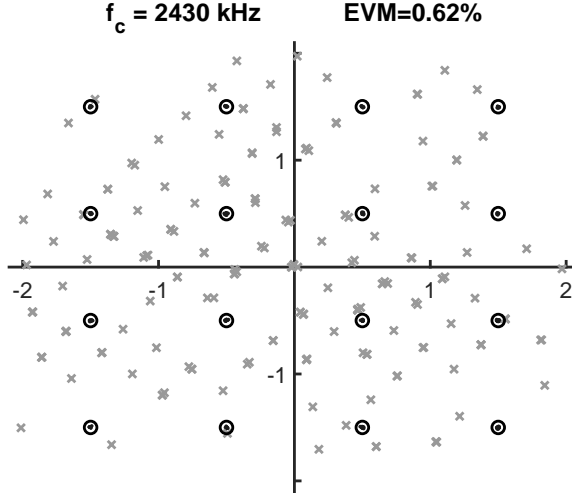


Figure 5.13: Measured constellation diagram of the sub-carrier with the highest EVM for the OFDM signal in Fig.5.12. The circles are the ideal constellation points, the dots are the reconstructed results when using the MRU algorithm and the crosses are the reconstructed results of a single ADC.

ideal input, however there are some errors which are hardly visible due to the logarithmic scale. The upper boundary for the errors is set by the accuracy of the ADC. The second most important factor of performance degradation is the propagation of errors due to the MRU algorithm, where the degradation is limited to the condition number κ . κ is determined by the chosen sample frequencies and the selected sub-carriers.

To determine the effect of the MRU algorithm on the quality of the received OFDM signal, the EVM for every sub-carrier is determined. The RMS EVM over N -symbols for an M -ary signal constellation is calculated as:

$$\text{EVM}_{\text{RMS}} = \frac{\sqrt{\frac{1}{N} \sum_{i=1}^N |S_{\text{ideal},i} - S_{\text{meas},i}|^2}}{\sqrt{\frac{1}{M} \sum_{i=1}^M |S_{\text{ideal},i}|^2}} \quad (5.27)$$

where $S_{\text{ideal},i}$ and $S_{\text{meas},i}$ are respectively the ideal and measured vectors corresponding to the i th symbol.

Fig. 5.13 shows the constellation before and after applying the MRU algorithm for the sub-carrier with the worst EVM due to quantization plus aliasing

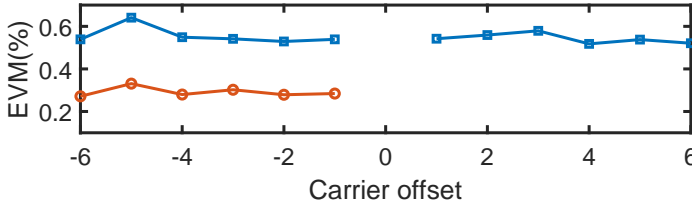


Figure 5.14: Measured EVM over 200 symbols of each sub-carrier of the OFDM signal after demodulation by using the MRU algorithm (squares) and a single ADC (circles). For the single ADC only the EVM of the sub-carriers that can be successfully demodulated is shown.

and Fig. 5.14 shows the EVM of all the sub-carriers in the OFDM signal measured over 200 symbols. The higher sub-carriers in Fig. 5.12 are corrupted by in-band interference due to aliasing, which prevents demodulation of the signal in a conventional way. It shows that the modulated data is recovered with an EVM lower than 0.62% (-44 dB). To compare the effect of degradation due to the MRU algorithm alone, the EVM for the lower sub-carriers in Fig. 5.14 is also determined. These lower sub-carriers in $|\mathbf{D}_{\mathbf{M}_2}|^2$ are not corrupted by aliasing. The average EVM for these sub-carriers is 0.28% (-50 dB). Using the MRU algorithm the signal can be demodulated at a cost of about 12 dB higher SNR compared to the case when there is no in-band interference. The 12 dB SNR degradation translates to 6 dB EVM degradation in case of no in-band interference, since $\text{EVM}_{\text{RMS}} \approx \text{SNR}^{-\frac{1}{2}}$ [111]. The measured 12 dB SNR degradation agrees with the simulated 12 dB SNR degradation as shown in Fig. 5.4.

5.6.2 Reconstruction of aliased signal outside first Nyquist Zone

The performance of the MRU algorithm when demodulating a single signal in higher Nyquist zone is demonstrated. The operating frequency of the ADCs is lowered compared to the previous measurement to allow sampling in multiple Nyquist zones, since the input bandwidth of the used low power ADCs is limited to 5 MHz. The sample rates are set to 1.17 MS/s ($M_1=78$) and 0.93 MS/s ($M_2=62$) for ADC_1 and ADC_2 respectively. The OFDM signal from the previous measurements is used and is centred around $N \cdot 1.125$ MHz in

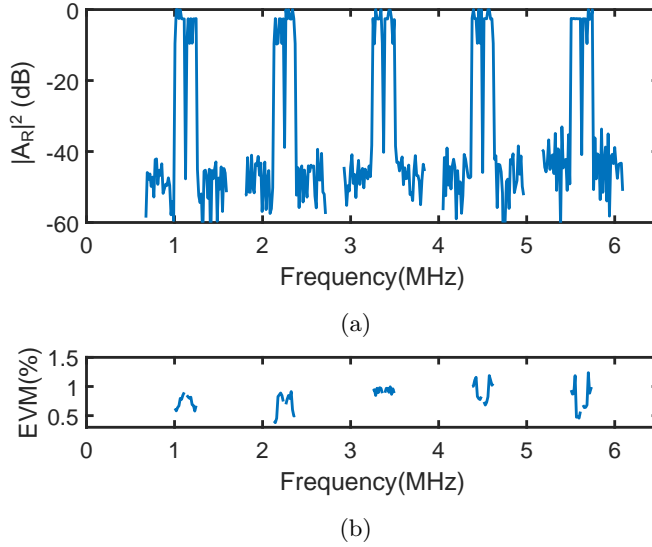


Figure 5.15: (a) Sequentially measured spectra of a single OFDM symbol out of a 200 symbol sequence with the center frequency in different Nyquist zones. (b) EVM corresponding to the OFDM signal in different Nyquist zones.

each sequential measurement where $1 \leq N \leq 5$.

Fig. 5.15(a) shows the sequentially reconstructed spectra up to 5.625 MHz using the MRU algorithm; Fig. 5.15(b) shows the EVM of the OFDM sub-carriers over all center frequencies in the different Nyquist zones. These figures show that the input signal frequencies in multiple Nyquist zones were recovered.

5.6.3 Reconstruction of two aliased signals from distinct Nyquist zones

To demonstrate the ability of the MRU algorithm to concurrently solve frequency ambiguity and determine the sub-carrier frequency before sampling, a dual-band OFDM signal that is spread over different Nyquist-zones is used as an input signal. After sampling the two OFDM bands become indistinguishable from each other, however MRU can resolve this allowing individual reconstruction of the two bands and determining the EVM.

The center frequency of the first OFDM band is 1.8 MHz (BW = 180 kHz) and that of the second OFDM band is 7.05 MHz (BW = 750 kHz), resulting

in aliasing in both DFT spectra. The sample rates for ADC_1 and ADC_2 are set to 2.43 MS/s ($M_1 = 162$) and 2.565 MS/s ($M_2 = 171$). The BW_{\max} of this system is 2.43 MHz (see (5.17)). Since the aggregated BW of the input signal (0.93 MHz) is smaller than 2.43 MHz, the MRU algorithm can solve the frequency ambiguity caused by sampling allowing reconstruction of both OFDM bands. The aliasing matrix \mathbf{P} is chosen such that it covers all the sub-carriers in the dual-band OFDM signal.

The measured frequency spectra of a single OFDM symbol by both ADCs is shown in Fig. 5.16(a) and 5.16(b) in blue. The original input spectra are added in solid grey and dashed black lines, and any overlap between the two input spectra would impact the demodulation performance significantly. In Fig. 5.16 the ratio P_R between the average power of the first and second band-pass signal is set to -20 dB for illustration purposes. Fig. 5.16(c) shows the recovered frequency spectrum after applying the MRU algorithm, clearly showing that the frequency ambiguity is removed. Since the MRU algorithm does not solve the frequency bands between the two OFDM bands there is no data corresponding to those frequencies. Fig. 5.16(d) shows the zoom-in around the first band for a single OFDM symbol and Fig. 5.16(e) shows the zoom-in of the second band for a single OFDM symbol. Compared to a conventional sample system that would sample at $2f_{\text{span}} \approx 15$ MHz, MRU reduces the individual sample rates (2.43 MS/s and 2.565 MS/s) and output data rates by a factor 6.

Fig. 5.17 shows the EVM of the demodulated dual-band OFDM signal with and without the MRU algorithm. The power ratio P_R between the two band-pass signals is swept from -18 dB to 18 dB in steps of 6 dB and the signal is scaled in such a way that the total dual-band signal range exactly fits the full-scale range of the ADC to minimize quantization errors and to also avoid distortion due to clipping. For low power ratios the increase in EVM by using the MRU algorithm is due to the fact that the (desired) signal amplitude is also decreased to prevent clipping in the ADC, thereby reducing the SNR of the input.

From Fig. 5.17 it can be concluded that by using the MRU algorithm, EVM can be improved by a maximum of 42 dB for this setup, allowing successful demodulation and characterization of the wanted signal in the presence of strong signals which after sampling can become in-band, e.g. intermodu-

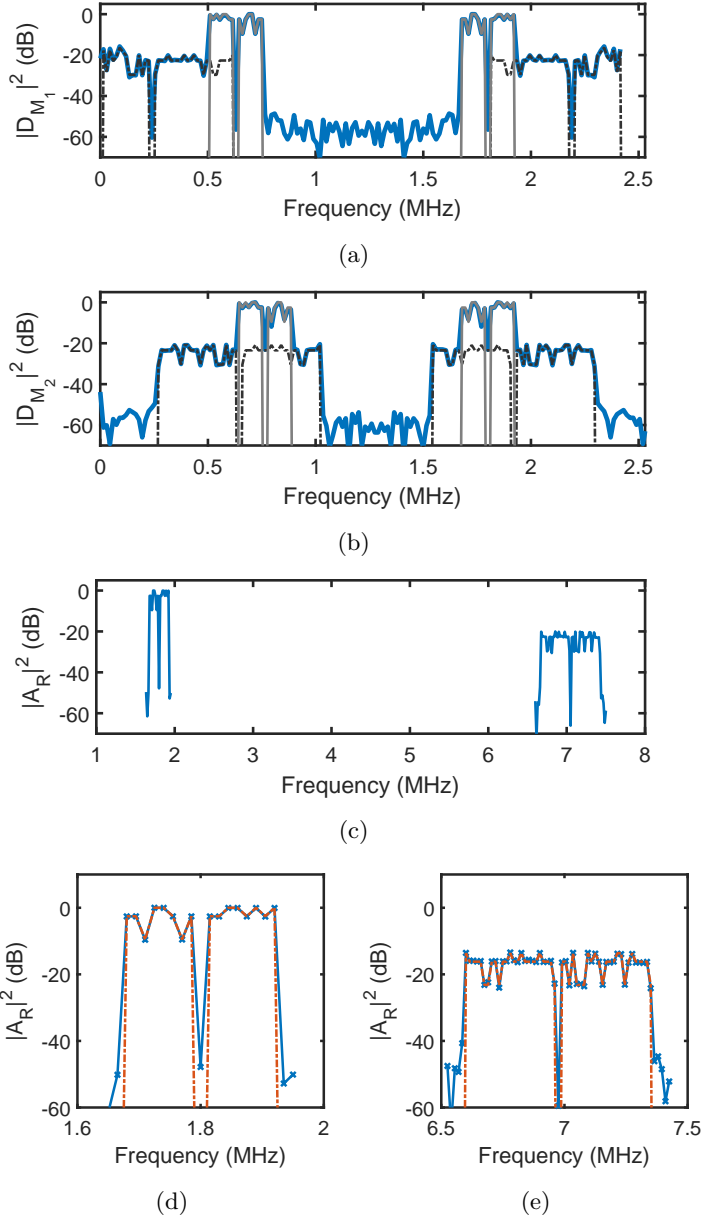


Figure 5.16: Measured spectra of the dual-band OFDM signal for a single OFDM symbol out of a 200 symbol sequence. (a) 2.43 MS/s DFT spectrum $|D_{M_1}|^2$ (solid blue) with the ideal input signals (dash black and solid grey line). (b) 2.565 MS/s DFT spectrum $|D_{M_2}|^2$ (solid blue) with the ideal input signals (dash black and solid grey line). (c) Recovered split-bandwidth spectrum. The dual-band OFDM signal is separated allowing independent reconstruction. (d) and (e) shows the zoom-in of (c) with both the measured (solid line) and the ideal input (dash line).

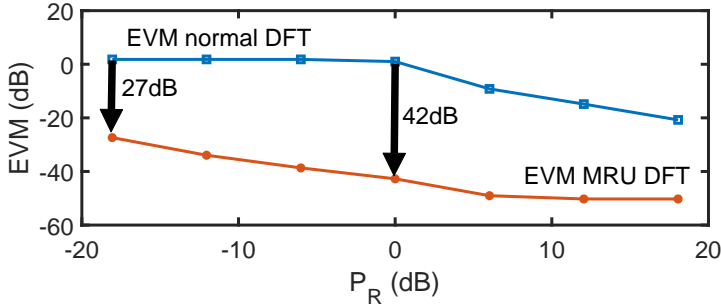


Figure 5.17: EVM of a demodulated OFDM signal in the presence of another OFDM signal with and without the MRU algorithm. The maximum improvement in EVM by using our MRU algorithm is 42 dB and is limited by the setup. The lower limit in EVM of the MRU algorithm is due to the SNR of the ADC and the SNR degradation due to the condition number. The total input signal is scaled to fit within the ADCs dynamic range to avoid clipping.

lation products. For a power ratio of -18 dB the desired signal can still be demodulated with an EVM of -27 dB.

5.7 Conclusion

A novel multi-rate unaliasing algorithm (MRU) that solves frequency ambiguity due to aliasing of (sub-)sampled multiband signals with an orthogonal frequency basis is presented. Sampling the input signal at two different sample frequencies that are non-integer multiples of one another results in two distinct systems of linear equations. Combining them increases the overall rank of the system of linear equations allowing the MRU algorithm to solve frequency ambiguity due to sampling. Additionally the MRU algorithm allows reconstruction of the input signal spectrum, which can be (sparsely) spread over a wide bandwidth equal to the least common multiple of the two sample frequencies. Furthermore MRU allows reconstruction of an aliased signal with an aggregated bandwidth close to the Nyquist-Shannon limit. The MRU algorithm can solve for frequency ambiguity in multiple Nyquist zones by using two different clock rates and some additional digital signal processing. A demonstrator setup comprising of two 10 bit ADCs clocked at two different sample rates is used to demonstrate the effectiveness of the MRU algorithm in the reconstruction of aliased signals.

Chapter 6

Theory and Implementation of a Load-Mismatch Protective Class-E PA System

6.1 Introduction

Efficiency is an important Power Amplifier (PA) parameter in modern battery-powered systems. Consequently, Switch-Mode PAs (SMPAs) compare favorably to linear PAs due to their exceptionally high efficiency¹. The class-E PA topology is one such SMPA, employing a resonant waveform-shaping network to achieve the Zero-Voltage Switching (ZVS) and Zero-Slope Switching (ZSS) conditions necessary to achieve high (ideally 100%) efficiency [19, 115–118]. A schematic representation of a class-E PA and its switch voltage and current waveforms under ZVS and ZSS conditions are shown in Figure 6.1a and b, respectively [119]. On the downside, class-E PAs are sensitive to load mismatch conditions: the resulting de-tuning of their resonant networks causes unwanted effects such as high switch currents and high peak switch voltages, which can result in PA degradation or even instantaneous destruction [40, 120–122].

Antenna impedances are a strong function of their EM environment, with Voltage Standing Wave Ratios (VSWRs) reaching up to 10:1 [14, 123, 124].

¹This chapter consists of material previously published in IEEE Transactions on Circuits and Systems Part I: Regular Papers [75] and it is reformatted to a thesis form.

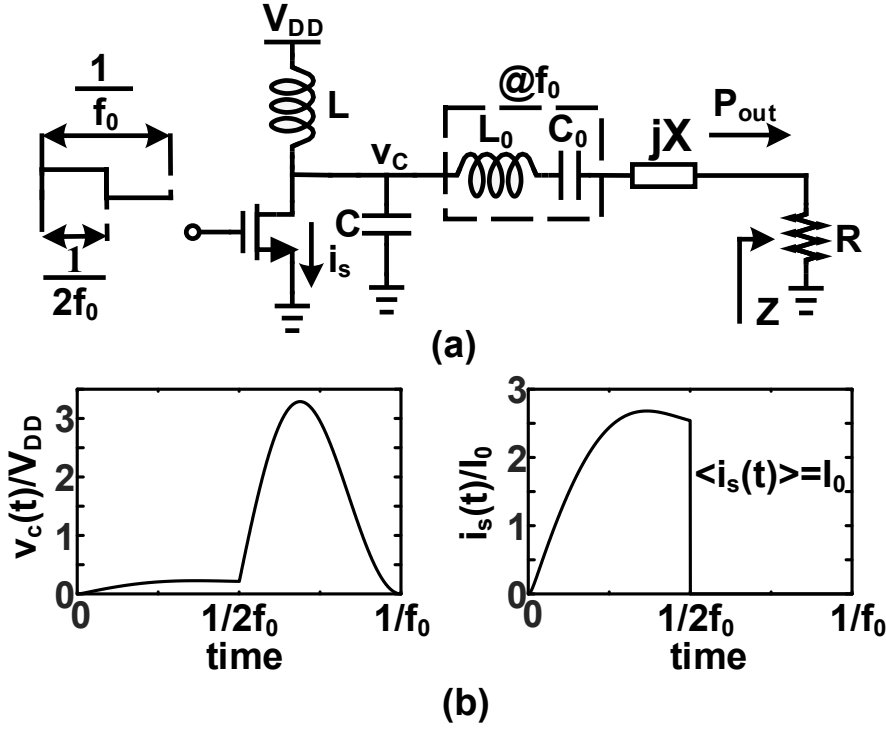


Figure 6.1: (a) Schematic representation of a single-ended class-E PA (b) Switch voltage and current waveforms for a class-E PA designed for ZVS and ZSS with $q = 1.412$, $d = 1$ and $m = 0.05$, operating under nominal conditions [119].

Under such load mismatch conditions, class-E PA reliability is degraded by several phenomena. Firstly, an increase in PA dissipation due to non-ZVS conditions can cause PA degeneration through thermal (over-)stress. Additionally, the associated increase in average switch current may damage the switch through electromigration [71, 125] or hot carrier degradation [115, 126]. Lastly, and most importantly, extreme switch voltage excursions exceeding the switch transistor breakdown voltage limit can cause instantaneous and permanent failure as a consequence of gate-oxide breakdown [66, 127].

There is prior published work concerning the protection of PAs under load mismatch conditions. Karoui et al. [128] report a self-protecting class-A PA that utilizes an analog control loop to automatically keep output stage current below a set limit. Applying this type of self-protecting system to class-E PAs results in waveform corruption and a reduction in efficiency. Scuderi et

al. [129] demonstrated a class-C-E PA utilizing bias variations and variable gain control to decrease PA gain in order to reduce active device voltage stress under load mismatch. This technique is not easily applied to switched-mode PAs (e.g. class-E PAs) because their gain cannot be readily tuned. Bowers et al. [72] presented a self-healing class-AB PA system, in which PA bias-point control is combined with active load tuning to achieve improved operating performance under load mismatch conditions. Their load-tuning technique could be adapted for use in a self-protective system, at the cost of reduced efficiency and increased complexity. A technique aimed specifically at class-E PAs was demonstrated by Wei et al. [130]. In it, the peak switch voltage is sensed and kept constant by varying the gate drive level and thereby varying the switch on-resistance R_{ON} . Unfortunately, the reduction in switch drive and associated increase in switch transistor R_{ON} degrades PA switching performance, and hence significantly degrades output power and efficiency. Another option is the application of isolators/circulators to isolate the PA from reflections due to load mismatch. However, at frequencies up to tens of GHz, their bulky nature renders them impractical for use in integrated circuits, while reflected power is absorbed in a termination resistor, significantly impacting efficiency under load mismatch conditions.

We previously proposed and demonstrated a new technique for protecting a class-E PA under load mismatch [119] with low impact on output power and efficiency. With the technique in [119], the (relative) resonance frequency (q) of the class-E PA switch tank is tuned in such a way that switch transistor (over-)stress due to load impedance variations is minimized. In this chapter, we present the theoretical foundation for this technique, which is backed up by simulation results and more measurement results. It was shown in [40] that changing the relative resonance frequency of the switch tank and changing the switch duty cycle have approximately opposing effects on class-E PA behavior. The use of this duty cycle tuning as a complementary method to switch tank tuning is also described.

This chapter is organized as following. Section 6.2 reviews the reliability concerns relevant to class-E PAs. In section 6.3, the theoretical effects of load mismatch on class-E PAs are presented in load-pull contours. The consequences of the observed variations in PA behavior are discussed. Section 6.4 presents a discussion of second-order effects that were not taken into account

in the theoretical treatise in Section 6.3, focusing on the resulting differences in PA behavior. Section 6.5 shows the effects of load mismatch on class-E PAs by utilizing load-pull contours obtained from simulation results. Based on these contours, a Safe Operating Areas (SOA) is drawn to indicate where the PA is at risk of degradation or destruction. Section 6.6 deals with the effects of changing the relative resonance parameter, q , and duty cycle, d , on PA behavior. This shows that a proper selection of the q parameter can move the SOA to enclose almost any load impedance, while variation in the d parameter allows for limited SOA tuning. Section 6.7 presents measurements performed on a class-E PA system, both for non-tuned and tuned cases, demonstrating the validity of the shown theory and simulations. Section 6.8 shows the implementation of a self-protecting system for the class-E PA, leveraging the results from section V. Measurement results are shown and compared to the experimental and theoretical data. Finally, in section 6.9, conclusions drawn from the chapter are summarized.

6.2 Reliability concerns in class-E PAs

6.2.1 Gate-oxide breakdown

When a high voltage exceeding the specified breakdown limits is applied to a MOS transistor, gate-oxide breakdown can occur, typically breaking bonds in the transistor gate-oxide [68, 69]. Although gate-oxide breakdown can manifest in several ways, this work mainly focuses on hard breakdown, wherein a highly conductive path is formed in the gate-oxide [68, 69]. This conductive path significantly reduces the off-resistance of a MOS transistor, heavily compromising its performance [115].

6.2.2 Hot carrier degradation

When a high lateral field is present in an MOS transistor, at drain-source voltages exceeding the material bandgap, carriers can gain significant kinetic energy [131, 132]. Such carriers, denoted as “hot carriers”, can amass enough energy to produce impact ionization upon collision with the crystal lattice. This process can generate surface defects, leading to reduced carrier mobility in the channel and the trapping of charges in the gate oxide, shifting the

local threshold voltage [131, 132]. These effects manifest as an increase in on-resistance and switch turn-on voltage, degrading the performance of SM-PAs. For significant hot carrier degradation to occur, both a high drain-source voltage and substantial drain current must be present, which only occur under severe load-mismatch conditions in SMPAs that are designed for ZVS [115].

6.3 Class-E PAs under (non-)nominal conditions

6.3.1 Class-E PA basics

Class-E PAs in single-ended form consist of a (transistor-based) switch and two resonant (LC) tanks. A schematic representation of a single-ended class-E PA is shown in Figure 6.1a. The switch tank, $L - C$, is dimensioned to shape the switch node voltage $v_c(t)$ to achieve ZVS and ZSS conditions, as represented in Figure 6.1b. The second tank at the output, $L_0 - C_0$, is a band-pass filter designed to pass energy to the load only at the fundamental frequency, f_0 . The relative duty cycle parameter, d [115], describes the duty cycle of the switch drive voltage as

$$S \triangleq \begin{cases} \text{ON}, & 0 < 2\pi f_0 t < d\pi, \\ \text{OFF}, & d\pi < 2\pi f_0 t < 2\pi. \end{cases} \quad (6.1)$$

Typically, the PA switch is driven by a square wave with $d = 1$ (50% duty cycle). The level of violation of ZVS and ZSS, respectively, are indicated by α and β as in [115]

$$v_c\left(\frac{1}{f_0}\right) = \alpha V_{\text{DD}}, \quad \frac{dv_c}{dt}\left(\frac{1}{f_0}\right) = 2\pi\beta f_0 V_{\text{DD}}, \quad (6.2)$$

where V_{DD} is the PA supply voltage.

Acar [115, 133–135] formulated relationships between class-E PA behavioral parameters and component parameters using the so-called K-design set, shown in Table 6.1.

Table 6.1: K-design set

$K_L = \frac{2\pi L f_0}{R}$	$K_C = 2\pi f_0 R C$	$K_X = \frac{X}{R}$	$K_P = \frac{R P_{\text{out}}}{V_{\text{DD}}^2}$
------------------------------	----------------------	---------------------	--

The K-design set parameters depend on α , β , the relative resonance frequency q , and the technology-dependent relative switch-on resistance, m , which is a function solely of the operating frequency, f_0 , and the technology-specific switch transistor time constant $R_{\text{ON}}C$, where R_{ON} is the switch on-resistance and C is the parasitic switch capacitance. The q and m parameters are defined as

$$q = \frac{1}{2\pi f_0 \sqrt{LC}}, \quad (6.3)$$

$$m = 2\pi f_0 R_{\text{ON}}C. \quad (6.4)$$

Load-pull contours for various amplifier metrics can be derived for a class-E PA designed for specific q , d and α and β [40]. To perform load-pull analyses, the PA load Z , is varied over a range of mismatch conditions. The resulting contours are shown in Smith charts normalized to the nominal load, $Z = R_{\text{nom}}$. For each load condition, PA metrics such as switch voltage, switch current, efficiency and output power can be derived. A full mathematical derivation of the load-pull analysis was presented in [40] and will not be repeated here. The load-pull contours show the peak switch voltage normalized to V_{DD} , efficiency and the average switch current and output power normalized to those under nominal load and design conditions ($Z = R_{\text{nom}}$, $\text{VSWR}=1:1$, $q = q_{\text{nom}}$ and $d = d_{\text{nom}}$). For high PA output power, the q parameter is set to 1.4 [115]. The m parameter for a typical 65 nm CMOS in the low GHz range is approximately 0.05. The d parameter is set to 1 (50% duty cycle). The supply voltage is chosen as $V_{\text{DD}} = 1.2\text{V}$ to comply with typically available CMOS supply voltages.

6.3.2 Effects of load mismatch on class-E PA behavior

To perform a load-pull study on the class-E PA, the K-design set parameters as well as the performance (output power and efficiency) and reliability related parameters (maximum switch voltage and average switch current) are derived as a function of the fixed parameters q , d and m and the load-dependent parameters α and β . Under nominal load conditions

$$K_{L_{\text{nom}}} = K_{L(q,d,m,\alpha=0,\beta=0)} = \frac{2\pi f_0 L}{R}, \quad (6.5)$$

$$K_{X_{\text{nom}}} = K_{X(q,d,m,\alpha=0,\beta=0)} = \frac{X}{R}. \quad (6.6)$$

Under load mismatch conditions, the load impedance Z deviates from the nominal load R , giving

$$Z = kR + jk'R. \quad (6.7)$$

where $k > 0$ and k' are real numbers. Under nominal load conditions, $k = 1$ and $k' = 0$. Under non-nominal load conditions, ZVS and/or ZSS conditions are violated and the K-design set K_L and K_X can be written as

$$K_{L(q,d,m,\alpha,\beta)} = \frac{2\pi f_0 L}{\Re\{Z\}} = \frac{2\pi f_0 L}{kR}, \quad (6.8)$$

$$K_{X(q,d,m,\alpha,\beta)} = \frac{X + \Im\{Z\}}{\Re\{Z\}} = \frac{X + k'R}{kR}, \quad (6.9)$$

which can be related to the nominal K-design set values by

$$K_L(q, d, m, \alpha, \beta) = \frac{K_{L_{\text{nom}}}}{k}, \quad (6.10)$$

$$K_X(q, d, m, \alpha, \beta) = \frac{K_{X_{\text{nom}}}}{k} + \frac{k'}{k}. \quad (6.11)$$

For any mismatch (k, k') , the switching parameters α and β can be found from (6.10) and (6.11) using a numerical solver. Once the load-dependent switching parameters α and β are obtained, the maximum switch voltage normalized to V_{DD} , average switch current normalized to that under nominal condition, output power normalized to that under nominal condition and efficiency follow.

Using this theory, developed in [40], a theoretical load pull analysis is performed on a class-E PA with parameters $q = 1.4$, $d = 1$, $m = 0.05$, $\alpha = 0$, $\beta = 0$. This design will henceforth be referred to as the nominal design. The resulting load-pull contours are shown in Figure 6.2. Inspection of the peak switch voltage load-pull contours reveals extreme behavior towards the upper left of the Smith chart, with peak switch voltages over $5.5 \times V_{DD}$. Likewise, the average switch current contours show an increasing trend towards the left side of the Smith chart, reaching over $3 \times I_{\text{nom}}$. These extreme peak switch voltages and average switch currents are accompanied by an increase in output power and a reduction in drain efficiency. When the load conditions shift towards the lower right of the Smith chart, high efficiency operation is maintained, but output power is degraded severely, reaching near-zero values. Because of the rapidly destructive nature of over-voltage-stress related oxide breakdown, relative to the gradual degrading effects of over-current, excessive switch peak voltage and the reduction thereof are the primary focus of this work.

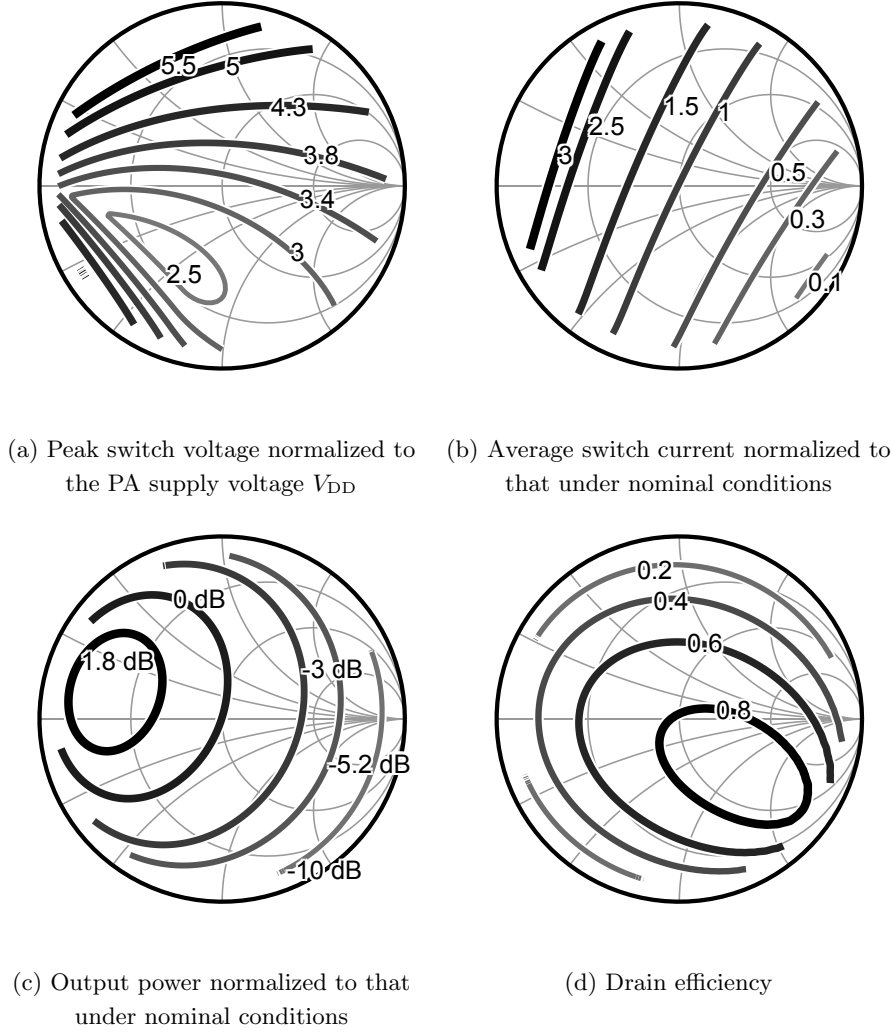


Figure 6.2: Theoretical class-E PA load-pull contours for $q = 1.4$, $d = 1$, $m = 0.05$, $\alpha_{\text{nom}} = 0$ and $\beta_{\text{nom}} = 0$

6.4 Second-order Effects

To obtain analytical results, the theory in [40] relies on an idealized switch model that has a finite R_{ON} , infinite R_{OFF} and instantaneous switching behavior. In practice, several second-order effects influence PA behavior. One such effect plays a role for highly negative switch voltages (highly negative α), which occur toward the upper left of the Smith chart in the theoretical load-pull contours [40]. In practice, these negative voltages are clamped due to reverse conduction of the switch transistor. This clamping leads to a reduction in switch voltage as compared to the theory due to the energy loss associated with this clamping action. Secondly, the m parameter varies under load mismatch due to the voltage-dependent switch transistor R_{ON} . This effect reduces the extreme switch currents. Another effect is the loss due to finite feed inductor Q , reducing PA efficiency. Additionally, losses in the matching network, output filter and interconnects reduce the impact of load mismatch on the PA, reducing extreme behavior. Lastly, the finite loaded Q of the output filter can result in significant transmission of energy at harmonic overtones, impacting PA performance. The main influence of the second order effects on the simulated and measured contours are warping and scaling with respect to the theoretical contours. A detailed discussion of these second-order effects and their impact on PA behavior is outside the scope of this chapter, but can be found in [40].

6.5 Simulation Results

As intermediate step between theoretical results and measurement results, load-pull simulations are performed on a class-E PA design using Cadence Spectre. The demonstrator PA is designed for $q = 1.4$, $d = 1$, $\alpha = 0$ and $\beta = 0$, $V_{\text{DD}} = 1.2 \text{ V}$, $f_0 = 1.4 \text{ GHz}$ and $P_{\text{out}} = 17.5 \text{ dBm}$. The switch consists of a 1.2 V thin-oxide MOS transistor ($W/L = 0.84 \text{ mm}/60 \text{ nm}$) cascoded by a 2.5 V thick-oxide MOS transistor ($W/L = 1.65 \text{ mm}/280 \text{ nm}$) with its gate biased to 1.8 V [22]. The PA component values shown in Table 6.2 were derived using the K-design set [115].

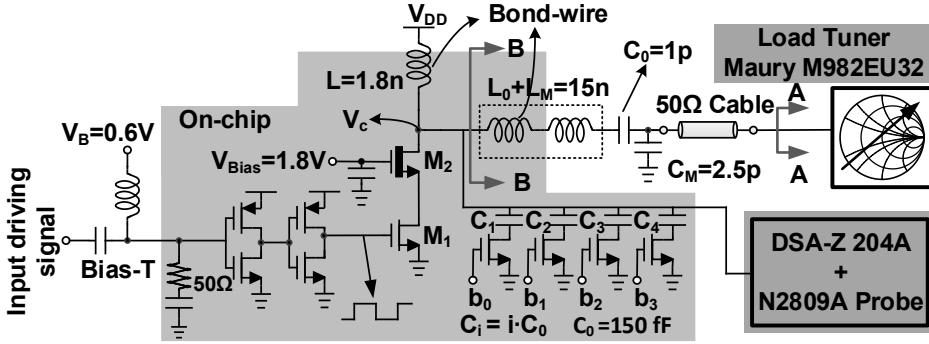


Figure 6.3: Schematic representation of the class-E PA. On-chip components are shown in the light-grey area, measurement-related information is contained in dark-grey areas. Modified from [119]. The chip micrograph and PCB setup of this PA, as used for the measurements in Section VI are shown in Figure 6.4.

Table 6.2: PA parameters

L	C	X	R	P_{out}
1.8 nH	3.4 pF	$j0 \Omega$	25 Ω	17.5 dBm

The schematic of the PA is shown in Figure 6.3. The matching network is lossless, the feed inductor has a quality factor $Q \approx 25$ and the loaded quality of the series filter is $Q_L \approx 5$.

The design of the switch allows a maximum switch voltage of 4.6 V, or $3.8 \times V_{\text{DD}}$ ($1.8 \text{ V} + 1.1 \times 2.5 \text{ V}$, including a 10% voltage margin). The focus of this work is on preventing oxide-breakdown due to high peak switch voltages and the reduction/prevention of hot-carrier degradation that may occur when ZVS conditions are severely violated. A dead-zone of $\Delta V_c = 0.2 \text{ V}$ was added to the algorithm to decrease noise sensitivity. At startup, the algorithm fully enables the SCB to ensure a safe starting condition for the PA. It then checks the peak switch voltage, $V_{c, \text{max}}$, lowering the SCB state while $V_{c, \text{max}} < V_{c, \text{nom}}$ and $C_{\text{bank}} > 0 \text{ fF}$, where $V_{c, \text{nom}}$ is

Simulated contours for this PA are shown in Figure 6.5; the contours are scaled and warped version of the theoretical contours in Figure 6.2 due to the second-order effects discussed in Section IV. Excluding the region of the load-

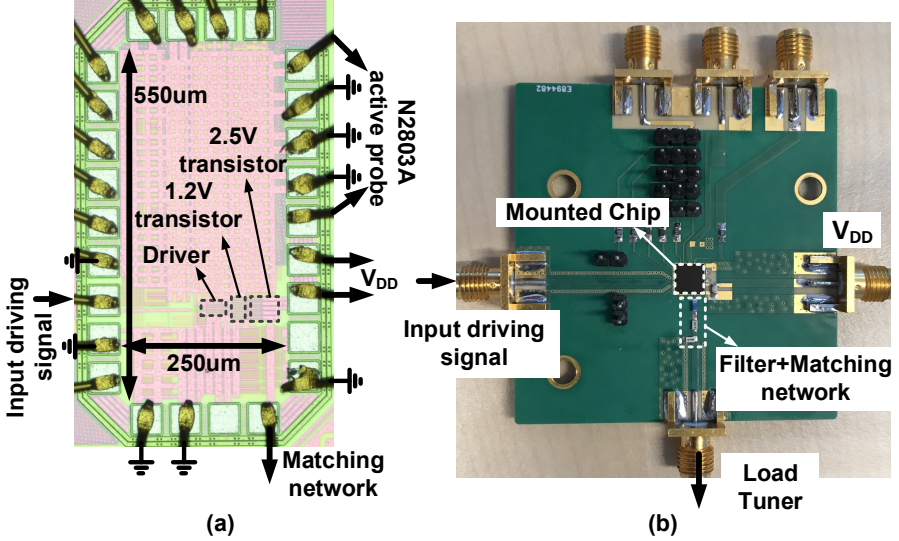
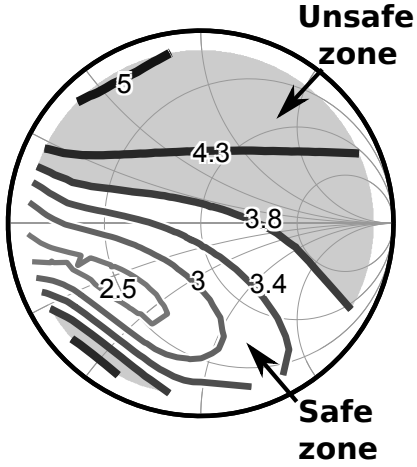


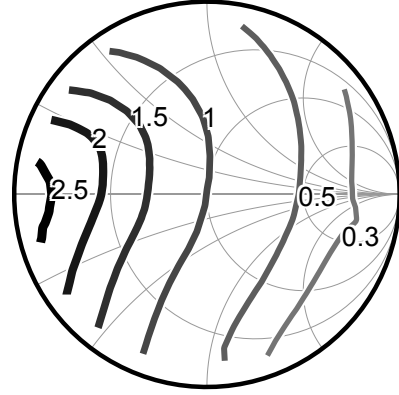
Figure 6.4: (a) Chip photomicrograph showing external connections and on-chip components [119] (b) PCB showing external connections and filtering + matching network [119]

pull plot in Figure 6.5a where the switch voltage exceeds $3.8 \times V_{DD}$ yields a Safe Operating Area (SOA). Figure 6.5b shows that a PA which has its switch designed to handle an average switch current slightly over $2.5\times$ that under nominal conditions sees no average switch current-related SOA reduction from the effects of load mismatch. The switch used in simulation and measurements meets this criterium.

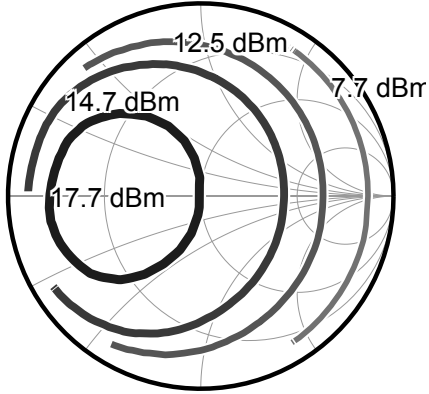
Figure 6.6 shows switch voltage waveforms for some load-mismatch conditions. The switch (oxide) breakdown limit ($3.8 \times V_{DD}$) is indicated by a dashed line. A violation of the breakdown limits can be observed for three of the four shown load conditions. The switch voltage waveform shown in Figure 6.6c exhibits high switch voltages at the switching moment, indicating the possibility of Channel Hot Carrier (CHC) degradation for load mismatches in the lower left region of the Smith chart.



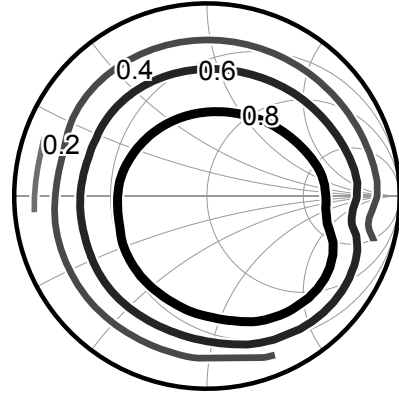
(a) Peak switch voltage normalized to the PA supply voltage V_{DD}



(b) Average switch current normalized to that under nominal conditions



(c) Output power



(d) Drain efficiency

Figure 6.5: Simulated class-E PA load-pull contours for $q = 1.4$ and $d = 1$

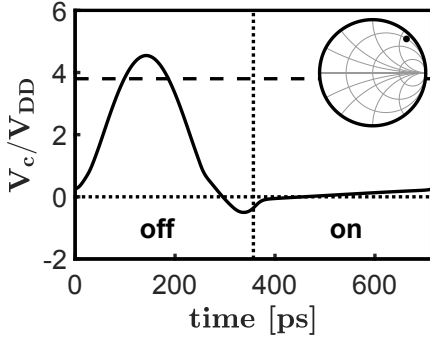
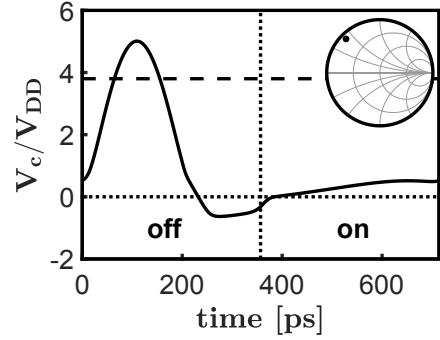
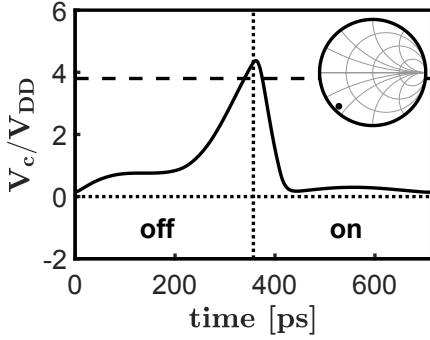
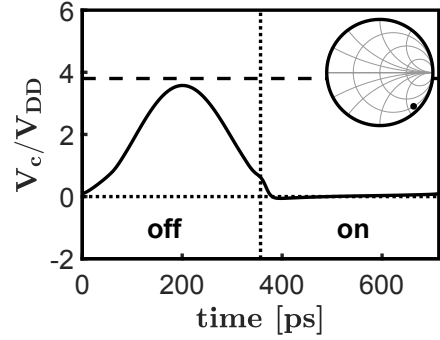
(a) Switch voltage waveform under load mismatch $\Gamma = 0.9\angle 45^\circ$ (b) Switch voltage waveform under load mismatch $\Gamma = 0.9\angle 135^\circ$ (c) Switch voltage waveform under load mismatch $\Gamma = 0.9\angle -135^\circ$ (d) Switch voltage waveform under load mismatch $\Gamma = 0.9\angle -45^\circ$

Figure 6.6: Simulated nominal PA switch voltage waveforms for several load mismatch conditions. The switching moment is indicated by the vertical dotted line.

6.6 Effects of the q and d parameters on PA behavior

In [93], the theoretical effects of varying the class-E PA q and d parameters were presented. The theory shows that, among other things, peak switch voltages occurring under load mismatch can be reduced by decreasing the q parameter or by increasing the d parameter. This behavior is illustrated using the theoretical load-pull analyses in the next subsections.

6.6.1 Effects of the q parameter on PA load-pull contours

Figure 6.7 shows the effects of changing the q from the original value of 1.4 to 1.15. Apparent is the receding of extreme peak switch voltage behavior, resulting in an increased SOA. Interestingly, the average switch current, output power and efficiency contours are virtually unaffected aside from a counter-clockwise rotation. The rotation of the efficiency contours is of special interest, as it implies that an increase in the effective high-efficiency operating area can be achieved by appropriate tuning of the q parameter.

The extension of the SOA by reduction of the q parameter opens the door to a self-protecting class-E PA system, as was demonstrated in [119]. Increasing the q parameter leads to a reduction of the SOA, and is thus not of interest for this work. In addition, a reduction of the q parameter would require a reduction of the switch tank capacitance, requiring down-scaling of the switch transistor. This necessarily leads to a higher switch R_{ON} and thus degraded PA performance [40].

6.6.2 Effects of the d parameter on PA load-pull contours

In addition to showing the effects of the q parameter, the work in [93] also showed that the d parameter can be used to influence PA behavior. This is illustrated using theoretical load-pull contours for a significantly increased d parameter.

Figure 6.8 shows the contours resulting from a change of the d parameter from 1 to 0.6. The resultant contours display a clockwise rotation with respect to the nominal load-pull contours. Notably, the (unshaded) SOA now covers the area in the lower left of the Smith chart that was not safe in the nominal case for $q = 1.4$ and $d = 1$.

The change in PA behavior due to a change in the d parameter is shown to be complementary to a similar change in the q parameter. As decreasing q advances the SOA towards the upper left of the Smith chart, a complementary change (increase) in d thus similarly extends the SOA. The results show that the unsafe area in the upper left of the Smith chart is the main region limiting PA SOA, which is decreased by both a decrease in q and an increase in d . This suggests a combination of the two approaches would permit a larger increase in SOA than either alone. Fortunately, the reverse switch conduction

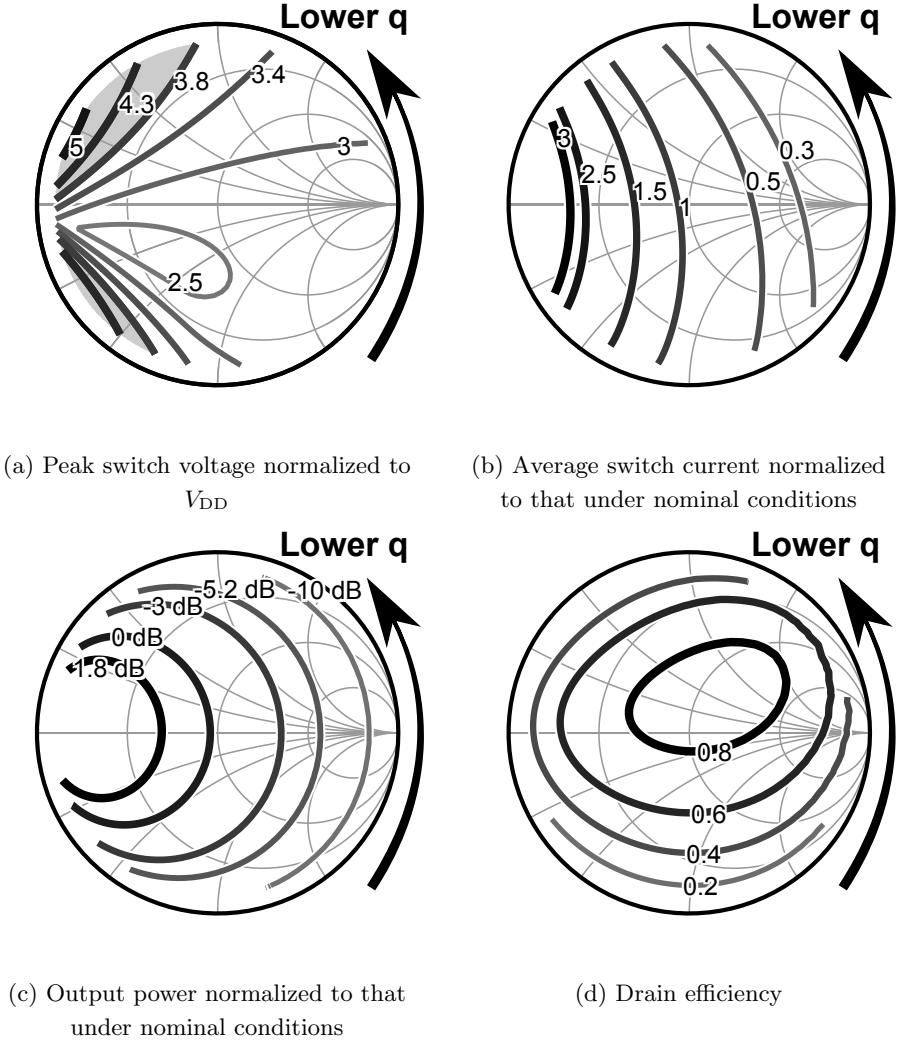


Figure 6.7: Theoretical load-pull contours for $q = 1.15$ and $d = 1$. Contour rotation due to reduction of the relative resonance frequency is illustrated.

discussed in section III effectively implements an increase in switch on-time, thereby virtually increasing the d parameter, which results in an extra counter-clockwise contour rotation for the associated load impedances. In this way, d tuning is automatically implemented for load conditions in the main unsafe area on the Smith chart. This automatic d tuning is the reason the SOA in Figure 6.5 is larger than predicted by the theory in Figure 6.2. The effect of

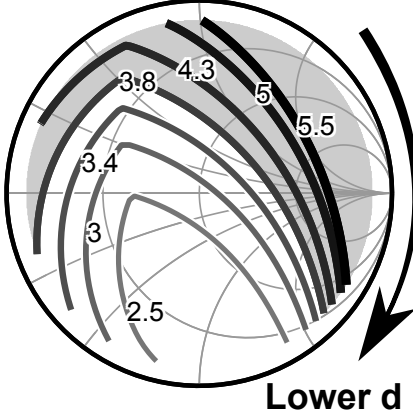
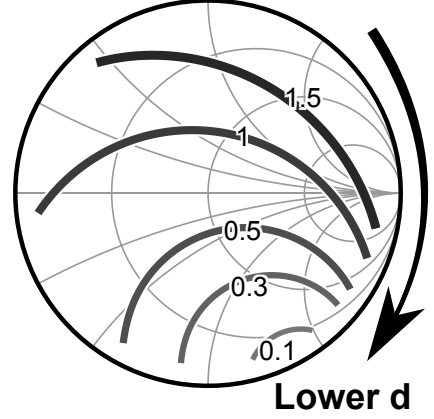
reverse switch conditions can be seen in the clamping behavior exhibited in e.g. Figure 6.6b.

6.7 Measurements

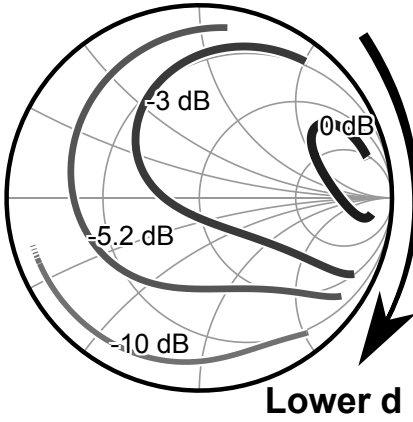
A class-E PA chip was developed in 65 nm for the work in [93]; some (component) values of this PA are shown in Table 6.2. The design and implementation of the class-E PA are shown in Figure 6.3 and Figure 6.4, respectively. The square-wave drive signal is produced on-chip by a cascaded pair of inverters. The first inverter input is biased using a bias-T to allow tuning of the switch drive signal duty cycle. The default switch tank capacitor is formed by the parasitic switch transistor capacitances.

In Section VI, the effects of varying the class-E PA q and d parameters were described. It was shown that the PA SOA can be rotated on the Smith chart by tuning either the relative (switch tank) resonance frequency, the switch duty cycle, or both. Because tuning the switch tank inductance is impractical, an increase in the q parameter is achieved by variably increasing the switch tank capacitance. This variable capacitance is implemented by a Switched-Capacitor Bank (SCB) with 4 control bits, utilizing 2.5 V thick-oxide switch transistors. These switch transistors are dimensioned to limit their maximum voltage stress to below 3 V. The residual capacitance the SCB presents to the switch node when it is in the off-state is compensated for by reducing the main switch size, lowering efficiency by less than 2% under nominal load conditions. The SCB switched capacitor bank utilizes four switches, switching 150 fF, 300 fF, 450 fF and 600 fF, respectively, for a total capacitance $C_{\text{SCB}} = 1500$ fF. This additional capacitance allows tuning of the q parameter from approximately $q = 1.4$ to $q = 1.15$ for a fully-disabled and fully-enabled SCB, respectively.

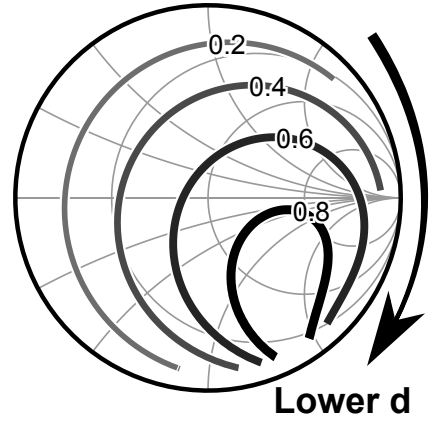
To verify the theory and simulations, a measurement setup was built using a Maury load tuner to detune the load and an 80 GSa/s oscilloscope with an Agilent active probe to capture the switch voltage waveform $V_c(t)$, as depicted in Figure 6.3. Additionally, the output power and power supply voltage and current are recorded. The load is pulled over the entire VSWR 19:1 range available from the Maury load tuner, in 196 steps, scanning at $|\Gamma| = \{0, 0.1, 0.3, 0.5, 0.7, 0.9\}$. In order to prevent destruction of the class-E

(a) Peak switch voltage normalized to V_{DD} 

(b) Average switch current normalized to that under nominal conditions

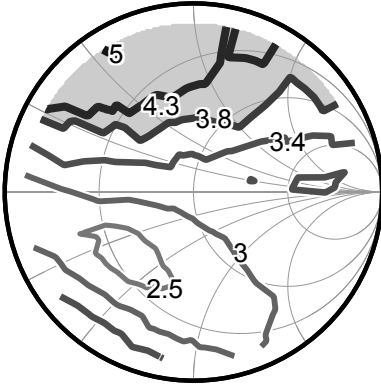


(c) Output power normalized to that under nominal conditions

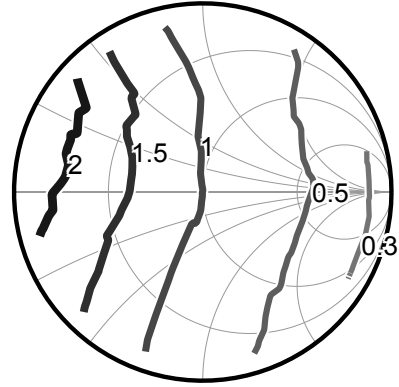


(d) Drain efficiency

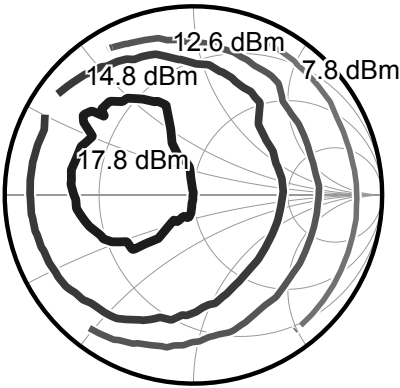
Figure 6.8: Theoretical load-pull contours for $q = 1.4$ and $d = 0.6$. Contour rotation due to reduction of the switch duty cycle is illustrated.



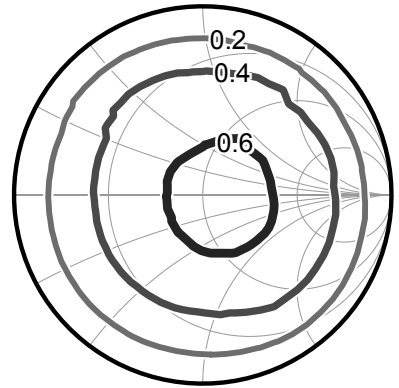
(a) Peak switch voltage normalized to V_{DD}



(b) Average switch current normalized to that under nominal conditions



(c) Output power

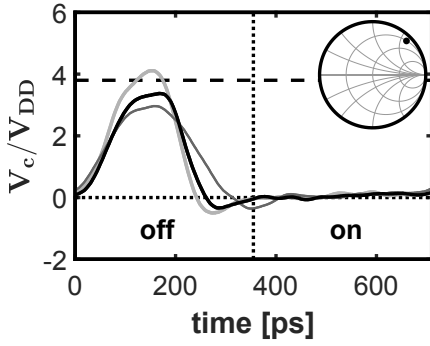


(d) Drain efficiency

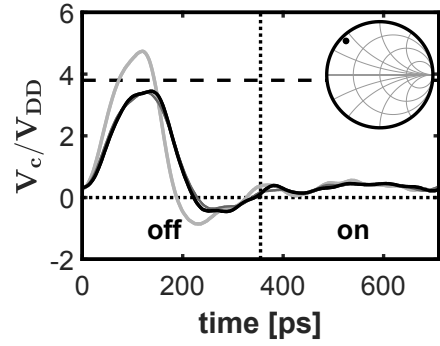
Figure 6.9: Measured load-pull data of the PA optimized for operation for the nominal load (center of the Smith chart); the frequency of operation is 1.4 GHz.

PA under test, the supply voltage V_{DD} is scaled down to keep the peak switch voltage below the switch breakdown limit. The data is scaled back to the nominal $V_{DD} = 1.2\text{ V}$, which does not compromise data accuracy. Phase shifts due to the matching network and interconnects were de-embedded.

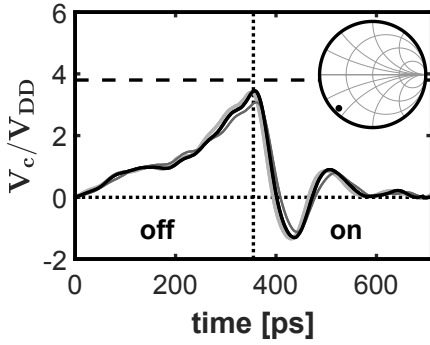
Figure 6.9 shows the load-pull contours obtained for the PA with $q = 1.4$ and $d = 1$. A good match with the simulation results in Figure 6.5 can be



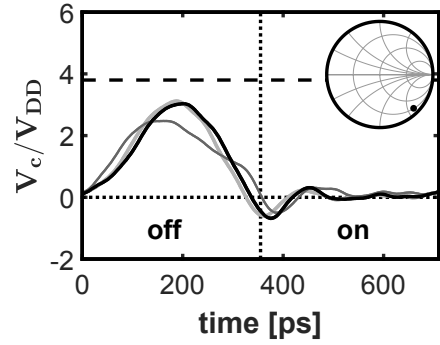
(a) Switch voltage waveform under load mismatch $\Gamma = 0.9\angle 45^\circ$



(b) Switch voltage waveform under load mismatch $\Gamma = 0.9\angle 135^\circ$



(c) Switch voltage waveform under load mismatch $\Gamma = 0.9\angle -135^\circ$



(d) Switch voltage waveform under load mismatch $\Gamma = 0.9\angle -45^\circ$

Figure 6.10: Measured PA switch voltage waveforms for $q = 1.4$ (thick light grey) $q = 1.15$ (thin medium grey) and with the self-protecting loop enabled (thick black) for several load mismatch conditions. The switching moment is indicated by the vertical dotted line.

observed.

In Figure 6.10, measured switch voltage waveforms normalized to V_{DD} are shown for the same load-mismatch conditions as used for the simulated results in Figure 6.6, showing good correspondence between measurement and simulation.

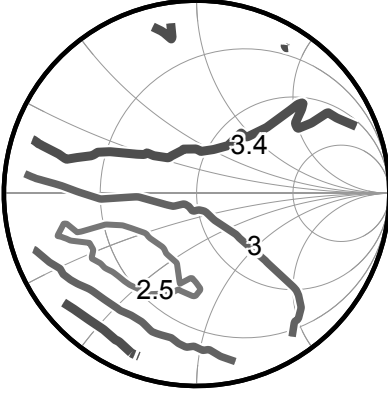
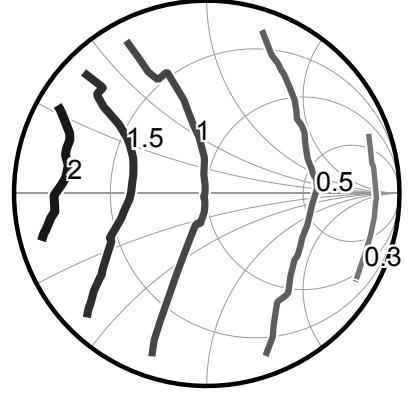
6.8 Self-healing system

Using the q -tuning technique previously discussed and demonstrated, a demonstrator self-healing PA system was constructed. For this, the setup used to gather the measurement data in Section VI is complemented by a control loop implementing the algorithm shown in Figure 6.12. The oscilloscope continuously monitors the switch voltage waveform $V_c(t)$ and extracts its peak value, which is input to the self-protecting algorithm. In our demonstrator setup, this computationally light algorithm was executed on the measurement data processing PC.

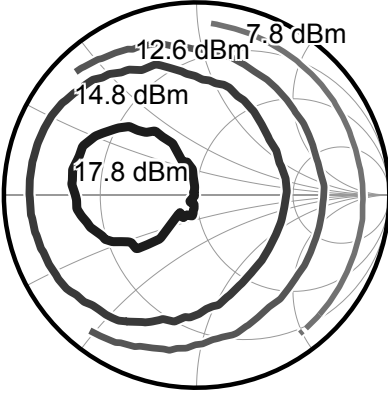
A dead-zone of $\Delta V_c = 0.2$ V was added to the algorithm to decrease noise sensitivity. At startup, the algorithm fully enables the SCB to ensure a safe starting condition for the PA. It then checks the peak switch voltage $V_{c, \max}$, lowering the SCB state while $V_{c, \max} < V_{c, \text{nom}}$ and $C_{\text{bank}} > 0$ fF, where $V_{c, \text{nom}}$ is the peak switch voltage under nominal conditions. If the peak switch voltage increases above $V_{c, \text{nom}} + \Delta V = 4.2$ V, the SCB state is incremented until the peak switch voltage drops below this level or the SCB is at the maximum state. If, in the latter case, the switch voltage is above the 4.6 V switch transistor breakdown limit, the algorithm reports that it cannot heal the PA. The algorithm runs continuously to ensure safe PA operation.

Figure 6.11 shows the measured load-pull contours for the self-healing class-E PA system, operating at 1.4 GHz. Note that the unshaded SOA covers the entire VSWR 19:1 range, proving experimentally that our self-protecting class-E PA system is reliable under load mismatch conditions exceeding those presented by antenna loads. As predicted by both theory and simulation, efficiency and output power are not significantly effected by the self-healing system, with a worst case degradation in output power of -1.6 dB and a worst case absolute efficiency decrease of 6%.

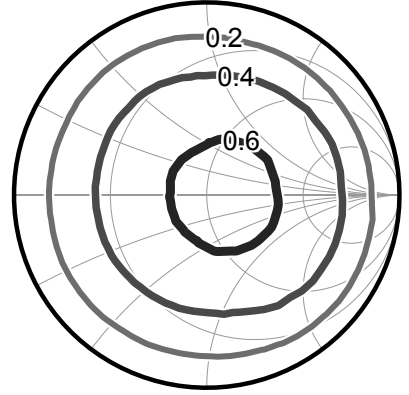
Because the self-protecting system requires only information about the peak switch voltage, only needs to track (low-frequency) load-impedance variations and involves the checking of simple conditions, the computational power and hence the power consumption of an on-chip implementation would be negligibly small relative to PA power consumption.

(a) Peak switch voltage normalized to V_{DD} 

(b) Average switch current normalized to the nominal case



(c) Output power



(d) Drain efficiency

Figure 6.11: Measured load-pull data of the self-healing system

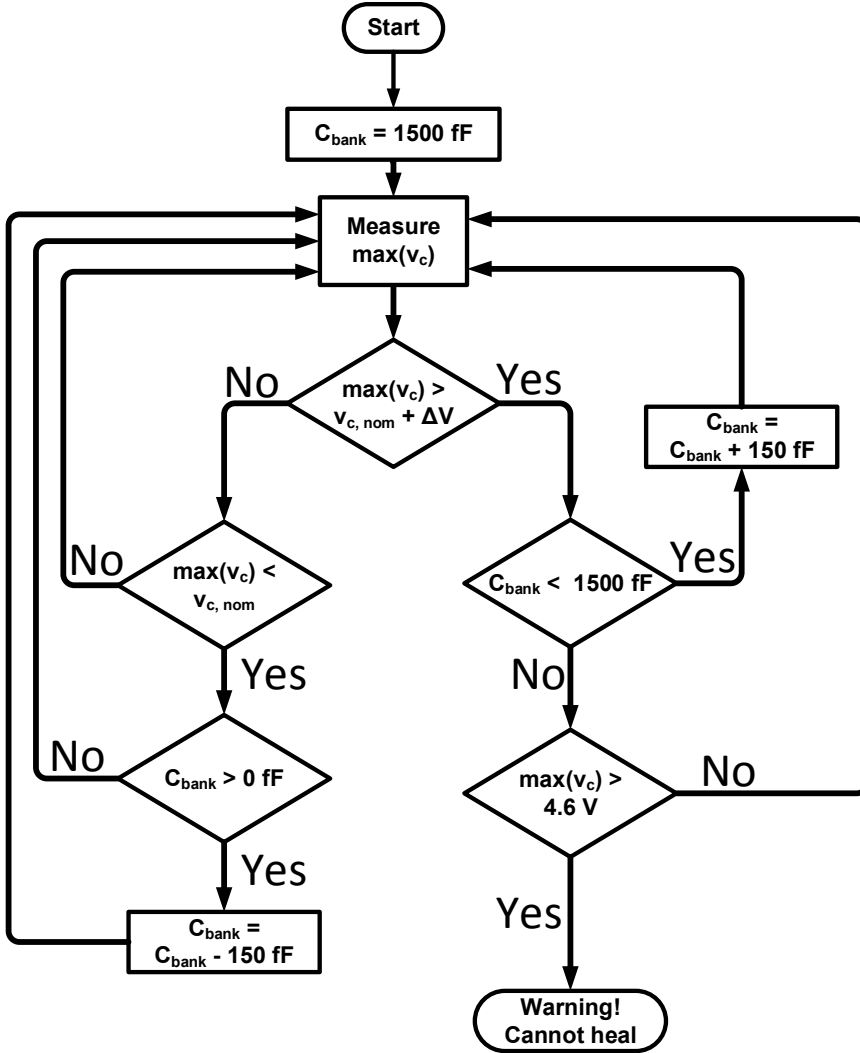


Figure 6.12: Demonstrator algorithm flow chart. Modified from [119]. The algorithm starts by ensuring PA safety by fully enabling the SCB. It then measures the peak switch voltage, based on which it increments or decrements the SCB state to attempt to return the PA back to nominal operation conditions. If the SCB is at the maximum state and the switch breakdown voltage limit is exceeded, an error is reported to the user.

6.9 Conclusion

Class-E PAs may encounter severe and destructive reliability degradation under load mismatch conditions when not including significant design margins, especially for (over-)voltage. This work showed, both experimentally and theoretically, the effects of such load mismatch conditions on a number of relevant PA parameters. It was shown that high peak switch voltages present the main danger to reliability. The effects of the relative resonance frequency of the tank, q , and the switch duty cycle, d , on class-E PA behavior were demonstrated, showing that while either can be used to increase the Safe Operating Area (SOA), the q parameter has a stronger influence. A tuning technique for reducing the peak switch voltage under load mismatch conditions based on tuning the q parameter was implemented alongside a class-E PA on a 65 nm CMOS chip by means of a switched capacitor bank. It was shown that in addition to the implemented controllable q tuning, virtual switch duty cycle tuning occurs under load conditions with large negative switch voltages. Using the proposed tuning technique, a class-E PA was augmented with a self-protecting system utilizing a simple tuning algorithm to automatically tune the PA by varying the SCB capacitance to obtain reliable operation under previously disastrous load mismatch conditions. Our tuning technique extends the SOA of the class-E PA up to VSWRs of 19:1. This demonstrates that our self-protecting class-E PA system can operate reliably with a large safety margin under the typical VSWR 10:1 load-mismatch conditions presented by an antenna. The self-protecting system has a low impact on output power and efficiency, with these metrics seeing a worst-case degradation of -1.6 dB and 6%, respectively.

Chapter 7

Preserving Polar Modulated Class-E Power Amplifier Linearity under Load Mismatch

7.1 Introduction

Modern wireless communication devices use high-order complex modulation schemes like 1024 QAM¹. These signals have a high peak to average power ratio (PAPR) and impose stringent linearity requirements on the power amplifiers (PAs). Given the large share of power consumed by the PAs in a communication system, highly efficient switched-mode PAs are attractive. However, due to inherent efficiency-linearity trade-offs [18], digital predistortion (DPD) becomes necessary for these PAs to meet linearity requirements [136], [137] of increasing order complex modulation schemes.

The antenna impedance depends on the electromagnetic environment of the antenna and therefore vary over time [14]. In switched-mode PAs, load mismatch from the nominal $50\ \Omega$ load detunes the resonant network. For class-E PAs, this degrades the output power, efficiency, linearity and also jeopardizes

¹This chapter consists of material previously published during the 2020 IEEE Radio Frequency Integrated Circuits Symposium[76] and it is reformatted to a thesis form.

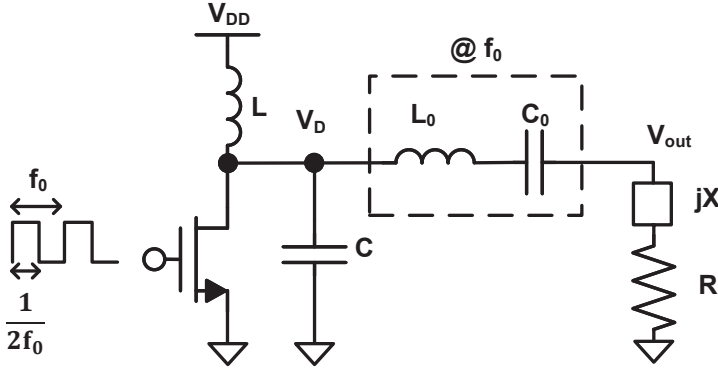


Figure 7.1: Schematic representation of a single-ended class-E PA.

the reliability [40]. For a *polar* class-E PA, this translates to variation in AM/AM and AM/PM characteristics, which renders $50\ \Omega$ optimized static DPD ineffective under load variation [138].

Previous works use various techniques to preserve PA linearity under load mismatch. These can be categorized into methods that keep the PA load impedance at its nominal value, and methods that deal with PA load variation. Implementations of the former methods are presented in [139], [140]. In [139], an adaptive tunable matching network (TMN) ensures the nominal load for the PA and thereby preserves linearity under antenna mismatch conditions. However, TMNs are lossy, bulky and hence not suitable for easy integration in ever-miniaturizing CMOS integrated circuits. A solution with similar disadvantages is the addition of circulators or isolators with the PA. In [140], a phase detector at the collector of the PA combined with a controlled phase shifter at the output are used. The increase in size and high driving voltage prevents the above approach from being practically integrated into the latest CMOS technology. Implementation of the latter method is described in [141], where a peak detector at the collector of the PA combined with an adaptive feedback control loop to tune the input drive signal is used. However, such a system improves linearity at the cost of transmitted power because it reduces the input drive level. Another way to deal with load-dependent non-linearity is to implement DPD for different loads and select the suitable DPD setting using load impedance estimation. For class-E PAs, to the best of the authors' knowledge, there is no work focusing on integrated adaptive linearity

improvement under severe load mismatch.

We present a proof-of-concept polar class-E PA with an integrated waveform characterizer, which allows the implementation of fully automated adaptive digital predistortion (ADPD) to preserve the linearity of a PA under load mismatch, aiming at 1024 QAM modulation.

In section 7.2, the linearity of polar class-E PA under load mismatch is discussed. In section 7.3, the principle of adaptive preservation of PA linearity with the integrated waveform characterizer and implementation of the system are discussed. The measurement results demonstrating the effectiveness of the system under load mismatch are presented in section 7.4. Conclusions are summarized in section 7.5.

7.2 Linearity of a polar class-E PA under load mismatch

Fig. 7.1 depicts a single-ended (non-polar) class-E PA where the MOSFET operates as a switch driven by a 50 % duty cycle square wave with a frequency f_0 . The LC tank shapes the switch's drain voltage waveform V_D , and the L_0C_0 resonant tank ensures that the output current is sinusoidal with frequency f_0 . A matching network (not in Fig. 7.1) transforms the antenna impedance to the PA's load impedance: $Z_L = R + jX$. Voltage V_D depends on both the real and imaginary parts of Z_L [40]. This Z_L -dependent switch voltage translates to Z_L -dependent magnitude and phase of the first harmonic of the output voltage signal of the class-E PA.

In communication systems, the PA must handle modulated signals. In this chapter, we aim at 1024 QAM. To deal with complex modulated signals, the class-E PA can be used in outphasing or polar configuration; we use the latter.

In polar modulated class-E PA, distortions are due to AM/AM and AM/PM conversions. AM/AM represents the non-linear relation between the modulated supply voltage V_{DD} and the amplitude of the output RF signal V_{out} . AM/PM is V_{DD} -dependent phase modulation of V_{out} . Any change in Z_L leads to a change in the class-E PA's switch voltage waveform and consequently leads to Z_L -dependent AM/AM and AM/PM characteristics. Other causes of AM/AM and AM/PM conversions in a polar class-E PA include feedthrough of the drive voltage of the switch via its relatively large gate-drain capacitance,

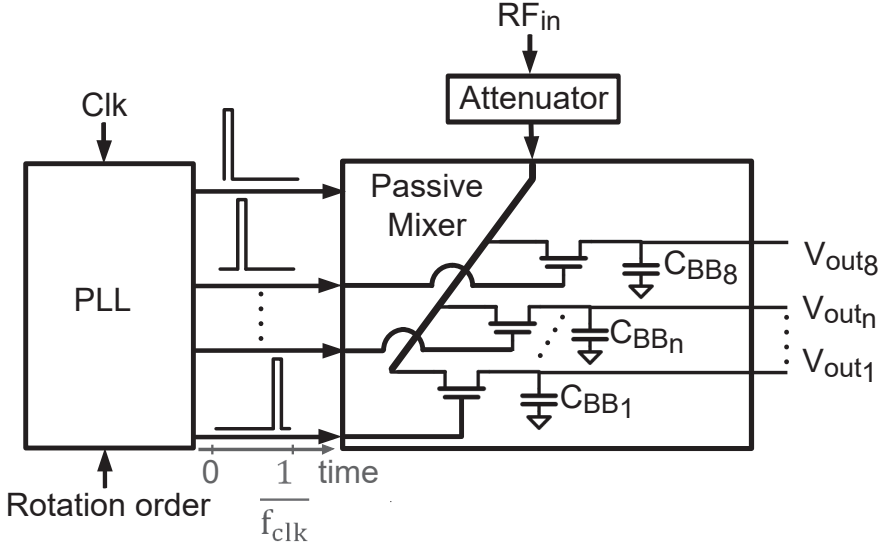


Figure 7.2: Block diagram of RF waveform characterizer.

non-zero on-resistance of the switch, and drain-bulk junction capacitance of the switch [36]. Note that the feedthrough signal is only phase modulated and hence has a wide bandwidth. Therefore, it leads to broadening of the output spectrum, increasing the adjacent channel power ratio (ACPR). The cascode PA topology minimizes the effect of the feedthrough signal.

7.3 Demonstration of ADPD with polar class-E PA

We present a polar class-E PA with an on-chip RF waveform characterizer that enables ADPD to correct AM/AM, AM/PM distortions, temperature changes and slow memory effects as the load changes.

7.3.1 Waveform Characterizer

The RF waveform characterizer is based on the work in [74]. Fig. 7.2 shows the block diagram of this waveform characterizer. It can measure up to three harmonics of an RF signal up to a fundamental frequency of 3 GHz. Hence, the waveform characterizer can be used for ADPD in PAs with operating frequencies up to 3 GHz; we target 2.4 GHz for demonstration. The char-

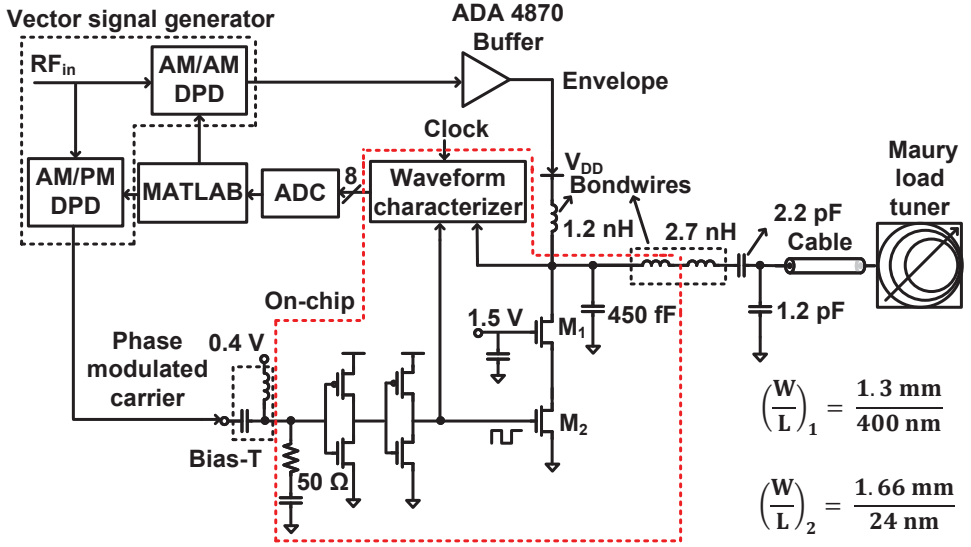


Figure 7.3: Schematic of the implemented polar class-E PA with ADPD using the integrated waveform characterizer.

acterizer mixes the RF waveform using an N-path approach and produces 8 quasi-DC samples per period of the RF waveform. These 8 samples are input to ADCs, the output of which is processed in a computer running MATLAB. The waveform characterizer uses the (unmodulated) carrier frequency as the clock signal: an extra clock is not required and the phase information of the measured signal can be obtained. An 8-point discrete fourier transform (DFT) is performed in MATLAB to get the magnitude and phase information of the sampled RF signal. In such systems, accuracy is generally limited by sample timing inaccuracies which in this case is mainly due to delay mismatch in a 4-stage differential inverter ring oscillator inside the phase-locked loop (PLL). To significantly enhance the accuracy of sampling, statistical properties of the delay mismatches are exploited to cancel the impact of delay spread [74]. The characterizer consumes 3 mW power under continuous operation at 2 GHz.

7.3.2 Adaptively Preserving PA Linearity

Fig. 7.3 presents the schematic of the polar modulated PA employing ADPD. For the ADPD, the input and output signal of the PA are required. The

transmitted data is known in a transmitter while the waveform characterizer samples the modulated data at the drain of the switch. The DFT yields magnitude and phase information of the first 3 harmonics in the drain voltage signal; the fundamental harmonic is used for ADPD. Magnitude and phase data are compared with the corresponding transmitted magnitude and phase data derived from IQ data transmitted by the vector signal generator (VSG) to generate AM/AM and AM/PM correction signals. For flexibility, signal processing is done on a computer running MATLAB. The correction signals are then input to the lookup table (LUT) based DPD inside the VSG. The VSG outputs the predistorted envelope and phase signals for the polar class-E PA. The loop is executed periodically making the PA linearity robust against any relatively slow process that impacts linearity.

The time constant of the waveform characterizer is $\tau = 16$ ns. For 40 dB accuracy, 5τ is required which makes the effective settling time of the characterizer 80 ns. Hence the maximum symbol rate measured by the waveform characterizer is 12.5 Msym/s. Transmitted and the sampled data are read from a mixed-signal scope in blocks. Reading one block takes 0.65 s; reading data from 8 channels requires 5.2 s. The bottleneck for effective sample rate in our demonstration is due to latency while reading data. Antenna environment changes on a time scale of ms [123]. Removing data latency bottleneck can reduce the response time of the complete system to order of ms making the system adapt to changes on a ms time scale such as temperature changes, slow memory effects [142] and antenna impedance variations.

7.3.3 Implementation

The chip includes a single-ended cascode class-E PA and the RF waveform characterizer fabricated in 22 nm FDSOI CMOS technology packaged in QFN 40; Fig. 7.4 shows the micro-photograph. The PA occupies 0.064 mm^2 area, and the waveform characterizer occupies 0.014 mm^2 area. The PA is designed for zero voltage switching and zero slope switching conditions at frequency $f_0 = 2.4$ GHz. The peak-power frequency is shifted to 2 GHz from the target 2.4 GHz, which may be due to the bondwires at the PA output. The component values for the designed PA are shown in Fig. 7.3. The 1.2 nH inductor is implemented using bondwires; the parasitic capacitance of the MOSFET is included in the 450 fF capacitor. Two cascaded inverters are used as switch

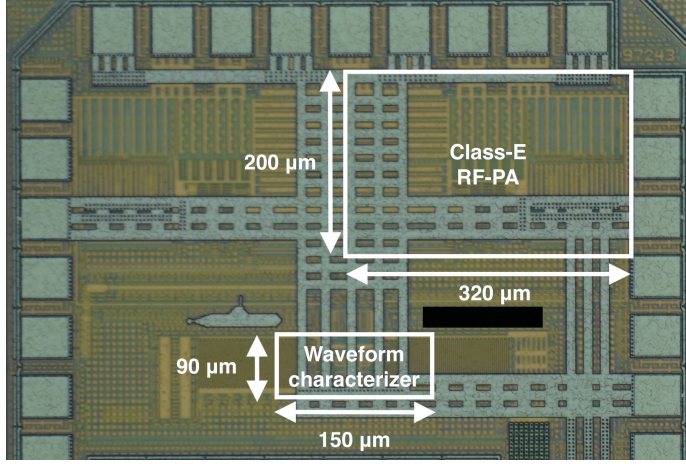


Figure 7.4: Chip microphotograph.

driver ensuring hard switching of the switch transistor. The input of the on-chip waveform characterizer is connected to the drain of switch and the outputs of the characterizer are fed to MATLAB through ADCs. The predistorted input signal is fed to the PA through an R&S SMW200A VSG. An ADA 4870 IC implements the envelope tracking buffer for the demonstrator.

7.4 Measurements

Single carrier modulated signal measurements are performed on the polar class-E PA to demonstrate linearity preservation using the presented ADPD under load mismatch. A 1024 QAM signal at 1 MSym/s symbol rate with pseudo-random bit sequence (PBRs) 23, pulse-shaped using root-raised cosine filter with a roll-off factor 0.35 and decomposed into the envelope and phase-modulated carrier at frequency 2 GHz are generated using the VSG. 400 symbols are used to construct AM/AM and AM/PM correction signals. Load-pulling is performed with a Maury load-pull tuner for voltage standing wave ratio (VSWR) up to 9:1. The PA is operated at 15 dB back-off for the nominal load condition to avoid breakdown during load-pull [40] while no class-E tuning for reliability [119] is done in this work to focus only on the linearity.

Fig. 7.5 (a), (b) show the normalized output symbol constellation and

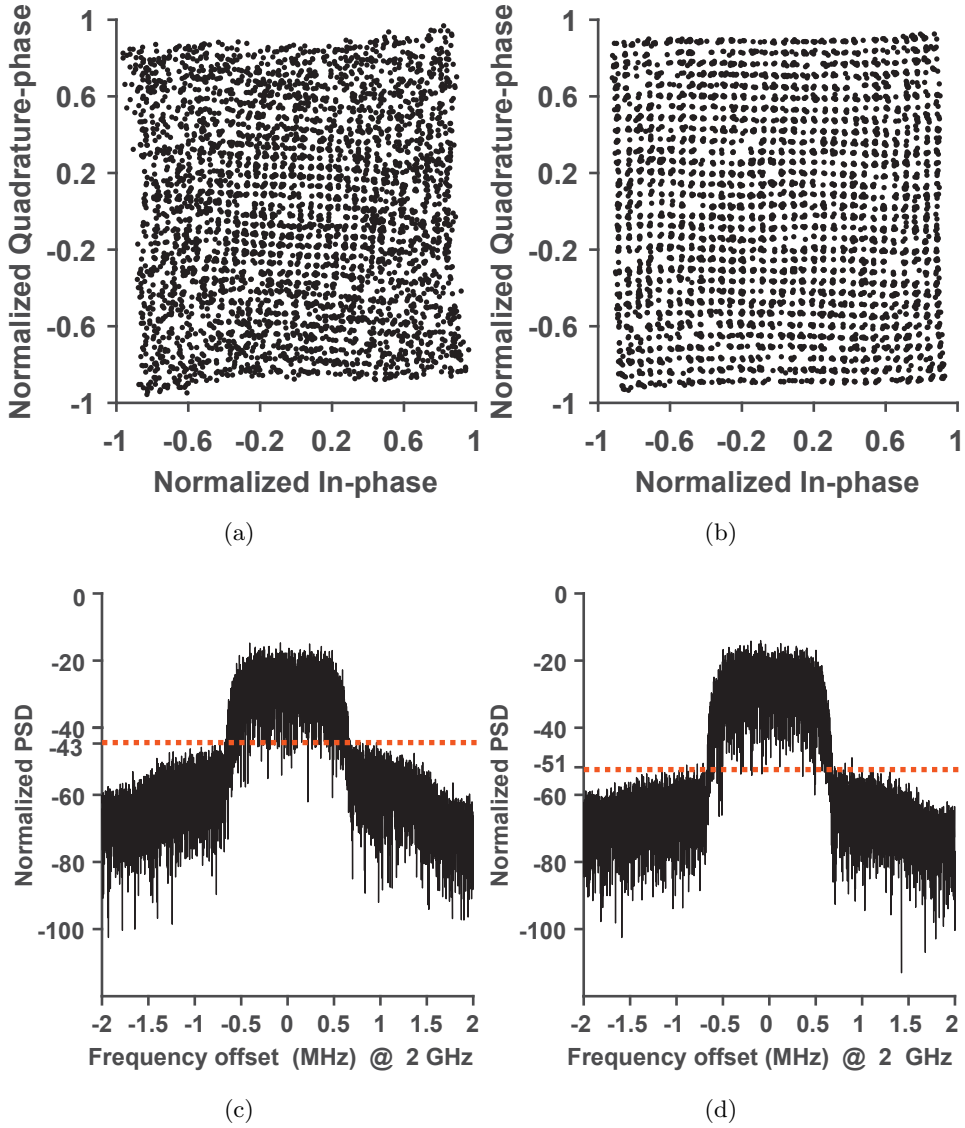


Figure 7.5: Measured performance for a 1 MHz 1024 QAM signal at 2 GHz at $50\ \Omega$ load. Normalized symbol constellation (a) before DPD, (b) after DPD. Normalized output power spectral density (c) before DPD, (d) after DPD.

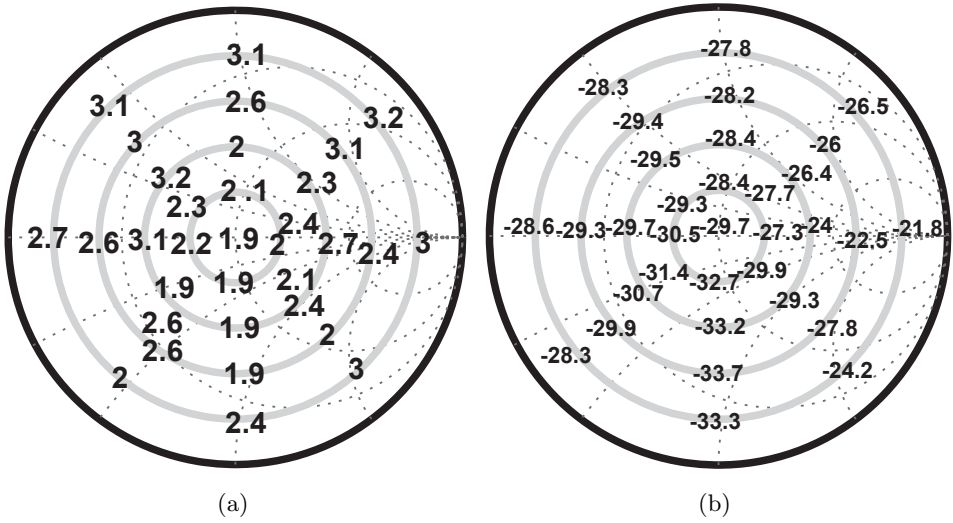


Figure 7.6: Load-pull measurements for VSWR up to 9:1 without DPD with a 1 MHz 1024 QAM signal at 2 GHz. (a) EVM (%), (b) ACPR (dB).

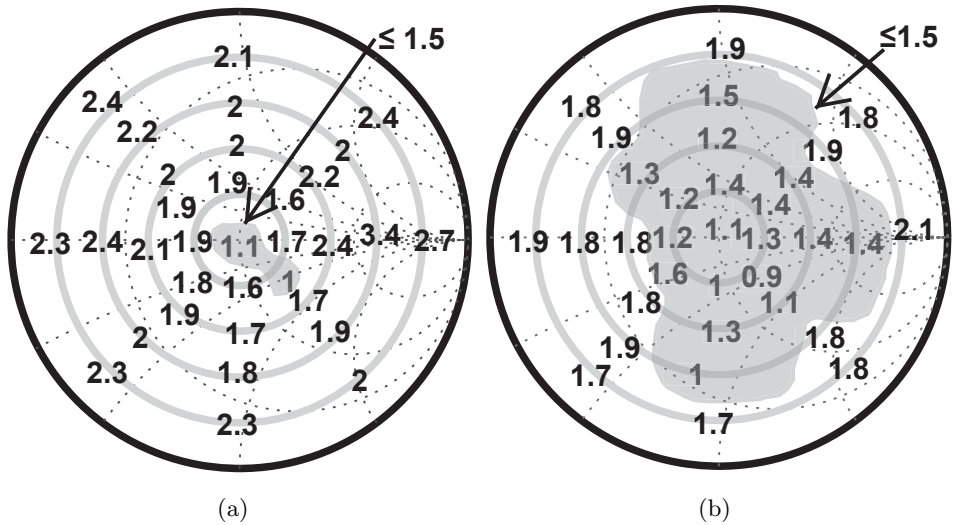


Figure 7.7: Load-pull measurements of EVM (%) for VSWR up to 9:1 with a 1 MHz 1024 QAM signal at 2 GHz. (a) after 50 Ω optimized static DPD, (b) after ADPD.

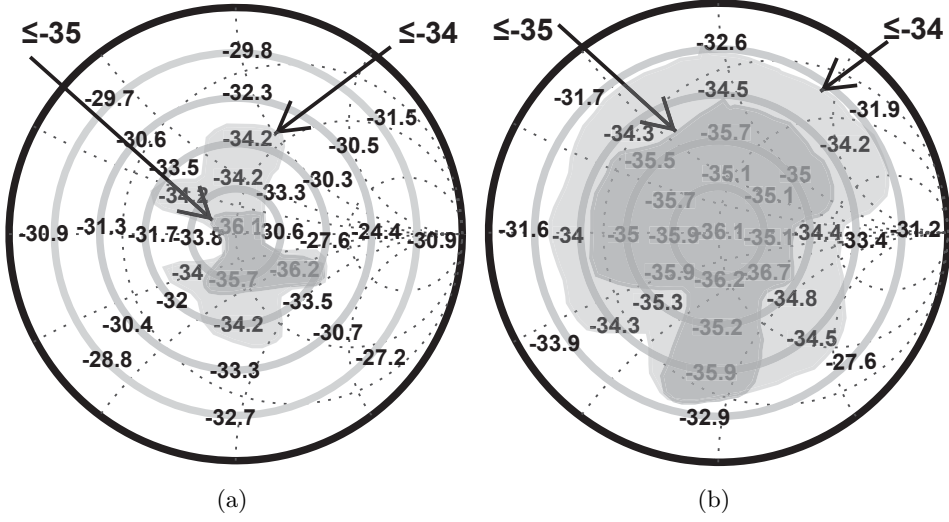


Figure 7.8: Load-pull measurements of ACPR (dB) for VSWR up to 9:1 with a 1 MHz 1024 QAM signal at 2 GHz. (a) after 50 Ω optimized static DPD, (b) after ADPD.

(c), (d) the normalized output power spectral density (PSD) before and after DPD, respectively at 50 Ω load. Fig. 7.6 (a) and (b) show the Smith charts of EVM (%) and ACPR (dB) of the polar class-E PA without any DPD. Fig. 7.7 (a) and (b) show Smith charts of EVM (%) up to VSWR 9:1 with 50 Ω optimized static DPD and with ADPD, respectively. The EVM is normalized to root mean squared (RMS) power. The EVM standard for 1024 QAM signal is considered 1.5 %. The load-pull Smith charts without DPD, with 50 Ω optimized static DPD and with ADPD include a shaded area for which EVM ≤ 1.5 %. A significant increase in area under the shaded region can be observed from no DPD to 50 Ω optimized static DPD to ADPD. Fig. 7.8 (a) and (b) show Smith charts of ACPR (dB) up to VSWR 9:1 with 50 Ω optimized static DPD and with ADPD, respectively. For ACPR calculation, the higher and lower adjacent channel bandwidth is considered to be 1 MHz each. The centers of adjacent channels are situated at an offset of ± 1.35 MHz from the carrier frequency. The ACPR Smith charts show the area covered for values ≤ -34 dB and ≤ -35 dB for all three cases: without DPD, with 50 Ω optimized static DPD and with ADPD. Similar to the Smith chart showing EVM, there is a significant increase in area under the shaded region for ACPR ≤ -34 dB and

ACPR \leq -35 dB from no DPD to 50 Ω optimized static DPD to ADPD.

7.5 Conclusion

The linearity of high-efficiency class-E PAs can be drastically compromised in the presence of load mismatch. We presented a single-ended polar class-E PA with an on-chip integrated waveform characterizer, in 22 nm FDSOI CMOS technology to implement ADPD. For VSWR up to 9:1 when the PA is excited with a 1 MHz 1024 QAM RF signal at 2 GHz, we showed that using our ADPD system sufficiently low EVM and ACPR values can be maintained across a relatively large area on the Smith chart compared to that when using a static (50 Ω optimized) DPD. The ADPD system can be used to optimize performance for relatively slow processes such as antenna load variation, temperature variation, and slow memory effects. This system allows practical application in next-generation mobile communication systems with complex modulation schemes that demand stringent linearity and are subjected to inevitable load mismatch.

Chapter 8

Summary and original contributions

This chapter summarizes this thesis and lists the original contributions.

8.1 Summary

The introduction of the internet of things resulted in an increase in the number of wireless devices, while simultaneously the number of wireless devices that require higher data rates also increased thus resulting in a congested frequency spectrum. Complex modulation schemes are used to enable higher data rates while occupying the same frequency spectrum, thus increasing the spectral efficiency. Complex modulation schemes come however at the cost of both higher linearity requirements of the RF-PA and a higher peak-to-average power ratio (PAPR) thus increasing the required energy to transmit a single bit.

The improvements in CMOS technology enabled the integration of full RF-transceivers on a single chip, reducing the overall cost of the transceiver. Designing RF-power amplifiers becomes more complicated due to using complex modulation schemes and the decreasing maximum (supply) voltages of modern CMOS technologies. Several techniques exist to increase both the output power of a CMOS RF-PA and its reliability.

Efficiency enhancement techniques such as outphasing and envelope elimination and restoration can increase the RF-PA efficiency. Additionally, both these techniques can be used in combination with switched-mode RF-PAs, al-

lowing a higher overall PA efficiency compared to that of linear RF-PAs. The class-E RF-PA is of special interest, since it can achieve relatively high output powers in a standard CMOS technology. However, class-E PAs are sensitive to load mismatch, which increases the maximum stress over the switch transistor and can even permanently damage or break the RF-PA. Depending on the load impedance of the class-E PA the maximum stress is caused by a high voltage or a high current.

Non-linearities in the RF-PA can cause spectral regrowth and intermodulation distortion. This results in an increased signal bandwidth and an overall lower SNR, decreasing the overall spectral efficiency and channel capacity. There are several techniques to linearise RF-PAs, however they all have their own drawbacks. Feedback topologies such as Cartesian feedback may exhibit stability issues, where feedforward topologies, such as predistortion, depend on exact compensation of unwanted components. In the case of digital predistortion (DPD), knowledge of the RF-PA's AM-AM and AM-PM characteristics are required. However, both AM-AM and AM-PM transfers depend on temperature, voltages and the load impedance and can thus vary from the DPD coefficients that are conventionally derived for a single operating point. To maintain DPD performance over these variations, information about the operating condition of the RF-PA can be used to adaptively tune the DPD coefficients, turning the feedforward (D)PD into a feedback (D)PD.

Enabling efficient and robust RF-PAs requires information about the operating points of the RF-PA, which can be acquired from the internal RF-waveforms in an RF-PA. Chapter 4 introduces N-path circuits as a RF-waveform characterizer, efficiently down-converting the RF-waveform to quasi-DC voltages. In case of an 8-path circuit, the DC voltage and the first three (complex) vectors corresponding to the first three harmonics of the RF-waveform can be obtained by performing a discrete Fourier transform (DFT) on the set of quasi-DC voltages. When using a DFT, it is assumed that these quasi-DC voltages are (ideally) equally spaced over a single period of the RF-carrier frequency. However, mismatch between the phases in the N-path circuit degrade the accuracy of the RF-waveform estimation; this mismatch is primarily caused by delay cell mismatch. Rotating the N delay elements inside the delay line N times yields after averaging ideal sampling moments. This technique increases the measurement accuracy by up to 20 dB at the cost of only a small area and

power overhead.

Chapter 5 presents an algorithm that can resolve frequency ambiguity for signals with an orthogonal frequency basis, such as used in most modern complex modulation schemes. The algorithm uses two samplers clocked at non-integer multiple sampling rates, resulting in distinct aliasing patterns. These aliasing patterns can be described by distinct sets of linear equations. Combining the two sets of linear equations increases the overall rank of the linear system, allowing the algorithm to resolve frequency ambiguity. Furthermore, the algorithm allows aggregated bandwidths close to the Nyquist-Shannon limit, while being able to reconstruct signals from multiple Nyquist zones. The proposed algorithm can be used to increase the number of harmonics the RF-waveform characterizer can measure. Changing the number of delay elements (and thus the number of samples per period) in the RF-waveform characterizer results in a different sample rate and thus a distinct aliasing pattern. Using the proposed algorithm together with measurements of the RF-waveform characterizer where a different number of delay elements are used increase the number of characterizable harmonics. This improves the measurement accuracy for signals with many harmonics, such as the drain waveform of a class-E PA, enabling e.g. adaptive tuning of the coefficients of the RF-PA's DPD.

To improve RF-PA reliability under load mismatch a self-protection technique is presented and demonstrated with a 65 nm CMOS class-E RF-PA in chapter 6. The technique uses the peak switch voltage of the RF-waveform and a self-protective control loop determines based on the peak voltage to add or subtract capacitance from the drain node of the class-E PA, effectively tuning the relative resonance frequency q of the class-E PA. This effectively tunes the relative resonance frequency of the PA, increasing the safe-operating-area up to VSWR of 19:1, while seeing a worst-case degradation in output power and efficiency of 1.6 dB and 6% respectively.

Digital pre-distortion is an effective technique to improve RF-PA linearity, but load mismatch decreases the effectiveness of feedforward (static) DPD. A polar class-E PA with an integrated RF-waveform characterizer is presented in chapter 7, enabling adaptive digital pre-distortion. The integrated waveform characterizer enables estimation of both the AM-AM and AM-PM curves during load-pull of the RF-PA, allowing the DPD coefficients to be dynamically

updated to compensate for the change in the load impedance. Load-pull measurements were performed for a VSWR up to 9:1 on an 1 MHz 1024-QAM signal and the DPD coefficients were dynamically updated by using the measured information from the RF-waveform characterizer. Measurement results show that both the EVM and ACPR can be maintained over a significantly larger area on the Smith chart compared to static 50Ω optimized DPD.

8.2 Original contributions

This thesis contains several original contributions to enable robust, efficient and high performance RF-PAs:

- The introduction of a RF-waveform characterizer that can measure the DC voltage and the first three harmonics of the RF-waveform [74].
- The introduction of a technique to significantly reduce the effect of delay cell mismatch on the sampling accuracy in the RF-waveform characterizer [74].
- The introduction of a technique to improve the save-operating-area of a class-E PA by measuring the peak drain voltage and adding or removing drain capacitance by means of a capacitor array [75, 119]
- The design of a polar modulated class-E PA that utilizes the RF-waveform characterizer to tune DPD coefficients, achieving a significant improvement of EVM and ACPR for VSWR 9:1. [76]
- The development of an algorithm that can resolve frequency ambiguity and demodulate signals with an orthogonal frequency basis spanning multiple Nyquist zones by sampling at two distinct sample rates. It requires that the aggregate information-bearing bandwidth of the signals is less than half the cumulative data converter sampling rates.

Appendix A

Numerical example of the MRU algorithm

This appendix gives a numerical example of the algorithm described in this paper. In this example the set of modulated sub-carriers S in the input signal $x(t)$ is chosen as:

$$S = \{0, 1, 3, 5\} \quad (\text{A.1})$$

and the set A containing the complex value coefficients corresponding to the sub-carriers in S are chosen to be:

$$A = \{0, j1, j2, j3\} \quad (\text{A.2})$$

where $j^2 = -1$. The sets S and A respectively describe the spectral and complex value (magnitude and phase) content of the input signal $x(t)$ in equation (5.1). The input signal is then sampled at two different (non-integer multiples) frequencies $M_1 f_o$ and $M_2 f_o$, where in this example $M_1 = 4$ and $M_2 = 5$. Sampling for a duration of $\frac{1}{f_o}$ and performing a DFT on the sampled data results in the DFT vectors \mathbf{D}_{M1} and \mathbf{D}_{M2} :

$$D_{M1} = \begin{bmatrix} 0 & j2 & 0 & -j2 \end{bmatrix}^T \quad (\text{A.3})$$

$$D_{M2} = \begin{bmatrix} 0 & j1 & -j2 & j2 & -j1 \end{bmatrix}^T. \quad (\text{A.4})$$

Combining the results of D_{M1} and D_{M2} into the vector D_c results in:

$$D_c = \begin{bmatrix} 0 & j2 & 0 & -j2 & 0 & j1 & -j2 & j2 & -j1 \end{bmatrix}^T. \quad (\text{A.5})$$

In order to reconstruct the complex values of the sub-carriers in the input signal, the MRU algorithm requires both the combined DFT vector \mathbf{D}_c and the aliasing pattern, \mathbf{P}_c (5.16).

The matrix \mathbf{P}_c is pre-calculated based on the sub-carriers in S . \mathbf{P}_c describes the contribution of the complex values in A belonging to the sub-carriers in S to the DFT bins in \mathbf{D} . Using (5.11) and (5.12) the values of each of the elements in the matrix \mathbf{P} are calculated. The elements in \mathbf{P} are equal to 1 if $S_l = k + rM$ in case of the even columns and $S_l = -k + rM$ in case of the odd columns where k is the row number and $0 \leq l < |S|$. The aliasing pattern \mathbf{P}_{M1} corresponding to a sample rate of $M_1 f_o = 4f_o$ is:

$$P_{M1} = \begin{pmatrix} 1 & 1 & 0 & 0 & 0 & 0 & 0 & 0 \\ 0 & 0 & 1 & 0 & 0 & 1 & 1 & 0 \\ 0 & 0 & 0 & 0 & 0 & 0 & 0 & 0 \\ 0 & 0 & 0 & 1 & 1 & 0 & 0 & 1 \end{pmatrix} \quad (\text{A.6})$$

As described in Section III, the even columns in (A.6) contain information about the contribution of A to \mathbf{D} and the odd columns describe the contribution of A^* to \mathbf{D} . To illustrate how the matrix \mathbf{P}_c links A to \mathbf{D} we use the second row of (A.6) in (5.10) resulting in :

$$\begin{aligned} D_{M1}[1] &= P_{M1}[0]A_0 + P_{M1}[1]A_0^* + P_{M1}[2]A_1 + \\ &\quad P_{M1}[3]A_1^* + P_{M1}[4]A_2 + P_{M1}[5]A_2^* + \\ &\quad P_{M1}[6]A_3 + P_{M1}[7]A_3^* \\ &= j1 - j2 + j3 = j2 \end{aligned} \quad (\text{A.7})$$

which matches $D_{M1}[1]$ in (A.3).

The aliasing pattern P_{M2} corresponding to a sample rate of $M_2 f_o = 5f_o$ is:

$$P_{M2} = \begin{pmatrix} 1 & 1 & 0 & 0 & 0 & 0 & 0 & 0 \\ 0 & 0 & 1 & 0 & 0 & 0 & 0 & 0 \\ 0 & 0 & 0 & 0 & 1 & 0 & 0 & 1 \\ 0 & 0 & 0 & 0 & 0 & 1 & 1 & 0 \\ 0 & 0 & 0 & 1 & 0 & 0 & 0 & 0 \end{pmatrix} \quad (\text{A.8})$$

The combined pattern matrix P_c is calculated by using (A.6) and (A.8) in

$$\begin{pmatrix} A_0 \\ A_0^* \\ A_1 \\ A_1^* \\ A_2 \\ A_2^* \\ A_3 \\ A_3^* \end{pmatrix}_{\mathbf{A_R}} = \underbrace{\begin{pmatrix} 0.44 & -0.06 & 0 & -0.06 & 0.06 & 0.06 & 0.06 & 0.06 \\ 0.44 & -0.06 & 0 & -0.06 & 0.06 & 0.06 & 0.06 & 0.06 \\ 0.12 & 0.13 & 0 & 0.12 & -0.12 & 0.87 & -0.12 & -0.13 \\ 0.12 & 0.12 & 0 & 0.12 & -0.12 & -0.12 & -0.12 & 0.88 \\ 0.13 & 0.12 & 0 & 0.13 & -0.13 & -0.13 & 0.87 & -0.12 \\ 0.13 & 0.13 & 0 & 0.13 & -0.13 & -0.12 & -0.13 & -0.13 \\ -0.38 & 0.62 & 0 & -0.37 & 0.38 & -0.62 & 0.37 & 0.38 \\ -0.37 & -0.37 & 0 & 0.62 & 0.37 & 0.37 & -0.62 & -0.63 \end{pmatrix}}_{\mathbf{P_c^{-1}}} \underbrace{\begin{pmatrix} 0 \\ -j2 \\ 0 \\ j2 \\ 0 \\ j1 \\ -j2 \\ j2 \\ -j1 \end{pmatrix}}_{\mathbf{D_c}}$$

(A.37)

(5.15), resulting in:

$$P_c = \begin{pmatrix} 1 & 1 & 0 & 0 & 0 & 0 & 0 & 0 \\ 0 & 0 & 1 & 0 & 0 & 1 & 1 & 0 \\ 0 & 0 & 0 & 0 & 0 & 0 & 0 & 0 \\ 0 & 0 & 0 & 1 & 1 & 0 & 0 & 1 \\ 1 & 1 & 0 & 0 & 0 & 0 & 1 & 1 \\ 0 & 0 & 1 & 0 & 0 & 0 & 0 & 0 \\ 0 & 0 & 0 & 0 & 0 & 1 & 0 & 0 \\ 0 & 0 & 0 & 0 & 1 & 0 & 0 & 0 \\ 0 & 0 & 0 & 1 & 0 & 0 & 0 & 0 \end{pmatrix} \quad (\text{A.9})$$

Calculating the left-inverse of \mathbf{P}_c results in \mathbf{P}_c^{-1} (rounded to second decimal in this example), which together with \mathbf{D}_c enables the reconstruction of the complex values A (magnitude and phase) corresponding to the sub-carriers described by S . The reconstructed complex value vector \mathbf{A}_R using \mathbf{P}_c^{-1} and \mathbf{D}_c can be calculated from (A.37).

Appendix B

IQ extension of the MRU algorithm

Conventional IQ demodulation systems already use two ADCs, one in each of the I and Q paths. This section will derive the algorithm such that MRU can be used in an IQ system. The system overview is given in Fig. B.1.

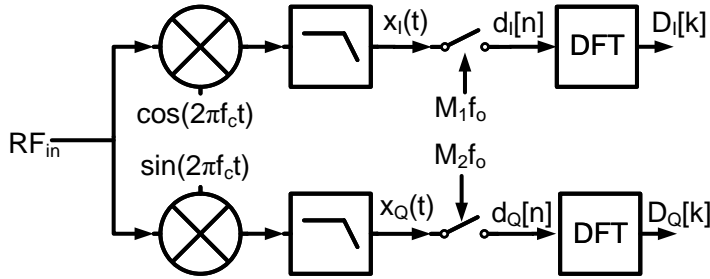


Figure B.1: MRU IQ system overview. The lowpass filters are only used to filter out the high frequency content and are not used as anti-aliasing filters.

The RF-input signal can be described by

$$x_{RF}(t) = \sum_{l \in L} \left(A_l e^{j2\pi(f_c + S_l f_o)t} + A_l^* e^{-j2\pi(f_c + S_l f_o)t} \right), \quad (\text{B.1})$$

where f_c is the bandpass center frequency and $S_l \in \mathbb{Z}$. Down conversion by respectively $\cos(2\pi f_c t)$ and $\sin(2\pi f_c t)$ and filtering the up-conversion products

results in the baseband I and Q signals give by

$$x_I(t) = \sum_{l \in L} \left(A_l e^{j2\pi S_l f_o t} + A_l^* e^{-j2\pi S_l f_o t} \right) \quad (\text{B.2})$$

and $x_Q(t) = -jx_I(t)$.

Sampling the analog signals $x_I(t)$ and $x_Q(t)$ results in the two data-streams $d_I[n]$ and $d_Q[n]$. Performing a DFT on both $d_I[n]$ and $d_Q[n]$ results in the two dataset

$$D_I[k] = \sum_{l \in L} \left(\sum_{r=-\infty}^{\infty} \left(A_l \delta(S_l - k - rM) + A_l^* \delta(S_l + k - rM) \right) \right), \quad (\text{B.3})$$

which describe the elements of the complex DFT vectors $\mathbf{D_I}$ and $\mathbf{D_Q}$ and $D_Q[k] = -jD_I[k]$.

The matrix $\mathbf{P_I}$ describing the aliasing pattern of the input signal to $\mathbf{D_I}$ is equal to (5.11) and (5.12), since they both describe the in-phase aliasing pattern. The matrix $\mathbf{P_Q}$ describing the quadrature aliasing pattern is derived from $D_Q[k]$ in a similar way as (5.11) and (5.12) are derived and is given by

$$P_Q[k, 2l] = \sum_{r=-\infty}^{\infty} \delta(S_l - k - rM) \quad (\text{B.4})$$

$$P_Q[k, 2l + 1] = - \sum_{r=-\infty}^{\infty} \delta(S_l + k - rM) \quad (\text{B.5})$$

The matrices $\mathbf{P_c}$ and $\mathbf{D_c}$ are formed similar to (5.15) and (5.14) by combining $\mathbf{P_I}$ with $\mathbf{P_Q}$ and $\mathbf{D_I}$ with $\mathbf{D_Q}$ resulting in

$$\mathbf{P_c} = \begin{bmatrix} \mathbf{P_I} \\ \mathbf{P_Q} \end{bmatrix}, \quad \mathbf{D_c} = \begin{bmatrix} \mathbf{D_I} \\ \pm j \mathbf{D_Q} \end{bmatrix}. \quad (\text{B.6})$$

where the sign of $\mathbf{D_Q}$ determines if the MRU algorithm should solve for the upper (+) or lower sideband (-). The final reconstruction is analog to the conventional case by using (5.16).

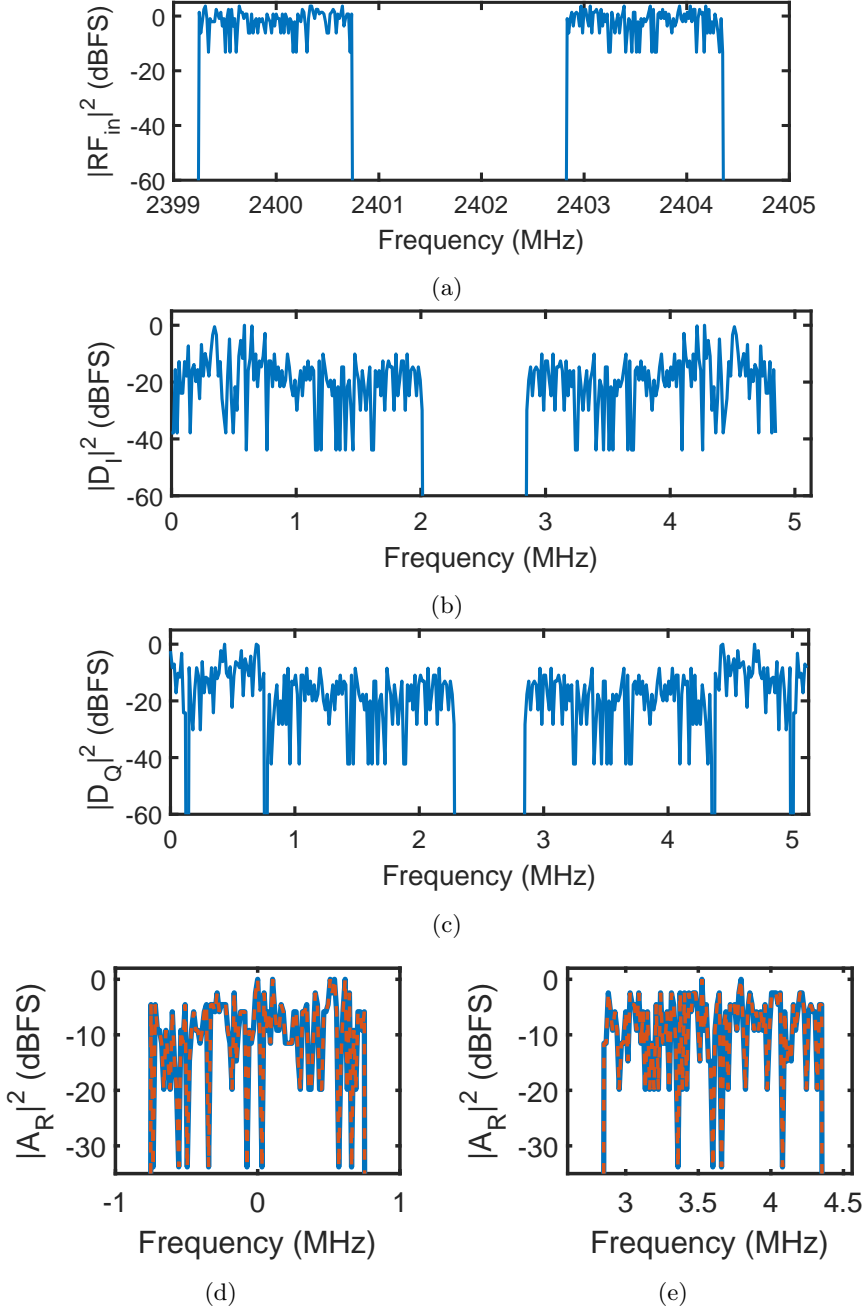


Figure B.2: (a) RF-input spectrum. Measured spectra of the dual-band OFDM signal after down-conversion for a single symbol. (b) 4.86 MS/s DFT spectrum ($|D_I|^2$) of the I-path. (c) 5.13 MS/s DFT spectrum ($|D_Q|^2$) of the Q-path. (d) and (e) shows the zoom-in of the recovered signal with both the measured (solid line) and the ideal input (dash line).

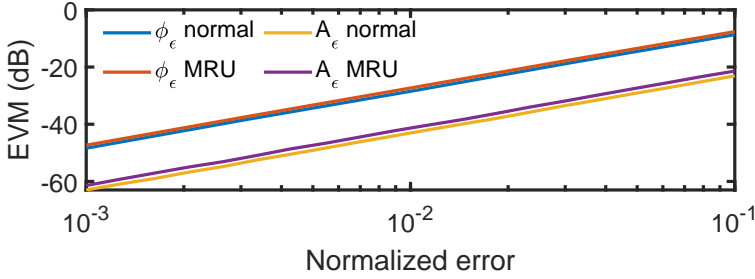


Figure B.3: Simulated EVM due to gain and phase mismatch in an IQ system. The results are for both a conventional oversampled system and the proposed MRU algorithm. A_ϵ is the normalized gain mismatch (e.g. $10^{-2} = 1\%$) and the phase mismatch ϕ_ϵ is normalized to 2π .

A simulation is performed to demonstrate MRU in an IQ system. Fig. B.2(a) shows the RF-input signal. It consists of two 1.5MHz OFDM signals centred at 2.4GHz and 2.4036GHz. The RF signal is down-converted, filtered and sampled. Fig. B.2(b) and (c) shows the resulting DFTs $\mathbf{D_I}$ and $\mathbf{D_Q}$ of the sampled datastreams $d_I[n]$ and $d_Q[n]$. Finally Fig. B.2(d) and (e) show a zoom-in of the separately reconstructed bands with an overlay of the original input spectrum, demonstrating that the input and output spectra are equal.

Any mismatch between the I and Q paths degrades the accuracy of the signal demodulation, where commonly occurring mismatch in IQ systems are gain and phase mismatch. Fig. B.3 shows the simulated results for the gain mismatch A_ϵ normalized to the ideal gain (e.g. $10^{-2} = 1\%$) and phase mismatch ϕ_ϵ normalized to 2π for both a conventional oversampled IQ system and the MRU algorithm. Compared to the conventional case the MRU algorithm degrades the EVM by 1 dB and 1.5 dB for phase and gain mismatch respectively. The degradation is independent on the amount of mismatch, where the degradation only depends on the condition number of the matrix $\mathbf{D_c}$ (see section 5.5.1).

Appendix C

Characterization of harmonics in an RF-PA

Another use case for the MRU algorithm is the characterization of the harmonics of an RF-waveform to improve the reliability and pre-distortion in an RF-PA as mentioned in Section 5.1. The work in [74] uses 8 equally spaced samples over a single period of the RF-waveform, allowing characterization of the DC component and the first 3 harmonics. However, when the RF-waveform contains more harmonics aliasing will occur. Down-mixing with a square wave at f_o results in the harmonics becoming indistinguishable, where mixing with a frequency offset can result in frequency pulling. To prevent aliasing the sample rate can be increased, but this would increase the system clock rate which might not be feasible at all times. MRU can increase the number of distinguishable harmonics by adding another sampler at a lower sample rate, such as 7 samples per period.

Fig. C.1 (a) shows an RF-waveform with $f_o = 2.5$ GHz and the resulting samples when sampling at rates of 20 GS/s ($M_1 = 8$, '□') and 17.5 GS/s ($M_2 = 7$, '×'). Fig. C.1 (b) and (c) show the aliased DFT spectra of the RF-input signal when sampling at 20 GS/s and 17.5 GS/s respectively. Fig. C.1 (d) shows the RF-input spectrum (line) and the reconstructed RF-spectrum (○) using MRU. By using MRU the number of harmonics that can be characterized is increased from 3 to 6. In contrast, a conventional system to characterize these harmonics would require a sample rate higher than 30 GS/s.

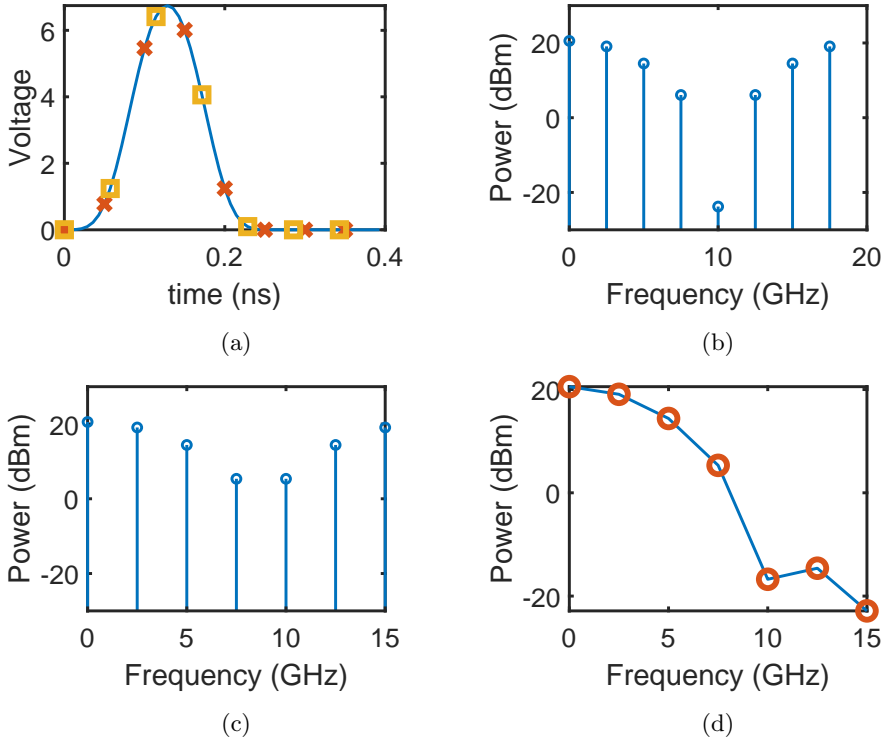


Figure C.1: (a) Characterization of a $f_o = 2.5$ GHz RF-waveform in an RF-PA. The '□' and '×' indicate the sampled signal for $M_1 = 8$ and $M_2 = 7$ respectively. (b) and (c) are the DFT spectra $|\mathbf{D}_1|^2$ and $|\mathbf{D}_2|^2$ for $M_1 = 8$ and $M_2 = 7$ samples per period respectively. (d) Input RF-waveform spectrum (line) and the reconstructed spectrum $|\mathbf{A}_R|^2$ (○).

Acknowledgement

I have spent more than six years working at the ICD group and had the honor of learning from and working with many people. I would like to take this opportunity to thank everyone who supported me during this journey.

First of all, I would like to thank my promoter, Bram Nauta, for the opportunity to do my Ph.D. at the ICD group. Maybe as important as starting my Ph.D., Bram also gave me an excellent opportunity to finish it, which resulted in this thesis. During our discussions, I enjoyed how you can find simple-to-understand analogies for even complex systems, which provided new insights and allows even complex ideas to be explained relatively easy. Furthermore, I would like to thank Bram for helping with restructuring the introduction of my last paper, which probably ended the seemingly endless review loop. His eye for detail, structure, and both industrial and scientific relevance significantly improved my work.

I would also like to take this opportunity to thank Anne-Johan Annema, who kindled my enthusiasm for electronics at the beginning of my studies. I still remember the brightly colored slides from my lectures in comic-sans, which is of course the best font for this. I learned many things from working with you, that I still apply regularly e.g. basic problem solving and simplifying models. Of course, I also learned many peculiar skills, such as impedance matching cutlery and calibrating electronics with a sledgehammer. I really enjoyed supervising module 3 with you. Helping the students and testing their amplifiers or FM-transmitters was good fun, which always produced a lot of interference (both audio and RF), (controlled) chaos and with a bit of luck a lot of smoke.

My gratitude also goes to the other committee members. I would like to thank Leo de Vreede and Peter Baltus for taking the time to read my thesis.

Special thanks to both Frank van Vliet and Andre Kokkeler for scrutinizing my thesis and providing me with feedback.

I would also like to thank Eric Klumperink for supervising me during my last two years at the ICD group. Even though we only worked together for a short time I learned a lot from you. I really appreciated your structured way of dealing with even complex problems. Thanks to you I am now finally able to finish the calculations I tried during wireless transceiver electronics. I would also like to acknowledge Mark Oude Alink and Ronan van der Zee for all the discussions and inputs they delivered during my time at the ICD group.

Doing a Ph.D. in IC design also requires a lot of practical work. I spend what seemed like ages in the lab performing measurements and I would like to thank Henk de Vries and Arnoud Rop for their support in setting up the lab equipment and tolerating the persistent presence of one of my many measurements setups. Without you guys performing the measurements would have been tedious. I would also like to thank Gerard Wienk for his support during my many tape-outs and his extensive knowledge of the Cadence tools. Without you, many tape-out deadlines would have been stretched to their absolute limits. Thank you Gerdien for making sure that everything runs smoothly and for solving many of the more practical problems.

I would like to express my sincere gratitude to Joeri Lechevallier and Harijot Singh Bindra. It was a pleasure sharing an office with you guys during (almost) my entire time at the ICD design group, as well as many dinners and other fun activities. I spent a lot of time in the lab together with Harijot, which often resulted in us measuring diodes. Many evenings were spent playing around with the ADC in some way, which resulted in more than 100 GB of data and even in a publication after more than three years. Thanks to Joeri for sharing the daily morning coffee with me, during which we discussed many things. It guaranteed a great start to the day.

Special thanks should go to Awani Khodkumbhe and Jeroen Ponte, who both really helped me out with measuring and writing some of my work. I am grateful for all the excellent results you guys delivered and it was a great pleasure working with you both. Furthermore, I would like to thank both my present and former ICD colleagues: Alexander, Ali, Andreas, Anton, Anoop, Bart, Claudia, Chris, Dirk-Jan, Erwin, Hugo, Inês, Joep, Johan, Labrinus,

Maryam, Nimit, Robin, Sajad, Thomas, Vijaya, YC and Zhiliang for all the nice talks and discussions.

My parents deserve a special thank you for always supporting me during my Ph.D. Without your unconditional support, this thesis would have never seen the day of light and I am grateful for your continued support.

Lastly, I would like to thank Sara for her support during my Ph.D. I am grateful for your companionship, especially during the time when I wrote most of this thesis. I am glad that we can finally spend a holiday during which I won't require a laptop to write a paper for this thesis anymore.

List of publications

- **M. Huiskamp**, A. Annema and B. Nauta, "A Delay Spread Cancelling Waveform Characterizer for RF Power Amplifiers," in IEEE Transactions on Circuits and Systems II: Express Briefs, vol. 65, no. 12, pp. 1834-1838, Dec. 2018.
doi: 10.1109/TCSII.2018.2873835
- J. Ponte, A. Ghahremani, **M. Huiskamp**, A. Annema and B. Nauta, "Augmentation of Class-E PA Reliability under Load Mismatch Conditions," 2018 25th IEEE International Conference on Electronics, Circuits and Systems (ICECS), Bordeaux, 2018, pp. 33-36.
doi: 10.1109/ICECS.2018.8617864
- J. Ponte, A. Ghahremani, **M. Huiskamp**, A. Annema and B. Nauta, "Theory and Implementation of a Load-Mismatch Protective Class-E PA System," in IEEE Transactions on Circuits and Systems I: Regular Papers, vol. 67, no. 2, pp. 369-377, Feb. 2020.
doi: 10.1109/TCSI.2019.2926468
- A. Khodkumbhe, **M. Huiskamp**, A. Ghahremani, B. Nauta and A. Annema, "Preserving Polar Modulated Class-E Power Amplifier Linearity under Load Mismatch," 2020 IEEE Radio Frequency Integrated Circuits Symposium (RFIC), Los Angeles, CA, USA, 2020, pp. 295-298, doi: 10.1109/RFIC49505.2020.9218279.

Accepted for publication:

- **M. Huiskamp**, M. S. Oude Alink, B. Nauta, A. Annema and H. S. Bindra, “Reconstructing Aliased Frequency Spectra by Using Multiple Sample Rates”, in IEEE Transactions on Circuits and Systems I: Regular Papers , doi: 10.1109/TCSL.2021.3131273.

Bibliography

- [1] G. E. Becker and S. H. Autler, “Water Vapor Absorption of Electromagnetic Radiation in the Centimeter Wave-Length Range,” *Phys. Rev.*, vol. 70, pp. 300–307, Sep 1946.
- [2] J. H. van Vleck, “The Absorption of Microwaves by Oxygen,” *Phys. Rev.*, vol. 71, pp. 413–424, Apr 1947.
- [3] 3GPP, “Evolved Universal Terrestrial Radio Access (E-UTRA); User Equipment (UE) radio transmission and reception,” 3rd Generation Partnership Project (3GPP), Technical Specification (TS) 36.101, 02 2020, version 14.14.0. [Online]. Available: <https://portal.3gpp.org/desktopmodules/Specifications/SpecificationDetails.aspx?specificationId=2411>
- [4] —, “5G; NR; User Equipment (UE) radio transmission and reception; Part 1: Range 1 Standalone,” 3rd Generation Partnership Project (3GPP), Technical Specification (TS) 38.101-1, 04 2020, version 15.9.0. [Online]. Available: <https://portal.3gpp.org/desktopmodules/Specifications/SpecificationDetails.aspx?specificationId=3283>
- [5] “Ericsson Mobility Visualizer, Cellular IoT,” <https://www.ericsson.com/en/mobility-report/mobility-visualizer?f=14&ft=1&r=1&t=21,22,23&s=14&u=1&y=2015,2025&c=1>, accessed: 2020-02-17.
- [6] A. Al-Fuqaha, M. Guizani, M. Mohammadi, M. Aledhari, and M. Ayyash, “Internet of Things: A Survey on Enabling Technologies, Protocols, and Applications,” *IEEE Communications Surveys Tutorials*, vol. 17, no. 4, pp. 2347–2376, Fourthquarter 2015.

- [7] A. Molisch, *Wireless Communications*, ser. Wiley - IEEE. Wiley, 2012.
- [8] P. H. Woerlee, M. J. Knitel, R. van Langevelde, D. B. M. Klaassen, L. F. Tiemeijer, A. J. Scholten, and A. T. A. Zegers-van Duijnhoven, "RF-CMOS performance trends," *IEEE Transactions on Electron Devices*, vol. 48, no. 8, pp. 1776–1782, 2001.
- [9] A. Rofougaran, G. Chang, J. J. Rael, J. Y. . Chang, M. Rofougaran, P. J. Chang, M. Djafari, M. . Ku, E. W. Roth, A. A. Abidi, and H. Samueli, "A single-chip 900-MHz spread-spectrum wireless transceiver in 1-/spl mu/m CMOS. I. Architecture and transmitter design," *IEEE Journal of Solid-State Circuits*, vol. 33, no. 4, pp. 515–534, 1998.
- [10] M. Steyaert, M. Borremans, J. Janssens, B. de Muer, I. Itoh, J. Craninckx, J. Crols, E. Morifuji, S. Momose, and W. Sansen, "A single-chip CMOS transceiver for DCS-1800 wireless communications," in *1998 IEEE International Solid-State Circuits Conference. Digest of Technical Papers, ISSCC. First Edition (Cat. No.98CH36156)*, 1998, pp. 48–49.
- [11] G. E. Moore, "Cramming More Components Onto Integrated Circuits," *Proceedings of the IEEE*, vol. 86, no. 1, pp. 82–85, 1998.
- [12] D. M. Pozar, *Microwave engineering; 3rd ed.* Hoboken, NJ: Wiley, 2005.
- [13] C. Balanis, *Antenna Theory: Analysis and Design.* Wiley, 2015.
- [14] K. R. Boyle, Y. Yuan, and L. P. Ligthart, "Analysis of Mobile Phone Antenna Impedance Variations With User Proximity," *IEEE Transactions on Antennas and Propagation*, vol. 55, no. 2, pp. 364–372, Feb 2007.
- [15] I. Aoki, S. D. Kee, D. B. Rutledge, and A. Hajimiri, "Distributed active transformer-a new power-combining and impedance-transformation technique," *IEEE Transactions on Microwave Theory and Techniques*, vol. 50, no. 1, pp. 316–331, 2002.
- [16] H. Bode, *Network Analysis and Feedback Amplifier Design*, ser. Bell Telephone Laboratories series. D. Van Nostrand Company, Incorporated, 1945.

-
- [17] R. Fano, "Theoretical limitations on the broadband matching of arbitrary impedances," *Journal of the Franklin Institute*, vol. 249, no. 1, pp. 57 – 83, 1950.
- [18] B. Razavi, *RF Microelectronics*, ser. Prentice Hall communications engineering and emerging technologies series. Prentice Hall, 2012.
- [19] S. Cripps, *RF Power Amplifiers for Wireless Communications*, ser. Artech House microwave library. Artech House, 2006.
- [20] T. Johansson and J. Fritzin, "A Review of Watt-Level CMOS RF Power Amplifiers," *IEEE Transactions on Microwave Theory and Techniques*, vol. 62, no. 1, pp. 111–124, 2014.
- [21] A. J. Annema, G. J. G. M. Geelen, and P. C. de Jong, "5.5-V I/O in a 2.5-V 0.25- μm CMOS technology," *IEEE Journal of Solid-State Circuits*, vol. 36, no. 3, pp. 528–538, 2001.
- [22] A. Mazzanti, L. Larcher, R. Brama, and F. Svelto, "Analysis of reliability and power efficiency in cascode class-E PAs," *IEEE Journal of Solid-State Circuits*, vol. 41, no. 5, pp. 1222–1229, 2006.
- [23] A. J. Annema, B. Nauta, R. van Langevelde, and H. Tuinhout, "Analog circuits in ultra-deep-submicron CMOS," *IEEE Journal of Solid-State Circuits*, vol. 40, no. 1, pp. 132–143, 2005.
- [24] T. Yan, H. Liao, Y. Z. Xiong, R. Zeng, J. Shi, and R. Huang, "Cost-Effective Integrated RF Power Transistor in 0.18- μm CMOS Technology," *IEEE Electron Device Letters*, vol. 27, no. 10, pp. 856–858, 2006.
- [25] H. Xiao, L. Zhang, R. Huang, F. Song, D. Wu, H. Liao, W. Wong, and Y. Wang, "A Novel RF LDMOS Fabricated With Standard Foundry Technology," *IEEE Electron Device Letters*, vol. 30, no. 4, pp. 386–388, 2009.
- [26] C. E. Shannon, "A mathematical theory of communication," *The Bell System Technical Journal*, vol. 27, no. 3, pp. 379–423, 1948.
- [27] 3GPP, "5G; NR; Physical channels and modulation," 3rd Generation Partnership Project (3GPP), Technical Specification (TS) 38.101, 07

- 2020, version 16.2.0. [Online]. Available: https://www.etsi.org/deliver/etsi_ts/138200_138299/138211/16.02.00_60/ts_138211v160200p.pdf
- [28] S. Weinstein and P. Ebert, "Data Transmission by Frequency-Division Multiplexing Using the Discrete Fourier Transform," *IEEE Transactions on Communication Technology*, vol. 19, no. 5, pp. 628–634, 1971.
- [29] Y. Li, L. J. Cimini, and N. R. Sollenberger, "Robust channel estimation for OFDM systems with rapid dispersive fading channels," *IEEE Transactions on Communications*, vol. 46, no. 7, pp. 902–915, 1998.
- [30] R. W. Chang, "Synthesis of band-limited orthogonal signals for multi-channel data transmission," *The Bell System Technical Journal*, vol. 45, no. 10, pp. 1775–1796, 1966.
- [31] T. Pollet, M. Van Bladel, and M. Moeneclaey, "BER sensitivity of OFDM systems to carrier frequency offset and Wiener phase noise," *IEEE Transactions on Communications*, vol. 43, no. 2/3/4, pp. 191–193, 1995.
- [32] H. Ochiai and H. Imai, "On the distribution of the peak-to-average power ratio in OFDM signals," *IEEE Transactions on Communications*, vol. 49, no. 2, pp. 282–289, 2001.
- [33] P. Massoud Salehi and J. Proakis, *Digital Communications*. McGraw-Hill Education, 2007.
- [34] S. Daumont, B. Rihawi, and Y. Lout, "Root-Raised Cosine filter influences on PAPR distribution of single carrier signals," in *2008 3rd International Symposium on Communications, Control and Signal Processing*, 2008, pp. 841–845.
- [35] M. Vigilante, E. McCune, and P. Reynaert, "To EVM or Two EVMs?: An Answer to the Question," *IEEE Solid-State Circuits Magazine*, vol. 9, no. 3, pp. 36–39, 2017.
- [36] P. Reynaert and M. Steyaert, *RF Power Amplifiers for Mobile Communications*, ser. Analog Circuits and Signal Processing. Springer Netherlands, 2006.

-
- [37] S. H. Han and J. H. Lee, "An overview of peak-to-average power ratio reduction techniques for multicarrier transmission," *IEEE Wireless Communications*, vol. 12, no. 2, pp. 56–65, 2005.
- [38] T. Jiang, Y. Yang, and Y. Song, "Exponential companding technique for PAPR reduction in OFDM systems," *IEEE Transactions on Broadcasting*, vol. 51, no. 2, pp. 244–248, 2005.
- [39] M. Acar, A. J. Annema, and B. Nauta, "Analytical Design Equations for Class-E Power Amplifiers," *IEEE Transactions on Circuits and Systems I: Regular Papers*, vol. 54, no. 12, pp. 2706–2717, 2007.
- [40] A. Ghahremani, A. J. Annema, and B. Nauta, "Load Mismatch Sensitivity of Class-E Power Amplifiers," *IEEE Transactions on Microwave Theory and Techniques*, vol. 67, no. 1, pp. 216–230, 2019.
- [41] H. Chireix, "High Power Outphasing Modulation," *Proceedings of the Institute of Radio Engineers*, vol. 23, no. 11, pp. 1370–1392, 1935.
- [42] L. R. Kahn, "Single-sideband transmission by envelope elimination and restoration," *Proceedings of the IRE*, vol. 40, no. 7, pp. 803–806, 1952.
- [43] A. A. M. Saleh, "Frequency-Independent and Frequency-Dependent Nonlinear Models of TWT Amplifiers," *IEEE Transactions on Communications*, vol. 29, no. 11, pp. 1715–1720, 1981.
- [44] W. Bosch and G. Gatti, "Measurement and simulation of memory effects in predistortion linearizers," *IEEE Transactions on Microwave Theory and Techniques*, vol. 37, no. 12, pp. 1885–1890, 1989.
- [45] J. H. K. Vuolevi, T. Rahkonen, and J. P. A. Manninen, "Measurement technique for characterizing memory effects in rf power amplifiers," *IEEE Transactions on Microwave Theory and Techniques*, vol. 49, no. 8, pp. 1383–1389, 2001.
- [46] R. Hassun, M. Flaherty, R. Matreci, and M. Taylor, "Effective evaluation of link quality using error vector magnitude techniques," in *Proceedings of 1997 Wireless Communications Conference*, 1997, pp. 89–94.

- [47] W. H. Doherty, "A New High Efficiency Power Amplifier for Modulated Waves," *Proceedings of the Institute of Radio Engineers*, vol. 24, no. 9, pp. 1163–1182, 1936.
- [48] D. Rudolph, "Out-of-band emissions of digital transmissions using Kahn EER technique," *IEEE Transactions on Microwave Theory and Techniques*, vol. 50, no. 8, pp. 1979–1983, 2002.
- [49] —, "Kahn EER technique with single-carrier digital modulations," *IEEE Transactions on Microwave Theory and Techniques*, vol. 51, no. 2, pp. 548–552, 2003.
- [50] F. H. Raab, "Intermodulation distortion in kahn-technique transmitters," *IEEE Transactions on Microwave Theory and Techniques*, vol. 44, no. 12, pp. 2273–2278, 1996.
- [51] F. Wang, D. Kimball, J. Popp, A. Yang, D. Y. C. Lie, P. Asbeck, and L. Larson, "Wideband envelope elimination and restoration power amplifier with high efficiency wideband envelope amplifier for WLAN 802.11g applications," in *IEEE MTT-S International Microwave Symposium Digest, 2005.*, 2005, pp. 4 pp.–648.
- [52] J. S. Walling, S. S. Taylor, and D. J. Allstot, "A Class-G supply modulator and Class-E PA in 130 nm cmos," *IEEE Journal of Solid-State Circuits*, vol. 44, no. 9, pp. 2339–2347, 2009.
- [53] F. H. Raab, B. E. Sigmon, R. G. Myers, and R. M. Jackson, "L-band transmitter using kahn eer technique," *IEEE Transactions on Microwave Theory and Techniques*, vol. 46, no. 12, pp. 2220–2225, 1998.
- [54] F. Raab, "Efficiency of Outphasing RF Power-Amplifier Systems," *IEEE Transactions on Communications*, vol. 33, no. 10, pp. 1094–1099, 1985.
- [55] A. K. Mustafa, S. Ahmed, and M. Faulkner, "Bandwidth Limitation for the Constant Envelope Components of an OFDM Signal in a LINC Architecture," *IEEE Transactions on Circuits and Systems I: Regular Papers*, vol. 60, no. 9, pp. 2502–2510, 2013.
- [56] H. Seidel, "A microwave feed-forward experiment," *The Bell System Technical Journal*, vol. 50, no. 9, pp. 2879–2916, 1971.

-
- [57] H. Seidel, H. R. Beurrier, and A. N. Friedman, "Error-controlled high power linear amplifiers at VHF," *The Bell System Technical Journal*, vol. 47, no. 5, pp. 651–722, 1968.
- [58] T. Arthanayake and H. B. Wood, "Linear amplification using envelope feedback," *Electronics Letters*, vol. 7, no. 7, pp. 145–146, 1971.
- [59] J. L. Dawson and T. H. Lee, "Automatic phase alignment for a fully integrated Cartesian feedback power amplifier system," *IEEE Journal of Solid-State Circuits*, vol. 38, no. 12, pp. 2269–2279, 2003.
- [60] J. Yi, Y. Yang, M. Park, W. Kang, and B. Kim, "Analog predistortion linearizer for high-power rf amplifiers," *IEEE Transactions on Microwave Theory and Techniques*, vol. 48, no. 12, pp. 2709–2713, 2000.
- [61] Seung-Yup Lee, Yong-Sub Lee, Seung-Ho Hong, Hyun-Sik Choi, and Yoon-Ha Jeong, "An adaptive predistortion rf power amplifier with a spectrum monitor for multicarrier wcdma applications," *IEEE Transactions on Microwave Theory and Techniques*, vol. 53, no. 2, pp. 786–793, 2005.
- [62] J. K. Cavers, "Amplifier linearization using a digital predistorter with fast adaptation and low memory requirements," *IEEE Transactions on Vehicular Technology*, vol. 39, no. 4, pp. 374–382, 1990.
- [63] Y. Y. Woo, J. Kim, J. Yi, S. Hong, I. Kim, J. Moon, and B. Kim, "Adaptive digital feedback predistortion technique for linearizing power amplifiers," *IEEE Transactions on Microwave Theory and Techniques*, vol. 55, no. 5, pp. 932–940, 2007.
- [64] S. Narayanan, "Application of volterra series to intermodulation distortion analysis of transistor feedback amplifiers," *IEEE Transactions on Circuit Theory*, vol. 17, no. 4, pp. 518–527, 1970.
- [65] L. Ding, G. T. Zhou, D. R. Morgan, Z. Ma, J. S. Kenney, J. Kim, and C. R. Giardina, "A robust digital baseband predistorter constructed using memory polynomials," *IEEE Transactions on Communications*, vol. 52, no. 1, pp. 159–165, 2004.

- [66] Chenming Hu, “Gate oxide scaling limits and projection,” in *International Electron Devices Meeting. Technical Digest*, 1996, pp. 319–322.
- [67] I. Aoki, S. Kee, R. Magoon, R. Aparicio, F. Bohn, J. Zachan, G. Hatcher, D. McClymont, and A. Hajimiri, “A fully-integrated quad-band gsm/gprs cmos power amplifier,” *IEEE Journal of Solid-State Circuits*, vol. 43, no. 12, pp. 2747–2758, 2008.
- [68] H. Yang, J. S. Yuan, Y. Liu, and E. Xiao, “Effect of gate-oxide breakdown on RF performance,” *IEEE Transactions on Device and Materials Reliability*, vol. 3, no. 3, pp. 93–97, 2003.
- [69] G. T. Sasse, F. G. Kuper, and J. Schmitz, “Mosfet degradation under rf stress,” *IEEE Transactions on Electron Devices*, vol. 55, no. 11, pp. 3167–3174, 2008.
- [70] F. M. d’Heurle, “Electromigration and failure in electronics: An introduction,” *Proceedings of the IEEE*, vol. 59, no. 10, pp. 1409–1418, 1971.
- [71] C. Constantinescu, “Trends and challenges in VLSI circuit reliability,” *IEEE Micro*, vol. 23, no. 4, pp. 14–19, 2003.
- [72] S. M. Bowers, K. Sengupta, K. Dasgupta, and A. Hajimiri, “A fully-integrated self-healing power amplifier,” in *IEEE Radio Frequency Integrated Circuits Symposium*, June 2012, pp. 221–224.
- [73] Y. Yoon, H. Kim, H. Kim, K. S. Lee, C. H. Lee, and J. S. Kenney, “A 2.4-GHz CMOS Power Amplifier With an Integrated Antenna Impedance Mismatch Correction System,” *IEEE Journal of Solid-State Circuits*, vol. 49, no. 3, pp. 608–621, March 2014.
- [74] M. Huiskamp, A. J. Annema, and B. Nauta, “A Delay Spread Cancelling Waveform Characterizer for RF Power Amplifiers,” *IEEE Transactions on Circuits and Systems II: Express Briefs*, vol. 65, no. 12, pp. 1834–1838, 2018.
- [75] J. Ponte, A. Ghahremani, M. Huiskamp, A. J. Annema, and B. Nauta, “Theory and Implementation of a Load-Mismatch Protective Class-E PA System,” *IEEE Transactions on Circuits and Systems I: Regular Papers*, vol. 67, no. 2, pp. 369–377, 2020.

-
- [76] A. Khodkumbhe, M. Huiskamp, A. Ghahremani, B. Nauta, and A. J. Annema, "Preserving Polar Modulated Class-E Power Amplifier Linearity under Load Mismatch," in *2020 IEEE Radio Frequency Integrated Circuits Symposium (RFIC)*, 2020, pp. 295–298.
- [77] N. F. Barber, "Narrow band-pass filter using modulation," *Wireless Engineer*, pp. 132–134, 1947.
- [78] B. D. Smith, "Analysis of Commutated Networks," *Transactions of the IRE Professional Group on Aeronautical and Navigational Electronics*, vol. PGAE-10, pp. 21–26, 1953.
- [79] C. Andrews and A. C. Molnar, "Implications of passive mixer transparency for impedance matching and noise figure in passive mixer-first receivers," *IEEE Transactions on Circuits and Systems I: Regular Papers*, vol. 57, no. 12, pp. 3092–3103, 2010.
- [80] —, "A passive mixer-first receiver with digitally controlled and widely tunable rf interface," *IEEE Journal of Solid-State Circuits*, vol. 45, no. 12, pp. 2696–2708, 2010.
- [81] M. C. M. Soer, E. A. M. Klumperink, P. T. de Boer, F. E. van Vliet, and B. Nauta, "Unified Frequency-Domain Analysis of Switched-Series-RC Passive Mixers and Samplers," *IEEE Transactions on Circuits and Systems I: Regular Papers*, vol. 57, no. 10, pp. 2618–2631, Oct 2010.
- [82] E. A. M. Klumperink, M. C. M. Soer, R. Struiksmma, F. E. van Vliet, and B. Nauta, "Towards Low Power N-Path Filters for Flexible RF-Channel Selection," in *Efficient Sensor Interfaces, Advanced Amplifiers and Low Power RF Systems*. Springer International Publishing, 2015.
- [83] S. Pavan and E. Klumperink, "Simplified Unified Analysis of Switched-RC Passive Mixers, Samplers, and N -Path Filters Using the Adjoint Network," *IEEE Transactions on Circuits and Systems I: Regular Papers*, vol. 64, no. 10, pp. 2714–2725, 2017.
- [84] Z. Ru, E. A. M. Klumperink, and B. Nauta, "Discrete-Time Mixing Receiver Architecture for RF-Sampling Software-Defined Radio," *IEEE Journal of Solid-State Circuits*, vol. 45, no. 9, pp. 1732–1745, 2010.

- [85] Z. Ru, N. A. Moseley, E. A. M. Klumperink, and B. Nauta, "Digitally Enhanced Software-Defined Radio Receiver Robust to Out-of-Band Interference," *IEEE Journal of Solid-State Circuits*, vol. 44, no. 12, pp. 3359–3375, 2009.
- [86] Y. Xu, J. Zhu, and P. R. Kinget, "A Blocker-Tolerant RF Front End With Harmonic-Rejecting N -Path Filter," *IEEE Journal of Solid-State Circuits*, vol. 53, no. 2, pp. 327–339, 2018.
- [87] A. Ghaffari, E. A. M. Klumperink, M. C. M. Soer, and B. Nauta, "Tunable High-Q N -Path Band-Pass Filters: Modeling and Verification," *IEEE Journal of Solid-State Circuits*, vol. 46, no. 5, pp. 998–1010, May 2011.
- [88] T. Iizuka and A. A. Abidi, "FET-R-C Circuits: A Unified Treatment—Part II: Extension to Multi-Paths, Noise Figure, and Driving-Point Impedance," *IEEE Transactions on Circuits and Systems I: Regular Papers*, vol. 63, no. 9, pp. 1337–1348, 2016.
- [89] A. Georgiadis, "Gain, Phase Imbalance, and Phase Noise Effects on Error Vector Magnitude," *IEEE Transactions on Vehicular Technology*, vol. 53, no. 2, pp. 443–449, 2004.
- [90] E. L. Firrao, A. J. Annema, F. E. van Vliet, and B. Nauta, "On the minimum number of states for switchable matching networks," *IEEE Transactions on Circuits and Systems I: regular papers*, vol. 62, no. 2, pp. 433–440, 2 2015, eemcs-eprint-25850.
- [91] S. M. Bowers, K. Sengupta, K. Dasgupta, B. D. Parker, and A. Hajimiri, "Integrated self-healing for mm-wave power amplifiers," *IEEE Transactions on Microwave Theory and Techniques*, vol. 61, no. 3, pp. 1301–1315, March 2013.
- [92] P. Colantonio, F. Giannini, E. Limiti, and V. Teppati, "An approach to harmonic load- and source-pull measurements for high-efficiency PA design," *IEEE Transactions on Microwave Theory and Techniques*, vol. 52, no. 1, pp. 191–198, Jan 2004.

-
- [93] A. Ghahremani, A. J. Annema, and B. Nauta, “Outphasing Class-E Power Amplifiers: From Theory to Back-Off Efficiency Improvement,” *IEEE Journal of Solid-State Circuits*, vol. 53, no. 5, pp. 1374–1386, May 2018.
- [94] R. C. H. van de Beek, E. A. M. Klumperink, C. S. Vaucher, and B. Nauta, “On jitter due to delay cell mismatch in DLL-based clock multipliers,” in *2002 IEEE International Symposium on Circuits and Systems. Proceedings*, vol. 2, 2002, pp. II–396–II–399 vol.2.
- [95] I. Galton, “Why Dynamic-Element-Matching DACs Work,” *IEEE Transactions on Circuits and Systems II: Express Briefs*, vol. 57, no. 2, pp. 69–74, Feb 2010.
- [96] R. B. Sanderson, J. B. Y. Tsui, and N. A. Freese, “Reduction of aliasing ambiguities through phase relations,” *IEEE Transactions on Aerospace and Electronic Systems*, vol. 28, no. 4, pp. 950–956, Oct 1992.
- [97] D. W. Tufts and H. Ge, “Digital estimation of frequencies of sinusoids from wide-band under-sampled data,” in *1995 International Conference on Acoustics, Speech, and Signal Processing*, vol. 5, May 1995, pp. 3155–3158 vol.5.
- [98] X. . Xia, “An Efficient Frequency-Determination Algorithm from Multiple Undersampled Waveforms,” *IEEE Signal Processing Letters*, vol. 7, no. 2, pp. 34–37, Feb 2000.
- [99] P. P. Vaidyanathan and P. Pal, “Sparse Sensing With Co-Prime Samplers and Arrays,” *IEEE Transactions on Signal Processing*, vol. 59, no. 2, pp. 573–586, Feb 2011.
- [100] C. E. Shannon, “Communication in the Presence of Noise,” *Proceedings of the IRE*, vol. 37, no. 1, pp. 10–21, Jan 1949.
- [101] R. G. Vaughan, N. L. Scott, and D. R. White, “The Theory of Bandpass Sampling,” *IEEE Transactions on Signal Processing*, vol. 39, no. 9, pp. 1973–1984, Sep. 1991.

- [102] D. M. Akos, M. Stockmaster, J. B. Y. Tsui, and J. Caschera, "Direct Bandpass Sampling of Multiple Distinct RF Signals," *IEEE Transactions on Communications*, vol. 47, no. 7, pp. 983–988, July 1999.
- [103] J. Gaskell, *Linear Systems, Fourier Transforms, and Optics*. New York: Wiley, 1978.
- [104] M. Pelgrom, *Analog-to-Digital Conversion*. Springer, 2010.
- [105] B. Razavi, "Problem of timing mismatch in interleaved ADCs," in *Proceedings of the IEEE 2012 Custom Integrated Circuits Conference*, Sep. 2012, pp. 1–8.
- [106] M. El-Chammas and B. Murmann, "General Analysis on the Impact of Phase-Skew in Time-Interleaved ADCs," *IEEE Transactions on Circuits and Systems I: Regular Papers*, vol. 56, no. 5, pp. 902–910, May 2009.
- [107] N. Sinha, M. Rachid, and S. Pamarti, "A sharp programmable passive filter based on filtering by Aliasing," in *2015 Symposium on VLSI Circuits (VLSI Circuits)*, June 2015, pp. C58–C59.
- [108] B. J. Thijssen, E. A. M. Klumperink, P. Quinlan, and B. Nauta, "A 0.06–3.4-MHz 92- μ W Analog FIR Channel Selection Filter With Very Sharp Transition Band for IoT Receivers," *IEEE Solid-State Circuits Letters*, vol. 2, no. 9, pp. 171–174, 2019.
- [109] H. S. Bindra, A. J. Annema, G. Wienk, B. Nauta, and S. M. Louwsma, "A 4MS/s 10b SAR ADC with integrated Class-A buffers in 65nm CMOS with near rail-to-rail input using a single 1.2V supply," in *2019 IEEE Custom Integrated Circuits Conference (CICC)*, 2019, pp. 1–4.
- [110] H. S. Bindra, A. J. Annema, S. M. Louwsma, and B. Nauta, "A 0.2 - 8 MS/s 10b flexible SAR ADC achieving 0.35 - 2.5 fJ/conv-step and using self-quenched dynamic bias comparator," in *2019 Symposium on VLSI Circuits*, June 2019, pp. C74–C75.
- [111] A. Georgiadis, "Gain, phase imbalance, and phase noise effects on error vector magnitude," *IEEE Transactions on Vehicular Technology*, vol. 53, no. 2, pp. 443–449, March 2004.

-
- [112] “Evolved Universal Terrestrial Radio Access (E-UTRA); User Equipment (UE) radio transmission and reception,” vol. 3GPP TS 36.101 version 15.8.0 Release 15, October 2018. [Online]. Available: https://www.etsi.org/deliver/etsi_ts/136100_136199/136101/15.08.00_60/ts_136101v150800p.pdf
- [113] B. Jann, G. Chance, A. G. Roy, A. Balakrishnan, N. Karandikar, T. Brown, X. Li, B. Davis, J. L. Ceballos, N. Tanzi, K. Hausmann, H. Yoon, Y. Huang, A. Freiman, B. Geren, P. Pawliuk, and W. Ballantyne, “21.5 A 5G Sub-6GHz Zero-IF and mm-Wave IF Transceiver with MIMO and Carrier Aggregation,” in *2019 IEEE International Solid-State Circuits Conference - (ISSCC)*, Feb 2019, pp. 352–354.
- [114] J. Lee, S. Han, J. Lee, B. Kang, J. Bae, J. Jang, S. Oh, J. Chang, S. Kang, K. Y. Son, H. Lim, D. Jeong, I. Jong, S. Baek, J. H. Lee, R. Ni, Y. Zuo, C. Yao, S. Heo, T. B. Cho, and I. Kang, “A Sub-6-GHz 5G New Radio RF Transceiver Supporting EN-DC With 3.15-Gb/s DL and 1.27-Gb/s UL in 14-nm FinFET CMOS,” *IEEE Journal of Solid-State Circuits*, vol. 54, no. 12, pp. 3541–3552, Dec 2019.
- [115] M. Acar, “Power Amplifiers in CMOS Technology: A contribution to power amplifier theory and techniques,” Ph.D. dissertation, University of Twente, 2 2011, 10.3990/1.9789036531382.
- [116] N. O. Sokal and A. D. Sokal, “Class E-A new class of high-efficiency tuned single-ended switching power amplifiers,” *IEEE Journal of Solid-State Circuits*, vol. 10, no. 3, pp. 168–176, 1975.
- [117] M. Kazimierczuk, *RF Power Amplifiers*. John Wiley & Sons, Ltd, 2014, ch. 1, pp. 1–64.
- [118] F. Raab, “Idealized operation of the class E tuned power amplifier,” *IEEE Transactions on Circuits and Systems*, vol. 24, no. 12, pp. 725–735, 1977.
- [119] J. Ponte, A. Ghahremani, M. Huiskamp, A. J. Annema, and B. Nauta, “Augmentation of Class-E PA Reliability under Load Mismatch Conditions,” in *2018 25th IEEE International Conference on Electronics, Circuits and Systems (ICECS)*, 2018, pp. 33–36.

- [120] C. D. Presti, F. Carrara, A. Scuderi, S. Lombardo, and G. Palmisano, “Degradation Mechanisms in CMOS Power Amplifiers Subject to Radio-Frequency Stress and Comparison to the DC Case,” in *2007 IEEE International Reliability Physics Symposium Proceedings. 45th Annual*, 2007, pp. 86–92.
- [121] C. Sánchez-Pérez, D. Sardin, M. Roberg, J. de Mingo, and Z. Popović, “Tunable outphasing for power amplifier efficiency improvement under load mismatch,” in *2012 IEEE/MTT-S International Microwave Symposium Digest*, 2012, pp. 1–3.
- [122] F. H. Raab, “Effects of circuit variations on the class E tuned power amplifier,” *IEEE Journal of Solid-State Circuits*, vol. 13, no. 2, pp. 239–247, 1978.
- [123] E. L. Firrao, A. J. Annema, and B. Nauta, “An Automatic Antenna Tuning System Using Only RF Signal Amplitudes,” *IEEE Transactions on Circuits and Systems II: Express Briefs*, vol. 55, no. 9, pp. 833–837, 2008.
- [124] K. Boyle and M. Leitner, “Mobile phone antenna impedance variations with real users and phantoms,” in *2011 International Workshop on Antenna Technology (iWAT)*, 2011, pp. 420–423.
- [125] C. Kim, *Electromigration in Thin Films and Electronic Devices: Materials and Reliability*, ser. Woodhead Publishing Series in Electronic and Optical Materials. Elsevier Science, 2011.
- [126] P. Sharma, S. Tyaginov, Y. Wimmer, F. Rudolf, K. Rupp, M. Bina, H. Enichlmair, J. Park, R. Minixhofer, H. Ceric, and T. Grassner, “Modeling of Hot-Carrier Degradation in nLDMOS Devices: Different Approaches to the Solution of the Boltzmann Transport Equation,” *IEEE Transactions on Electron Devices*, vol. 62, no. 6, pp. 1811–1818, 2015.
- [127] F. Monsieur, E. Vincent, D. Roy, S. Bruyere, J. C. Vildeuil, G. Pananakakis, and G. Ghibaudo, “A thorough investigation of progressive breakdown in ultra-thin oxides. Physical understanding and

- application for industrial reliability assessment,” in *2002 IEEE International Reliability Physics Symposium. Proceedings. 40th Annual (Cat. No.02CH37320)*, 2002, pp. 45–54.
- [128] W. Karoui and T. Parra, “A protection circuit for HBT RF Power Amplifier under load mismatch conditions,” in *2008 Joint 6th International IEEE Northeast Workshop on Circuits and Systems and TAISA Conference*, 2008, pp. 241–244.
- [129] A. Scuderi, F. Carrara, and G. Palmisano, “VSWR-protected silicon bipolar power amplifier with smooth power control slope,” in *2004 IEEE International Solid-State Circuits Conference (IEEE Cat. No.04CH37519)*, 2004, pp. 194–522 Vol.1.
- [130] C. Wei, L. Wei, and H. Shizhen, “A novel VSWR-protected and controllable CMOS class E power amplifier for Bluetooth applications,” in *2009 4th IEEE Conference on Industrial Electronics and Applications*, 2009, pp. 420–424.
- [131] G. T. Sasse and J. Bisschop, “The hot carrier degradation rate under AC stress,” in *2010 IEEE International Reliability Physics Symposium*, 2010, pp. 830–834.
- [132] J. S. Yuan and H. Tang, “CMOS RF Design for Reliability Using Adaptive Gate–Source Biasing,” *IEEE Transactions on Electron Devices*, vol. 55, no. 9, pp. 2348–2353, 2008.
- [133] M. Acar and A. J. Annema and B. Nauta, “Generalized Analytical Design Equations for Variable Slope Class-E Power Amplifiers,” in *2006 13th IEEE International Conference on Electronics, Circuits and Systems*, 2006, pp. 431–434.
- [134] —, “Variable-Voltage Class-E Power Amplifiers,” in *2007 IEEE/MTT-S International Microwave Symposium*, 2007, pp. 1095–1098.
- [135] —, “Analytical Design Equations for Class-E Power Amplifiers with Finite DC-Feed Inductance and Switch On-Resistance,” in *2007 IEEE International Symposium on Circuits and Systems*, 2007, pp. 2818–2821.

- [136] P. B. Kenington, *High linearity RF amplifier design*. Artech House, Inc., 2000.
- [137] S. C. Cripps, *Advanced techniques in RF power amplifier design*. Artech House, 2002.
- [138] E. Zenteno, M. Isaksson, and P. Händel, “Output Impedance Mismatch Effects on the Linearity Performance of Digitally Predistorted Power Amplifiers,” *IEEE Transactions on Microwave Theory and Techniques*, vol. 63, no. 2, pp. 754–765, Feb 2015.
- [139] C. Sánchez-Perez, J. de Mingo, P. G. Ducar, P. L. Carro, and A. Valdovinos, “Improving Digital Predistortion Mismatch Sensitivity Using Tunable Matching Networks,” *2011 IEEE 73rd Vehicular Technology Conference*, pp. 1–5, 2011.
- [140] A. Keerti and A. Pham, “Dynamic output phase to adaptively improve the linearity of power amplifier under antenna mismatch,” in *2005 IEEE Radio Frequency integrated Circuits (RFIC) Symposium - Digest of Papers*, June 2005, pp. 675–678.
- [141] A. van Bezooijen, C. Chanlo, and A. H. M. van Roermund, “Adaptively preserving power amplifier linearity under antenna mismatch,” in *2004 IEEE MTT-S International Microwave Symposium Digest*, vol. 3, June 2004, pp. 1515–1518.
- [142] F. Roger, “An analog approach to power amplifier predistortion,” *Microwave Journal*, vol. 54, no. 4, pp. 60–76, 2011.